

The Effect of Cholesterol on a Five Component
Mitochondria-Like Membrane

THE EFFECT OF CHOLESTEROL ON A FIVE COMPONENT
MITOCHONDRIA-LIKE MEMBRANE

BY
KELLY E. CATHCART, B.Sc.

A THESIS
SUBMITTED TO THE DEPARTMENT OF PHYSICS AND ASTRONOMY
AND THE SCHOOL OF GRADUATE STUDIES
OF MCMASTER UNIVERSITY
IN PARTIAL FULFILMENT OF THE REQUIREMENTS
FOR THE DEGREE OF
MASTER OF SCIENCE

Master of Science (2014)

McMaster University

Physics

Hamilton, Ontario, Canada

TITLE: The Effect of Cholesterol on a Five Component Mitochondria-Like Membrane

AUTHOR: Kelly E. Cathcart

B.Sc.H, (Physics)

Queen's University, Kingston, Canada

SUPERVISOR: Dr. Cécile Fradin

NUMBER OF PAGES: xxiii, 129

Abstract

Cholesterol is known to affect biophysical quantities in one and two component membranes, overall increasing membrane thickness and orientational order and decreasing membrane fluidity. Although these effects are useful in the plasma membrane of cells where strength is a desired property, there is evidence suggesting that the appearance of cholesterol in other cellular membranes has adverse effects. Indeed, cholesterol is found at elevated levels in the mitochondria membranes of cancer cells and is associated with chemotherapy resistance. At the molecular level, the link between cancer and cholesterol seems to be that cholesterol interferes with apoptosis, or programmed cell death, specifically by inhibiting the insertion of the pro-apoptotic protein Bax in the mitochondria outer membrane. We studied the effects of cholesterol on a five component mitochondria-like membrane, in order to determine which of these are relevant for Bax membrane insertion. As expected we found, using x-ray and neutron scattering, that upon cholesterol addition: (1) the thickness of the mitochondria-like membrane increases, (2) the area per phospholipid decreases, and (3) the orientational order of the membrane increases. Interestingly, our data indicate that the ordering effect of cholesterol is less efficient for the five component mitochondria-like membrane than for a single component membrane. Finally, we determined that in spite of the relatively high degree of unsaturation of the lipids in the mitochondria-like

membrane, cholesterol adopts a canonical orientation. At higher cholesterol concentrations, cholesterol's polar hydroxyl group moves outwards and comes in proximity with the phospholipid's carbonyl group, allowing hydrogen bonding between the two types of molecules. Any of the above effects could in principle be responsible for cholesterol's inhibition of Bax insertion, thus follow up studies are required to confirm which, or what combination of them are relevant for apoptosis.

Acknowledgements

I would like to take this opportunity to thank my incredibly hard working and dedicated supervisor, Dr. Cécile Fradin. Working with her has been such a pleasure and I'm constantly in awe at how much she accomplishes. I appreciate the knowledge I've gained, and the experiences I've had working with her as her student. A special thank you to Dr. Maikel Rheinstädter for his endless help and guidance during my project, and for the use of his x-ray diffractometer, BLADE. Finally I would like to thank my committee members, Dr. Maikel Rheinstädter and Dr. Bruce Gaulin, for their time, insightful comments and tough questions.

I must also thank the Fradin lab members, who have made this experience so much fun. I have enjoyed working with all of you, and have greatly appreciated your help and advice. Nehad, coming to ABB everyday wouldn't have been the same without you buddy.

Of course I would like to thank my family, Mom and Dad, Quinn and Currie, who have always supported and pushed me. You make me excited to pursue new projects and you have always been happy to listen to me blab on and on about what I've been doing. I would also like to thank my extended family, Rebecca, Anna, Ellin and the kids. I am so lucky to have you all in my life, thank you for your support. Finally I would like to thank my partner and best friend, I wouldn't have been able to do this

without your encouragement, love and unwavering support John.

Abbreviations

AECL	= Atomic Energy of Canada Limited
BLADE	= Biological Large Angle Diffraction Experiment
CL	= Cardiolipin
c-Bid	= Cleaved Bid
DAPC	= 1,2-diarachidonoyl- <i>sn</i> -glycero-3-phosphocholine
DFF	= DNA Fragmentation Factor
diC22:1PC	= Dierocoyl- <i>sn</i> -glycero-3-phosphocholine
DISC	= Death-Inducing Signaling Complex
DMPC	= Dimyristoylphosphatidylcholine
DMPS	= Dimyristoylphoshoserine
DNA	= Deoxyribonucleic Acid
DOPS	= 1,2-dioleoyl- <i>sn</i> -3-phospho-L-serine
DPPC	= 1,2-dipalmitoyl- <i>sn</i> -glycero-3-phosphocholine
D₆ cholesterol	= 2,2,3,4,4,6 D ₆ cholesterol, cholesterol deuterated at 6 sites near the hydroxyl group shown in figure 1.4
FADD	= Fas Associated Death Domain
FWHM	= Full Width at Half Maximum
HEPES	= 4-(2-hydroxyethyl)-1-piperazineethansulfonic acid

MIM	=	Mitochondria Inner Membrane
Mito-like	=	Mitochondria like membrane made of five lipids
MOM	=	Mitochondria Outer Membrane
MOMP	=	Mitochondria Outer Membrane Permeabilization
NRU	=	National Research Universal
NSLD	=	Neutron Scattering Length Density
PA	=	Phosphatidic acid
PC	=	Phosphatidylcholine
PE	=	Phosphatidylethanolamine
PI	=	Phosphatidylinositol
POPC	=	1-palmitoyl-2-oleoyl- <i>en</i> -glycero-3-phosphocholine
PS	=	Phosphatidylserine
SLD	=	Scattering Length Density
SOPC	=	1-stearoyl-2-oleoyl- <i>sn</i> -glycero-3-phosphocholine
t-Bid	=	Truncated Bid
TFE	=	Trifluoroethanol
TNF	=	Tumore Necrosis Factor
TOCL	=	1',3'-bis[1,2-dioleoyl- <i>sn</i> -glycero-3-phospho]- <i>sn</i> -glycerol
WAXS	=	Wide Angle X-ray Scattering
10H	=	Mito-like sample containing 10% protonated cholesterol
10D	=	Mito-like sample containing 10% deuterated cholesterol
20H	=	Mito-like sample containing 20% protonated cholesterol
20D	=	Mito-like sample containing 20% deuterated cholesterol

Contents

Abstract	iii
Acknowledgements	v
Abbreviations	vii
1 Introduction	1
1.1 Biological Context and Hypothesis	1
1.1.1 Apoptosis and the Importance of Cell Death	2
1.1.2 Apoptotic Pathways	4
1.1.3 Phospholipids and Biomembranes	8
1.1.4 The Outer Mitochondria Membrane and Apoptosis	11
1.1.5 Cholesterol: Structure and Function	13
1.1.6 Cholesterol's Effect on Apoptosis	16
1.2 Scattering Experiments for Biological Membrane Structure Determination	17
1.2.1 Comparing X-ray and Neutron Scattering of Biological Membranes	18

1.2.2	Scattering Experiments Used to Investigate Membranes and Membranes Containing Cholesterol	20
2	Experimental Methods	23
2.1	Sample Preparation	23
2.1.1	Reagents	23
2.1.2	Membrane Preparation Composition	25
2.1.3	Substrates	26
2.1.4	Multilamellar Membranes Preparation	27
2.1.5	Liposomes	29
2.2	X-ray Apparatus and Experiment	30
2.2.1	Apparatus: BLADE	30
2.2.2	Scattering Theory	31
2.2.3	Out of Plane, Reflectivity Experiments	33
2.2.4	Reflectivity Analysis: Electron Density Scaling and Fitting, and Form Factor Phase and Membrane Thickness Determination .	35
2.2.5	In Plane Scattering Experiments	38
2.2.6	In Plane Analysis: Area per Phospholipid Chain and Acyl Chain Orientational Order Parameter	39
2.3	Neutron Apparatus and Experiment	40
2.3.1	Apparatus: N5 Triple Axis Spectrophotometer	40
2.3.2	Scattering Theory	42
2.3.3	Rocking Scan	44
2.3.4	Reflectivity Experiment	45
2.3.5	Form Factor Phase Determination	48

2.3.6	Reflectivity Data: Scaling Neutron Scattering Length Density Profiles	50
2.4	Fluorescence Apparatus and Experiment	52
2.4.1	Apparatus: TECAN Spectrophotometer	52
2.4.2	Dual Ratiometric Method Theory	52
2.4.3	Dual Ratiometric Method Experiment	54
2.4.4	Calibration	55
3	Results	57
3.1	Dual Ratiometric Fluorescence Results for Cholesterol Orientation in Mito-like Membranes	57
3.2	X-Ray Diffraction Results	59
3.2.1	Structure of Multi-Component Mitochondria-Like Membranes	62
3.2.2	Cholesterol Effects on Mitochondria-Like Membranes	67
3.3	Neutron Reflectivity Results	71
3.3.1	Determination of Sample Orientation Quality	71
3.3.2	Neutron Reflectivity and Scattering Length Density Profiles	73
3.3.3	Structure of Single Component POPC and Multi-Component Mitochondria-like Membranes	75
3.3.4	Cholesterol Effects on Mitochondria-Like Membranes: Membrane Thickness	79
3.3.5	Cholesterol Effects on Mitochondria-Like Membranes: Location and Orientation of Cholesterol	82
4	Discussion	87

4.0.6	How Different is the Multicomponent Mitochondria-Like Membrane From a Single Component POPC Membrane?	87
4.0.7	Effect of Cholesterol on The Complex Mitochondria-Like Membrane	91
4.1	Orientation of Cholesterol in a Mitochondria-like Membrane	95
4.2	Implications for Mitochondria with Elevated Cholesterol Content	99
5	Concluding Statements and Future Work	101
A	Neutron Form Factor Determination	104
B	Neutron Scattering Length Density Profiles	108

List of Figures

- 1.1 **Extrinsic and intrinsic apoptosis pathways.** Apoptosis in cells can occur via the extrinsic or intrinsic pathway. The extrinsic pathway begins with a signal originating from outside the cell that activates receptors on the cell surface called Fas. These receptors bind together to form the Fas associated death domain, FADD, which recruits pro-caspase 8 to form the death inducing signal complex, DISC. DISC in turn activates caspase 8 which through a caspase cascade activates caspase 3. Caspase 3 activates the DNA fragmentation factor, DFF, which destroys the DNA of the cell. The intrinsic pathway involves a signal originating from within the cell, often stress induced, that activates certain Bcl-2 family of proteins and results in mitochondria outer membrane permeabilization, MOMP. See text for details. The inter-membrane space of the mitochondria includes cytochrome c, which gets released during MOMP and activates caspase 3. This process has the same outcome as the extrinsic pathway. This figure has been adapted from [78].

1.2 Structure of a phospholipid and of a simplified phospholipid membrane. Phospholipids are composed of a hydrophilic head group that contains a glycerol-3-phosphate group, and a hydrophobic tail group composed of acyl chains attached to the headgroup via carbonyl groups at the sn1 and sn2 positions. The phospholipid shown here is 1-palmitoyl-2-oleoyl- <i>sn</i> -glycero-3-phosphocholine, the main component of the membrane studied in this work. Biological membranes contain sterols as well as proteins in addition to the phospholipids shown here. They are also fluid both laterally and vertically as opposed to this static representation.	10
1.3 Lipid composition of mitochondria-like membranes. The five phospholipid shown here were used in this work to model the mitochondria outer membrane.	13
1.4 Chemical structure of Cholesterol and D6-Cholesterol. Cholesterol and a deuterium labeled cholesterol often used in neutron diffraction experiments are shown here. Both are composed of a polar hydroxyl group attached to a four ring planar structure with a flexible hydrocarbon chain.	14
2.1 Relative humidity as a function of temperature for KCl and K_2SO_4. RH values for x-ray and neutron experiments were found from regressions on RH versus temperature plots for a) KCl: $RH = 0.0009T^2 - 0.1923T + 88.599$ and, b) K_2SO_4 : $RH = -0.0599T + 98.772$. Data comes from Ref. [90].	24

2.6	Form factor determination .A) Semi-log plots of the absolute slope, $\rho(n)$ predicted from equation 2.24, and experimental form factor data for the mito-like sample. The signs of the form factors are shown above or below the data, and alternate in sign until a dip in the theoretical curve after which the alternation starts again. The first sign must be negative as that produces the "U" shape in the NSLDs characteristic of a bilayer. $\rho(n) = [- + - - +]$. B) Data points represent form factors calculated from reflectivity data following equation 2.19, while lines are a fit, whose slopes are the data points from A). The slope of each line then determines the sign of each form factor, and thus the form factor phases, ν_n . Form factors of the mito-like sample for each of five diffraction orders are displayed.	50
2.7	Calibration of fluorescent R to dipole potential, ψ_d . Data points represent values of R measured in our experiment for different samples as a function of the known values of ψ_d from the literature [44]. The line is a linear fit to the data, $R = (0.012 \pm 0.024)\psi_d - (1.3 \pm 1.1)$. Error bars represent standard deviations from three independent R measurements	56
3.1	Dipole potential as a function of cholesterol content . Data points represent ψ_d values calculated using equation 2.32 for three independent trials (mean \pm standard deviation). Curves are guides to follow the trend and not fits.	58

3.4 Calculated electron densities for the mitochondria-like and POPC membranes. The electron densities for the mitochondria-like and POPC membranes were determined from the data shown in Figure 3.3 and modelled with Gaussian peak profiles to represent different lipid molecular components. The head group region is fit with a single Gaussian peak, and the chain terminal region by a single Gaussian depression positioned at the centre of the membrane, both sitting atop a constant background. The individual components of the fit are plotted with a zero background in black and grey for the mitochondria-like and POPC membranes respectively. The dashed black and grey lines are the result of the total fit for the mitochondria-like and POPC membranes respectively. The FWHMs of the head group region, w_h , and chain terminal region, w_c , are indicated on the figure and their values are listed in table 3.2.	65
3.5 Area condensation effect of cholesterol in mitochondria-like membranes. Semi-log plot of chain correlation peaks for mitochondria-like membranes containing between 0 and 30 mol % cholesterol (see Table 2.1 for exact lipid composition). Each curve was fit with a Gaussian profile on a slopping background (black lines). Curves were shifted vertically for clarity. The inset shows the average area per total chain (i.e. including cholesterol chains), A_c , directly inferred from the position of the peak (closed symbols), compared to the average area per phospholipid chain, A_{pc} , as corrected for cholesterol volume using Eq .3.1 (open symbols). Solid lines are guides for the eyes.	68

3.6 Cholesterol increases mitochondria-like membrane orientational order. Integrated intensities along the chain correlation peak are plotted as a function of the polar angle ϕ . Curves have been shifted upwards for clarity. Continuous lines represent fit of the filled symbol data with Eq. (2.14), while the open symbols were not included in the fit. The inset shows the X-ray chain orientational order parameter, $S_{\text{X-ray}}$, calculated from that fit.	69
3.7 Cholesterol increases lamellar spacing and membrane thickness in mitochondria-like membranes A) Reflectivity curves for mitochondria-like membranes with 0, 10, 20 and 30 mol% cholesterol. The curves are shifted for clarity. Intensity is plotted on a logarithmic scale. B) Scaled electron density profiles of mitochondria-like membranes with the same cholesterol content as in A). C) Lamellar spacing, d_z , and peak-to-peak membrane thickness, d_{hh} , as a function of cholesterol content.	70

3.8 Neutron rocking curves. Semi-log plots of neutron rocking curves for the first diffraction peak for each sample taken at 100% D ₂ O. Minima in the curves occur where there is neutron absorption while rotating the sample in θ . Maximum absorption occurs when the substrate is parallel to either the incident or diffracted beams. The orientation of the bilayers in the sample can be determined from the width of the peak. The narrower the peak, the more oriented the bilayers. See section 2.3.3 for details. The six samples are POPC, mito-like (MITO), mito-like with 10% protonated cholesterol (10H), mito-like with 10% deuterated cholesterol (10D), mito-like with 20% protonated cholesterol (20H) and mito-like with 20% deuterated cholesterol membranes. Cholesterol samples are in mito-like membranes.	72
3.9 Neutron relectivity profiles. Semi-log plots of neutron reflectivity curves for each sample in 8% D ₂ O, 40% D ₂ O, 70% D ₂ O and 100% D ₂ O in H ₂ O. Profiles are shifted vertically for clarity, in ascending order with the 8% D ₂ O profile at the bottom and the 100% D ₂ O profile at the top. Five diffraction orders were used for all profiles in all samples. .	73
3.10 NSLD profiles for a mito-like membrane at all contrasts. Profiles were obtained for each of the four D ₂ O contrast solutions using equation 2.20 and scaled using equation 2.28.	75
3.11 NSLD profiles for mito-like (MITO) and POPC membranes. Profiles are of membranes hydrated with 8% D ₂ O. Notable differences include thickness, carbonyl peak width and acyl chain shape.	76

3.12 Membrane bilayer thicknesses. Lamellar thickness, d_z , membrane thickness found by neutron scattering, d_b , membrane thickness found by x-ray scattering, d_{hh} , the glycerol region thickness, d_g and half the water layer thickness, d_w , are represented shematically.	78
3.13 NSLD profiles for mito-like (MITO), 10 and 20% cholesterol containing membranes. Inset shows the change in membrane thickness defined as the distance between the two carbonyl peaks, as a function of cholesterol content. Note that cholesterol has a thickening effect on the multicomponent mito-like membranes.	80
3.14 Water probability profiles for mito-like 10 and 20% cholesterol containing membranes. Curves are obtained from the average of the differences between NSLDs of the samples at the four contrast solutions. The inset shows the change in water penetration, defined from the center of the membrane, as a function of cholesterol content.	81
3.15 NSLD profiles for mito-like (MITO), 10 and 20% cholesterol containing membranes. Profiles are obtained using equation 2.20 and scaled using equation 2.28. Membranes containing protonated cholesterol are shown as black curves, while those labeled with deuterated cholesterol are shown as dashed gray curves. Note that as cholesterol content increases, a “kink” in the acyl chain region begins to appear, more pronounced in the deuterated membrane, signaling greater lipid order.	83

Chapter 1

Introduction

1.1 Biological Context and Hypothesis

Cholesterol's effect on simple membranes, those composed of one or two lipid species, has been a subject of study for many years. Owing to its large ring structure and small polar hydroxyl group, cholesterol tends to order phospholipids by straightening hydrocarbon chains and thus condensing the area per phospholipid [89]. The goal of this work was to describe the structural features of a multicomponent mitochondria-like membrane, to see how they changed as a function of cholesterol, and to determine if these changes were consistent with those seen in one component membranes. The following sections introduce the biological context of this work, and to explain its significance for the biochemical and the biophysical communities.

1.1.1 Apoptosis and the Importance of Cell Death

Cell death, contrary to what one might believe, is an important process for multi-cellular organisms. Perhaps even more important is its regulation. Controlled cell death, known as apoptosis, is organisms' way of controlling tissue growth and disposing of dysfunctional cells. Apoptosis is an evolutionary conserved process and is characterized by the loss of organelle (mitochondria and endoplasmic reticulum) integrity, DNA fragmentation and plasma membrane blebbing [42]. This is in contrast to another form of cell death, necrosis. While necrosis involves the swelling of many cells together, resulting in a cluster of dead cells, which can significantly damage the tissue, apoptosis normally occurs in cells interspersed with non-apoptotic cells within a tissue, keeping the tissue healthy [74].

Proper apoptotic regulation is important to the health of organisms. If an unhealthy cell were allowed to continue to undergo mitosis and reproduce, the tissue would begin to be composed of dysfunctional cells resulting in genetic instability and a disease state for the organism. Indeed, the lack of apoptosis is one of the hallmarks of cancer [127]. Cancer, however, is not the only disease that results in part from the absence of apoptotic control; neurodegenerative disorders such as Parkinson's and Huntington's diseases as well as symptoms from stroke are all associated with a lack of apoptotic regulation. While cancer is characterized by a cell's ability to avoid death, neurodegenerative disorders such as Alzheimer's, Parkinson's and Huntington's see an overabundance of neuronal apoptosis [81].

Cancer is a disease characterized by the uncontrolled growth of unhealthy cancer cells, which invade surrounding healthy tissue. As such many cancer treatments, such as chemotherapy and immunotherapy target the apoptotic pathway with the intent of

killing cancer cells. However, some cancer cells are capable of evading apoptosis thus developing treatment resistance. This has motivated the development of molecular targeted treatments which allow the cancer cells to undergo apoptosis [57, 42, 9]. An example of such a type of treatment is Bcl-2 inhibitors. The Bcl-2 family of proteins contains pro and anti-apoptotic proteins (see section 1.1.2), and over expression of anti-apoptotic Bcl-2 proteins has been linked with chemotherapy resistance. Thus the Bcl-2 inhibitors are agents which target the expression of the anti-apoptotic proteins in order to facilitate apoptosis [57].

Dominant inherited Huntington's disease, is caused by the mutant huntingtin protein, called mutant Htt or mHtt. The function of both the wild type and mutant huntingtin protein remains unclear, however it is believed that the disease is brought on by both the absence of wild type huntingtin as well as the toxic functions of the mHtt [18]. Studies have shown that wild type huntingtin is anti-apoptotic, in that it protects against pro-apoptotic signals [103, 102]. Additionally, the removal of wild type huntingtin leads to the rapid development of apoptotic cells in numerous locations in the brain [29]. Thus, Huntington's disease, and its potential treatments are intimately linked with the regulation of apoptosis.

Parkinson's disease (PD), is a neurodegenerative disorder with no known cause. Symptoms, however are a direct result of the death of dopamine secreting neurons located in the midbrain. There has been debate over the years if apoptosis, necrosis or other forms of cell death were the main pathways through which the dopaminergic neurons died. The correct answer to this question is important from the perspective of symptom treatments. Recently, studies looking for the elevated presence of certain characteristic proteins involved in apoptosis have found that indeed these proteins

(caspase 8 [48, 122], caspase 9 [122], caspase 3 [47, 115] and Bax [49]) have all been found to have elevated levels in the midbrain neurons of PD patients. Experimental evidence suggests that neurodegeneration in PD patients occurs in part by mitochondria dependent apoptosis [96, 97, 121]. From the mounting evidence, apoptosis appears to be a crucial pathways through which dopaminergic neurons die unnecessarily in PD patients. Designing treatment that aims to inhibit neuronal apoptosis would therefore be beneficial for symptom management and the inhibition of disease progression.

The dysregulation of apoptosis is thus a defining feature in cancer, Huntington's and Parkinson's diseases, among many others. These diseases affect many people throughout the world, regardless of socio-economic class. The development of effective treatments as well as potential cures are central to many research initiatives. Understanding the regulation of apoptosis, how to evade cancer cell immortality, and how to reduce overabundant apoptosis in neurodegenerative disorders, is of great interest and value to the larger scientific community.

1.1.2 Apoptotic Pathways

Apoptosis proceeds via two pathways, the extrinsic and intrinsic pathways outlined in figure 1.1. As the names imply the extrinsic pathway is activated outside of the cell, while the intrinsic begins within the cell. The extrinsic pathway begins when a cell death signal is sent to the cell and received on the cell surface by a pro-apoptotic receptor, Fas, belonging to the tumor necrosis factor (TNF) superfamily. Clustering together following their activation, these pro-apoptotic ligands form a death-inducing

signaling complex (DISC) which activates caspase 8, a cysteine protease, which subsequently can either initiate proteins involved in the intrinsic pathway or activate caspase 3. Caspase 3 then activates DNA fragmentation factor (DFF) which destroys the cell's DNA [78]. The intrinsic pathway, also called the mitochondrial pathway, begins with a signal from within the cell, such as DNA damage, that activates caspase 8. Caspase 8 in turns activates the Bcl-2 family pro-apoptotic protein Bid. Bid is cleaved to form cleaved Bid (c-Bid), composed of truncated Bid (t-Bid) and the protein fragment p7. t-Bid, a positively charged protein approaches the negative outer mitochondria membrane where it undergoes a conformational change to insert in the membrane [68]. Once inserted, t-Bid activates pro-apoptotic Bcl-2 family proteins, such as Bak and Bax. Bak is constitutively mitochondrial, while Bax, like t-Bid, approaches the membrane and inserts, taking on a transmembrane conformation. Following activation, Bax and Bak oligomerize to form a complex. This complex forms an aqueous pore in the membrane, which releases the contents of the inter-membrane space into the cytosol of the cell, namely cytochrome c. Cytochrome c activates caspases 9 and 3 which subsequently lead to morphological changes in the cell characteristic of apoptotic cell death [78].

The Bcl-2 family of proteins, two of which are mentioned above, is composed of pro and anti-apoptotic proteins that work together with membrane lipids to regulate mitochondria outer membrane permeabilization (MOMP) in the intrinsic apoptosis pathway. MOMP is often said to be the point of no return during apoptosis. This is the step where the cell commits to dying. The mitochondria membrane itself, in addition to the proteins mentioned above, is thus a key player in apoptosis, and lipid-lipid, lipid-protein interactions are important for apoptosis regulation. Much work has

been done to investigate protein-protein interactions involved in apoptosis [67, 106], as well as lipid-protein interaction [32, 13, 33, 129, 105]. This work aims to study the structure of the membrane to further understand how lipid membranes may impact protein function during apoptosis.

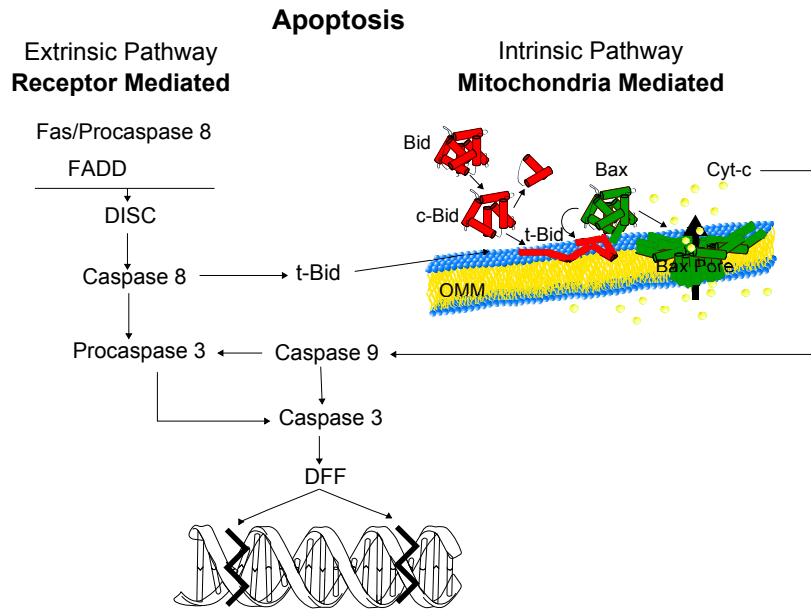


Figure 1.1: **Extinsic and intrinsic apoptosis pathways.** Apoptosis in cells can occur via the extrinsic or intrinsic pathway. The extrinsic pathway begins with a signal originating from outside the cell that activates receptors on the cell surface called Fas. These receptors bind together to form the Fas associated death domain, FADD, which recruits procaspase 8 to form the death inducing signal complex, DISC. DISC in turn activates caspase 8 which through a caspase cascade activates caspase 3. Caspase 3 activates the DNA fragmentation factor, DFF, which destroys the DNA of the cell. The intrinsic pathway involves a signal originating from within the cell, often stress induced, that activates certain Bcl-2 family of proteins and results in mitochondria outer membrane permeabilization, MOMP. See text for details. The intermembrane space of the mitochondria includes cytochrome c, which gets released during MOMP and activates caspase 3. This process has the same outcome as the extrinsic pathway. This figure has been adapted from [78].

1.1.3 Phospholipids and Biomembranes

Cells are surrounded by a selectively permeable plasma membrane called the plasma membrane that allows the transport of necessary molecules in and out of the cell, and prevents the transport of dangerous or unnecessary molecules. Each of the cellular organelles is also separated from the intracellular environment by a membrane. Membranes maintain important physiologic conditions required for the health of the cell and thus that of the tissue and organism. These include, but are not limited to osmotic pressure, pH, signal transduction, transport, and shape [14]. Where organelles are concerned, membranes have similar functions, primarily the transport of molecules in and out of cellular compartments. These membranes are composed of three types of amphipathic lipids (phospholipids, glycolipids and sterols) that self assemble to form a bilayer, with the hydrophilic polar head groups of the lipids on the outside and the hydrophobic hydrocarbon chains on the inside, as shown in figure 1.3. Membranes are also associated with numerous embedded membrane proteins and carbohydrates. Thus the plasma as well as organelle membranes are complex structures with many components that all function together for the health of the cell [14]. The types of lipids and protein that compose a membrane vary from organelle to organelle based on the required functions of that organelle. At physiologic conditions, cellular membranes are in a liquid crystalline state, allowing for diffusion of components throughout their respective leaflet [89]. The membrane is a dynamic environment, where components are constantly moving around, and should not be thought of as a static structure. It is the fluid nature of the membrane that contributes to its many functions [110].

The general structure of a phospholipid is a glycerol backbone with acyl chains

attached at the sn-1 and sn-2 hydroxyl groups, and a phosphate group attached at the glycerol sn-3 group followed by additional polar headgroups, as shown in figure 1.2. There is enormous variety of phospholipids. Which arise from the many distinctive headgroups, as well as variations in chain length and unsaturation, all of which are responsible for the physical properties of phospholipids [80]. The charges on headgroups are in great part responsible for electrostatic interactions with proteins [55], and their size can infer an intrinsic curvature to the bilayer. Curvature is important when considering self assembled structures, for example, lipids lacking intrinsic curvature such as a phosphatidylcholine are capable of forming planar bilayers, whereas lipids with intrinsic positive or negative curvature prefer curved self assembled structures that can be more relevant for a membrane for example of a structure within a cell that has a small radius of curvature such as the inner mitochondria membrane [72]. Curvature has been associated with membrane fusion, pore formation and protein insertion [19] and is thus an important physical feature of a membrane. The chain length, usually between 14-20 carbons long, and degree of unsaturation both affect the fluidity of the membrane, and the lipid's interaction with other lipids [80]. A carbon carbon double bond causes a kink in the hydrocarbon chain, which increases the area the chain explores within a membrane. This makes it more difficult to pack an unsaturated lipid in with other lipids, thus increasing the fluidity of the membrane.

Understanding biophysical properties of membranes is important to understand the impact of lipids on cellular functions as suggested above. As physiologically relevant membranes are so complex, containing different lipids as well as sterols and proteins, model membranes are useful because they provide a simple system with which to study complex interactions and allow studying the influence of specific lipids by

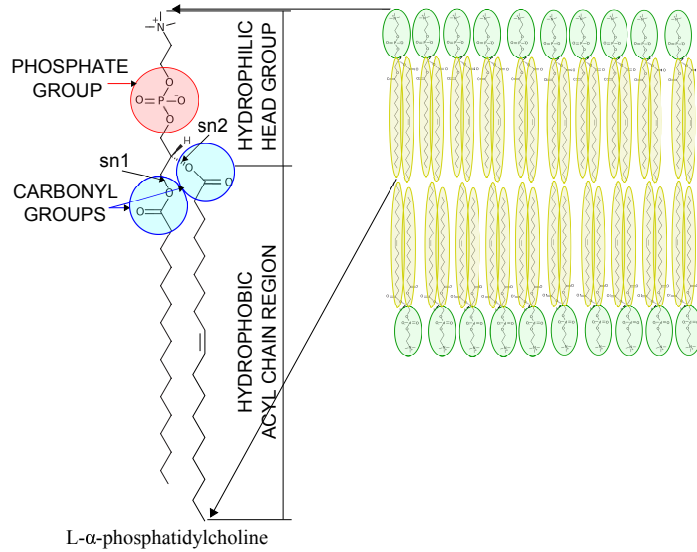


Figure 1.2: Structure of a phospholipid and of a simplified phospholipid membrane. Phospholipids are composed of a hydrophilic head group that contains a glycerol-3-phosphate group, and a hydrophobic tail group composed of acyl chains attached to the headgroup via carbonyl groups at the sn1 and sn2 positions. The phospholipid shown here is 1-palmitoyl-2-oleoyl-*sn*-glycero-3-phosphocholine, the main component of the membrane studied in this work. Biological membranes contain sterols as well as proteins in addition to the phospholipids shown here. They are also fluid both laterally and vertically as opposed to this static representation.

systematically varying their abundances. Much research in the field of biophysics is performed on membranes composed of one, two or at most three lipids. These studies range in topic, from investigating the structure of pores formed by proteins [100], to the localization of various molecules within a membrane [45, 27, 76]. The lipids chosen in these models aim to represent the type of membrane involved in the process being studied. For example, in Dies et al. 2014 Alzheimer's associated amyloid- β peptides are localized in a membrane composed of two lipids, dimyristoylphosphatidylcholine (DMPC) and dimyristoylphosphoserine (DMPS) to represent neuronal cell membranes, [27]. Of course, a two lipid composition ignoring sterols and other membrane integral proteins is a simplified picture. However, such a composition avoids

the risk of contributing effects from other components and allows for a clear picture of the peptides' position and orientation within the membrane. The mitochondria outer membrane, the subject of this work, has been modeled using both three [32] and five [67, 129, 105, 107] component model membranes. The five component membrane is used in this work and will be discussed in the following section.

1.1.4 The Outer Mitochondria Membrane and Apoptosis

Often referred to as the power-house of the cell, the mitochondria is an energy producing organelle inside the cell. Its external boundary is delimited by two membranes, the inner and outer membranes. In addition to their crucial role in energy production and storage, these membranes also play a major role in the apoptosis pathway. It is the mitochondria outer membrane (MOM) that is involved primarily in the intrinsic apoptosis pathway, and will be discussed here.

The mitochondria membranes of mammalian cells are composed mainly of phospholipids. Phosphatidylcholine (PC) and phosphatidylethanolamine (PE) account for \approx 40 and 30% respectively, phosphatidylserine (PS) and cardiolipid (CL) account for \approx 10-15%, while phosphatidic acid (PA) account for \approx 5% of mitochondria membrane phospholipids [131, 23]. The majority of CL, the lipid that seems to be required for Bcl-2 family proteins activation, has been found in the mitochondria inner membrane (MIM) and there has been considerable debate over whether CL is present at all in the MOM. However, recent work has concluded that as much as \approx 25% of mitochondria CL is found in the MOM [41]. Sterols, a group of molecules that include cholesterol and have been associated with membrane structure are found in trace amounts in the mitochondria membranes, despite their large

presence in mammalian cell plasma membranes [119].

Modeling of the MOM has been accomplished by a mixture of five lipid; PC, PE, PI, PS, and CL. PC, a zwitterionic lipid composed the majority of the mix, PE is a zwitterionic lipid with a negative intrinsic curvature, and PI, PS and CL all have a negative charge. This mixture is representative of the MOM and has previously been used in in vitro experiments investigating membrane protein interaction during apoptosis and has been shown to support pore formation via t-Bid and Bax [67]. The chemical structures of these five lipids are shown in figure 1.3. It is this mixture that will be used in this work to compare the structures of complex and simple membranes as well as the effect of cholesterol on such a complex membrane.

As mentioned in section 1.1.2, mitochondria outer membrane permeabilization, MOMP, governed by the Bcl-2 family of proteins, is the point of no return during programmed cell death. Considerable evidence shows that MOM lipid composition, and therefore MOM structure, play a role in its interaction with Bcl-2 family proteins during apoptosis. In vitro models of the outer membrane, with the lipid composition described above, have shown that by removing lipids largely responsible for the negative charge of the membrane, phosphatidylserine (PS) and cardiolipin (TOCL), t-Bid recruitment and binding is inhibited [107, 72]. Additionally, an increase in a lipid responsible for negative curvature, phosphatidylethanolamine (PE), was shown to promote Bax mediated permeabilization while a lack of PE was shown to hinder Bax oligomerization [72]. Since, from the above evidence, it is understood that specific lipids affect the MOM's influence on proteins presumably via non-specific interactions, the question of how the overall structure of the MOM affects protein function becomes important. This work will investigate the structure of the model

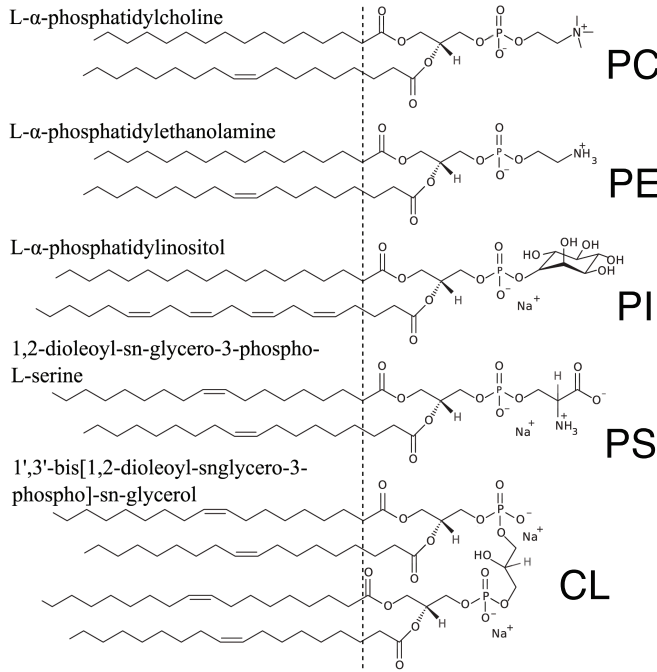


Figure 1.3: **Lipid composition of mitochondria-like membranes.** The five phospholipid shown here were used in this work to model the mitochondria outer membrane.

mitochondria-like membrane and how it changes with cholesterol, with the goal of explaining how these structural changes might affect Bax insertion.

1.1.5 Cholesterol: Structure and Function

Cholesterol is an amphipathic sterol composed of a rigid four ring planar structure with a flexible hydrocarbon tail at one end and a polar hydroxyl group at the other, see figure 1.4. In cells cholesterol is primarily found in membranes, with \approx 40-90% of cellular cholesterol in the plasma membrane of mammalian cells. Cholesterol content is \approx 30-50% of the lipid composition of the plasma membrane. The remainder of cellular cholesterol is found distributed in the membranes of the Golgi apparatus and in trace amounts in the mitochondria and endoplasmic reticulum membranes [89].

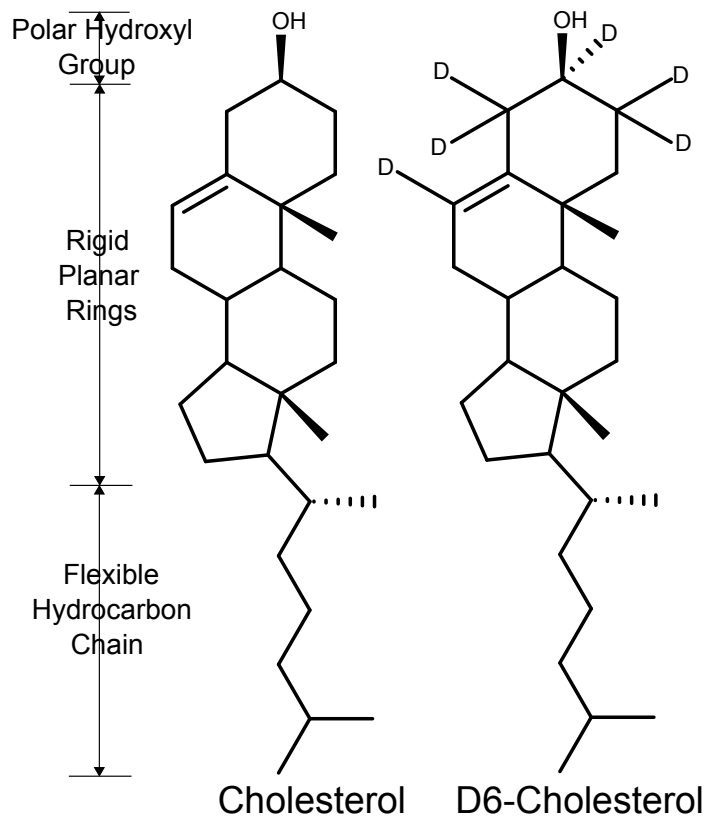


Figure 1.4: **Chemical structure of Cholesterol and D6-Cholesterol.** Cholesterol and a deuterium labeled cholesterol often used in neutron diffraction experiments are shown here. Both are composed of a polar hydroxyl group attached to a four ring planar structure with a flexible hydrocarbon chain.

This distribution, characteristic of healthy cells can change in disease states, for example the mitochondria cholesterol content increases in certain cancer cells [35].

The primary role of cholesterol in membranes seems to be its ability to control and modulate the biophysical properties of the membrane. In model membranes at temperatures above the gel to liquid crystalline transition, T_m , cholesterol decreases phospholipid chain fluidity [89]. Moreover, in model membranes in the liquid-crystalline state, cholesterol increases lateral orientational order [114], condensation and packing density of phospholipids [73, 111, 80] while decreasing phospholipid chain

motion [114].

Due to cholesterol's ability to condense membranes by straightening the acyl chains of phospholipids, cholesterol also causes an increase in the thickness of membranes. The effect has been reported in one component membranes [93, 51, 112], and has been shown to be most pronounced for saturated lipids such as DMPC, followed by lipids containing one monounsaturated chain such as SOPC, and finally lipids containing two monounsaturated chains, such as DOPC and diC22:1PC [93].

There is also evidence to support cholesterol's role in phospholipid synthesis. Specifically an increase in cholesterol concentration upregulates the enzyme responsible for phosphatidylcholine (PC) synthesis, cytidine 5'-triphosphate:phosphocholine cytidylyltransferase enzyme [109].

Finally, cholesterol has been associated with the lateral organization of membrane phospholipids. Beyond the fluid mosaic model of the membrane by Singer and Nicolson [110], it is now well understood that the lateral distribution of lipids and other membrane components is heterogeneous and although lateral diffusion of lipids and proteins is possible, it is not as free as previously thought. The heterogeneous organization of lipids is believed by some to be orchestrated by cholesterol. Moreover, direct binding of cholesterol and certain proteins is thought to occur in cholesterol lipid rafts [17].

Due to cholesterol's ability to affect the biophysical properties of membranes, cholesterol is capable of regulating certain proteins either via physical changes in the membrane or by direct binding. Some of these physical changes, for example the thickening and condensing effect, as well as membrane ordering are expected to affect MOM interaction with Bax. The following section will review the evidence that

inclusion of cholesterol in a mitochondria-like membrane indeed affects apoptosis.

1.1.6 Cholesterol's Effect on Apoptosis

In contrast to cholesterol's positive roles, its appearance in the MOM seems to bring about damaging consequences for the cell. The mitochondria of certain cancer cells contain elevated levels of cholesterol [35, 11], and cholesterol's presence in mitochondria membranes is associated with chemotherapy resistance [85]. As a response to these negative effects, statins, anti-cholesterol pharmaceuticals, have begun to be studied as possible anti-cancer agents. These studies have been positive in that they show that statins can induce apoptosis in certain cancer cells. [128]. In an attempt to understand the molecular mechanisms of cholesterol's negative impact in the MOM, studies have found that an increase in mitochondrial cholesterol is linked to an inhibition of Bax mediated MOMP. Specifically, Bax insertion is hindered by cholesterol's presence in a model MOM [20, 70, 107]. Although cholesterol can interact directly through binding with proteins, the fact that the enantiomer of cholesterol also has an inhibitory effect [20] on the insertion of Bax into the MOM, provides support for an inhibition mechanism based on structural changes in the membrane as opposed to one based on direct interaction between proteins and cholesterol.

Structural changes induced by cholesterol thus seem to be sufficient to inhibit pore formation by Bax. As cholesterol is known to increase membrane thickness and lateral orientational order and reduce membrane fluidity in model membranes, we hypothesized that one or a combination of these effects inhibits Bax insertion in the MOM. In order for Bax to insert into the MOM, and adopt a transmembrane conformation Bax must first insert through the headgroups of the membrane. The

condensing effect of cholesterol could cause problems for this step by eliminating membrane defects through which Bax could gain access to the hydrophobic core of the membrane. The next step is for Bax to go through this hydrophobic core, where an increase in cholesterol induced order could decrease membrane elasticity and fluidity required by Bax [3, 55]. The final step is for Bax to expose a hydrophilic section between two of the inserted helices to the intermembrane space [130]. Thickening of the membrane due to cholesterol would make this more difficult if not impossible due to the inherent length of the Bax helices.

As a first step towards our understanding of the effect of cholesterol on Bax membrane insertion, we quantitatively studied the effects of cholesterol in the five component mitochondria-like membrane. Scattering was chosen as the experimental means for this work as both scattering of x-rays and neutrons can give structural information on the appropriate length scale for lipid membranes as discussed in the next section.

1.2 Scattering Experiments for Biological Membrane Structure Determination

Scattering experiments are used to visualize the structure of both hard and soft condensed matter. It is well understood in the molecular biology community that structure and function are intimately related. In order to understand, for example a protein's function, it is first useful to understand its folded tertiary structure and in order to understand the cellular properties of a membrane it is first useful to determine its structure. X-ray and neutron scattering with wavelengths, λ , on the scale of

Angstroms, are capable of probing structures down to the appropriate molecular scale. Thus, quantities such as membrane thickness and the area per phospholipid are accessible through scattering experiments.

1.2.1 Comparing X-ray and Neutron Scattering of Biological Membranes

There are benefits to using different types of scattering depending on the type of experiment. Differences between x-ray and neutron scattering and between the information they provide, arise from the fundamental process of the scattering. X-rays are electromagnetic radiation and as such interact with electrons, while neutrons being neutral particles with a magnetic moment interact with the nuclei of atoms as well as with nuclear magnetic moments. Following analysis, x-rays provide an electron density profile of a sample, while neutrons produce a neutron scattering density profile. The x-ray scattering length of electrons in atoms depends both on the scattering length of a free electron and the electron density distribution in an atom, which increases linearly with atomic number. The scattering length therefore only depends on the element. By contrast, the neutron scattering length of a nuclei varies for the same element. It is dependent on the spin of the nucleus which can be zero or some non-zero half integer, i . The spin of a neutron is $1/2$, so the overall spin of the neutron nuclei interaction is $i+(1/2)$ or $i-(1/2)$. The scattering length can therefore vary greatly for elements close in atomic number and for isotopes [104] as can be seen in table 1.1. From table 1.1 one can see that the scattering length of atoms varies linearly for x-rays but not for neutrons. This difference has implications for contrast and can be crucial if one is looking to locate a molecule or a specific part of a sample.

Table 1.1: **Comparison between scattering lengths of atoms for neutrons and x-rays.** adapted from [54]

Atom	Nucleus	b_{coh} (10^{-12} cm)	f_{x-ray} (10^{-12} cm)
Hydrogen	^1H	-0.3742	0.28
Deuterium	^2D	0.6671	0.28
Carbon	^{12}C	0.6651	1.69
Nitrogen	^{14}N	0.940	1.97
Oxygen	^{16}O	0.5804	2.25
Phosphorous	^{31}P	0.517	4.23

For example, the electron density profile of a phospholipid membrane obtained from x-ray reflectivity has two maxima which correspond to the electron rich phosphate groups of the lipid hydrophilic region, whereas two maxima also appear in neutron scattering length density profiles of protonated lipids, however they arise primarily from the carbonyl groups of the lipids [125].

Since electron rich elements scatter x-rays efficiently, in order to have contrast in x-ray experiments, one requires a sample with both regions of electron rich elements (such as Phosphorous) and electron poor elements (such as Hydrogen). This is useful when looking at membranes composed of phospholipids. As mentioned in section 1.1.3, phospholipids are lipids composed of two sections; multiple acyl hydrophobic tails and a phosphate containing hydrophilic head. The difference in the x-ray scattering lengths of CH_3 , CH_2 , CH and PO_3 groups allows one to visualize the head and tail regions of a phospholipid membrane.

By contrast, neutrons scatter as a function of the atom's neutron scattering length, b , which is composed of both coherent and incoherent scattering lengths. The coherent scattering length provides information about the structural arrangement of atoms, whereas the incoherent scattering provides information about the atoms' motions

within the sample. For the purposes of the experiments that will be discussed, only coherent scattering will be considered. Conveniently the scattering length of Hydrogen and its isotope, Deuterium, are very different and are of opposite sign as can be seen in Table 1.1. The negative sign associated with the scattering length of Hydrogen indicates that there is a 180° phase shift of the scattered neutrons as compared to neutrons scattered from elements with a positive scattering length. Consequently, one can label a region of a molecule with Deuterium to see where that region sequesters within a sample.

Similarly to the contrast obtained from PO_3 groups in x-ray experiments, neutron scattering experiments can obtain contrast in the headgroup region of phospholipids, as the carbonyl group, $\text{C}=\text{O}$, located at the division between a phospholipid's head and tail groups, has a large neutron scattering length due to the lack of Hydrogen with negative scattering lengths [126, 125].

1.2.2 Scattering Experiments Used to Investigate Membranes and Membranes Containing Cholesterol

Cholesterol is an important molecule in biomembranes and as discussed in section 1.1.5 and 1.1.6 has effects on the structure of the membrane. In addition to studying physical quantities of membrane structures alone, people have been interested in the effects of cholesterol, see Refs: [93, 51, 83, 75, 46, 45, 64, 27, 2, 8, 7, 5] to name a few. As mentioned in section 1.1.5, Pan et al. 2008 used x-ray scattering to investigate how cholesterol affected the membrane thickness, bending modulus and orientational order parameter of five phospholipids of varying length and degrees of unsaturation. They found that cholesterol, while increasing membrane thickness and orientational order

parameter as expected, did not do so with the same magnitude for each lipid species. Thickness and order increases were more pronounced for completely saturated lipids. Additionally, they found that cholesterol significantly increased the bending modulus of saturated lipids but barely increased the bending modulus for lipids containing one or two monounsaturated chains [93]. These changes were on the order of angstroms, and thus x-rays were an appropriate tool for the investigation. Cholesterol's thickening effect has also been investigated for different lipid species and associated with a condensing effect using x-ray scattering [51].

Mills et al. 2008 used x-ray in plane diffraction to investigate order parameters and the area per phospholipid of saturated and di-monounsaturated membranes containing cholesterol [83]. The saturated lipid was found to have a higher order parameter and a lower area per phospholipid compared to the di-monounsaturated lipid. Cholesterol was found to increase the order parameter and decrease the area per phospholipid in both membranes. These results suggest that unsaturation leads to increased fluidity, and cholesterol acts to decreases fluidity in the membrane to a greater extent for saturated lipids. Comparisons between the effects of cholesterol and its enantiomer have also been performed using x-ray diffraction and it was found that membranes containing either cholesterol or its enantiomer were structurally similar [75].

Neutron scattering is useful when contrast for a specific part of the sample or added molecule is desirable. Investigating the location and orientation of cholesterol is thus well suited to neutron scattering experiments. Harroun et al. 2006 were interested in finding the location and orientation of cholesterol in polyunsaturated lipid membranes. Using cholesterol labeled with deuterium in its polar region, cholesterol's

hydroxyl group was found near the hydrophilic head group region of a control monounsaturated POPC membrane, while at the center of a polyunsaturated DAPC membrane. To further investigate the orientation of cholesterol, a second experiment was performed with cholesterol containing a deuterium label on its hydrocarbon tail. The center of mass of the label was found at the center of the POPC membrane, consistent with a vertical orientation, called the canonical orientation, with respect to the membrane normal extending from the hydrophilic region of the phospholipid to the center of the membrane. Surprisingly, the tail label was also found at the center of the DAPC membrane consistent with a horizontal orientation, called the non-canonical orientation, of cholesterol at the center of the membrane [46]. Interestingly, the addition of POPC to a DAPC membrane with cholesterol was found to induce a change in cholesterol's orientation from lying at the center of the membrane to adopting a vertical orientation [64].

Scattering experiments were chosen for this work because of their usefulness in membrane structure determination. Physical quantities and their dependence on cholesterol content, such as the membrane thickness, area per phospholipid, order parameter and water penetration in both mitochondria-like and POPC membranes were probed with scattering experiments, while the orientation of cholesterol was estimated using a fluorescence technique called the dual ratiometric method and further verified using neutron reflectivity. The following chapter will outline experimental procedures as well as scattering theory relevant to the experiments.

Chapter 2

Experimental Methods

2.1 Sample Preparation

2.1.1 Reagents

All lipids were purchased from Avanti Polar Lipids Inc. located in Alabama, USA, with the exception of cholesterol and D₆-cholesterol, which were purchased from BioShop Canada Inc. and CDN Isotopes Inc. located in Quebec, Canada, respectively. Lipids include naturally extracted L- α -phosphatidylcholine (PC) (#840051C, Avanti), naturally extracted L- α -phosphatidylethanolamine (PE) (#84118C, Avanti), naturally extracted L- α -phosphatidylinositol (PI) (#840042C, Avanti), 1,2-dioleoyl-sn-glycero-3-phospho-L-serine (DOPS) (# 840035C, Avanti), 1',3'-bis[1,2-dioleoyl-sn-glycero-3-phospho]-sn-glycerol (TOCL) (# 710335C, Avanti) and 1-palmitoyl-2-oleoyl-sn-glycerol-3-phosphocholine (POPC) (#850457, Avanti). All phospholipids were purchased dissolved in chloroform.

All chemicals and salts were purchased from Caledon Laboratory Chemicals, located in Ontario Canada unless otherwise stated. For scattering experiments, prepared lipid samples are codisolved in chloroform and trifluoroethanol (TFE) in a 1:1 volume ratio. TFE was purchased from Sigma Aldrich Canada. A saturated salt solution of potassium chloride, KCl, was used to hydrate multilamellar samples to 83 % RH (see figure 2.1a) during x-ray experiments, while a saturated salt solution of potassium sulfate, K₂SO₄ was used to hydrate multilamellar samples to 97% RH (see figure 2.1b) during neutron experiments. Deuterated water, D₂O, was used for contrast in neutron experiments. D₂O was provided by AECL on site at the Chalk River NRU reactor. Dichloromethane was used to clean silicon wafers for x-ray experiments. Solutions of potassium chloride, KCl, magnesium chloride, MgCl₂, and HEPES were used to make a buffer for liposomes. These chemicals were purchased from BioShop Canada Inc.

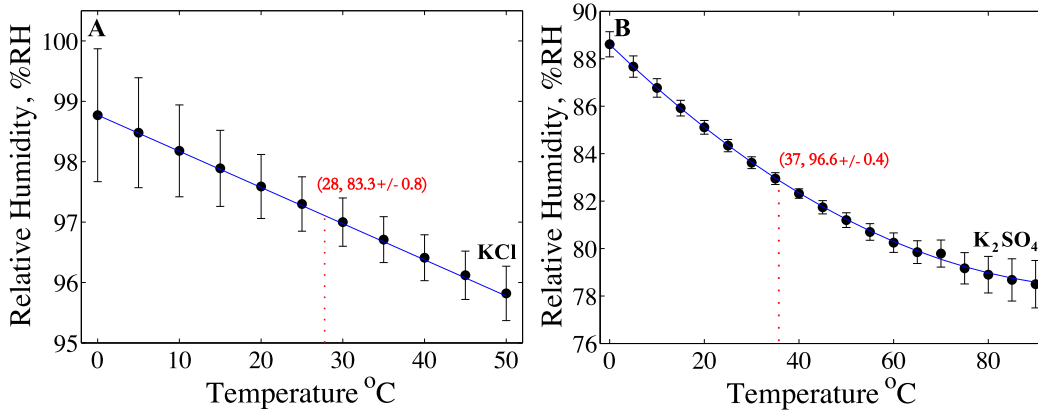


Figure 2.1: **Relative humidity as a function of temperature for KCl and K₂SO₄.** RH values for x-ray and neutron experiments were found from regressions on RH versus temperature plots for a) KCl: $RH = 0.0009T^2 - 0.1923T + 88.599$ and, b) K₂SO₄: $RH = -0.0599T + 98.772$. Data comes from Ref. [90].

Table 2.1: **Composition of the membranes examined in this study.** POPC, DOPS and TOCL were synthetic lipids. PC, PE and PI were obtained from natural extracts and had a distribution of acyl chains, as explained in the text. n_w and $\langle e_c \rangle$ are the number of water molecules associated on average with a phospholipid headgroup and the average number of electrons per chain for a given sample membrane respectively. These last two parameters are explained in section 2.2.4

Sample	POPC (mol%)	PC (mol%)	PE (mol%)	PI (mol%)	DOPS (mol%)	TOCL (mol%)	Cholesterol (mol%)	n_w	$\langle e_c \rangle$
POPC	100	—	—	—	—	—	—	7	245
Mito-like	—	48	28	10	10	4	0	6	237.9
Mito-like (10% chol.)	0	38	28	10	10	4	10	6	238.4
Mito-like (20% chol.)	0	28	28	10	10	4	20	6	238.9
Mito-like (30% chol.)	0	18	28	10	10	4	30	6	239.4

2.1.2 Membrane Preparation Composition

The mitochondria outer membrane was modelled using a combination of five phospholipids that previously have been shown to support Bcl-2 mediated pore formation [67]. The five lipid mitochondria-like membrane was composed of naturally extracted PC, PE and PI, and synthetically prepared DOPS and TOCL. Lipids were mixed following the molar ratios indicated in Table 2.1. The mitochondria-like membrane was compared to a simple one component membrane of POPC. Cholesterol was added to the mito-like membrane and was purchased as a powder from. In order to retain the desired charge and curvature of the mito-like membrane, PC a zwitterionic phospholipid with no inherent curvature, was removed from the mixture when cholesterol was added following the molar ratios for the mito-like samples with cholesterol in Table 2.1. Cholesterol was dissolved in chloroform prior to mixing with other phospholipids. X-ray experiments required 1.05 mg of lipid per sample, an example of the volumes of lipids used to give this mass is shown in table 2.2

Once lipids were mixed in the desired ratios following table 2.1 the chloroform solvent was evaporated under a steady stream of argon gas.

Table 2.2: **Volume of lipids required for x-ray samples.** X-ray samples required $\approx 1.05\text{mg}$ of lipid per sample. After mixing, the chloroform solvent was evaporated from the lipid mixture. This was then codissolved in chloroform and TFE in a 1:1 ratio at a concentration of 15mg/mL. Wafers could hold $\approx 70\mu\text{L}$ of solution during deposition, which at a concentration of 15mg/mL give 1.05mg of lipid on the wafer. POPC was also scanned for comparison with the complex mito membrane.

Lipid	Stock Concentration mg/mL	Volume (μL)			
		0 mol % CHOL	10 % CHOL	20 % CHOL	30 % CHOL
PC	25	19.4	16.1	12.5	8.5
PE	10	26.32	27.6	29.1	30.7
PI	10	11.8	12.4	13.4	13.8
DOPS	10	10.6	11.1	11.7	12.4
TOCL	10	7.9	8.3	8.7	9.2
CHOL	5	0	10.6	22.4	35.5

Neutron experiments required using a deuterium labeled cholesterol in addition to the cholesterol mentioned above. 2,2,3,4,4,6 D₆ cholesterol was chosen for the neutron experiments. Six hydrogens near the hydroxyl group are replaced with deuterium. D₆ cholesterol was purchased in powder form. Neutron experiments required 12 mg of total lipid per sample, an example of the volumes of each lipid required to give this mass are shown in table 2.3. Figure 1.3 shows chemical structures for all lipids.

2.1.3 Substrates

Lipid samples were deposited on silicon wafer substrates for scattering experiments following procedures outlined in [27]. For x-ray experiments these wafers were purchased pre cut from Silchem Handelsgesellschaft mbH, Germany. Wafers were laser cut into squares with a area of 1cm² and thickness of 300 μm . Grown using the Czochralski process, wafers had a (1 1 1) orientation and were polished on one side. Lipids were deposited on the polished side. Wafers were cleaned by sonification, immersed in a beaker of dichloromethane at 37°C for 30 minutes. After sonification,

Table 2.3: Volume of lipids required for neutron samples. Neutron samples required \approx 12mg of lipid per sample. After mixing, the chloroform solvent was evaporated from the lipid mixture. This was then codissolved in chloroform and TFE in a 1:1 ratio to give a concentration of 24mg/mL. The wafer could take \approx 0.5mL of lipid solution during deposition which at a concentration of 24mg/mL gives 12mg of lipid per sample.

Lipid	Stock Concentration mg/mL	Volume (μ L)				
		0 mol% CHOL	10% CHOL	10% D6 CHOL	20% CHOL	20% D6 CHOL
PC	25	221.2	193.6	183.8	159.7	142.5
PE	10	120.3	133.1	126.3	148.9	132.8
PI	10	54.0	59.7	56.7	66.8	59.6
DOPS	10	121.2	134.1	127.2	150.0	133.8
TOCL	10	89.9	99.4	94.3	111.2	99.2
CHOL	5	0	128.0	—	286.4	—
D6 CHOL	5	0	0	12.3	—	259.5

wafers were rinsed three times alternating water and methanol. If wafers were to be used immediately they were dried with nitrogen gas, and if they were to be stored, they were left immersed in methanol to avoid contact with organic contaminants.

Silicon wafers for neutron experiments were provided by AECL on site at the Chalk River NRU (National Research Universal) reactor. These silicon wafers were hand cut into rectangles with a $2.5 \times 6 \text{ cm}^2$ surface and 0.1cm thickness. They were cleaned with methanol and stored in methanol to avoid contact with contaminants until they were used.

2.1.4 Multilamellar Membranes Preparation

Multilamellar membranes on a solid supported substrate were desired for scattering experiments. Lipid samples were codissolved in chloroform and TFE. It was found that chloroform only as a solvent for the mitochondria-like mixture led to samples with a unhomogenous deposition. It was found that a 1:1 chloroform:TFE solvent solution dissolved the majority of the lipids in the mitochondria-like mix well, and thus the

lipid mixes were codissolved in this ratio. The codissolved lipids were then deposited on cleaned silicon wafers at 40°C using the “rock and roll” method described in [118]. For x-ray preparation, silicon wafers and a solid block of aluminum were heated to 40°C using a water bath. Both the aluminium block and the silicon wafer were placed in an inclosed rocker set to a speed and tilt of 1 and 20 respectively. 70 μ m of the desired lipid sample were deposited on the polished surface of the silicon wafer using a metal syringe. The rocker enclosure was then closed and the solvents were left to evaporate. Following evaporation, samples were placed in a vacuum at 37°C for three hours, and stayed in the vacuum overnight to remove all traces of the solvent. As the mitochondria-like mixture includes unsaturated lipids, samples were stored under argon or nitrogen gas to avoid oxygen contamination. Prior to experiments, samples were placed in an incubator set to 37°C in a sealed beaker with pure water to hydrate and anneal for 12 hours.

The rock and roll method was also used for the preparation of oriented multilamellar membranes for neutron experiments, however, the size of the wafer and the method of rocking was different. Lipid samples were prepared in the same way as for the x-ray experiments, however 12mg of lipid were required for deposition. Each wafer could take 0.5mL of solution before the solution would spill over the sides, so the desired concentration was 24mg/mL. Wafers and lipid solutions were heated to 40° on a plate heater. The silicon wafer was held as 0.5mL of the desired lipid mixture was deposited using a metal syringe onto to the surface of the wafer and then gently rocked in circles to evenly distribute the solution by hand as the solvents evaporated. Once the solvents had visually evaporated, the wafer was placed in a vacuum for 12 hours to remove any remaining solvent. Following vacuum evaporation, wafers were

Table 2.4: **Volume of lipids required for fluorescent liposome samples.** 1mg/mL liposomes were required. 1 mg of total lipid mix, following this table, was hydrated with 1mL of buffer as described in section 3.1.5.

Sample	Lipid	Concentration mg/mL	Volume (μL)				
			0 mol% CHOL	10% CHOL	20% CHOL	30% CHOL	40% CHOL
MITO	PC	25	18.1	15.0	11.6	7.8	3.5
	PE	25	10.3	10.8	11.4	12.0	12.8
	PI	10	11.1	11.7	12.3	13.0	13.8
	DOPS	10	10.0	10.5	11.1	11.7	12.3
	TOCL	10	7.4	7.8	8.2	8.7	9.1
	CHOL	5	0	10.1	21.1	33.4	47.1
	di-8-ANEPPS	0.5	7.3	7.7	8.1	8.5	9.0
POPC	POPC	25	39.8	37.7	35.3	32.65	29.7
	CHOL	5	0	10.7	22.6	35.8	50.7
	di-8-ANEPPS	0.5	7.8	8.2	8.7	9.2	9.7
DAPC	DAPC	25	39.9	37.9	35.7	33.2	30.3
	CHOL	5	0	9.9	20.9	33.3	47.5
	di-8-ANEPPS	0.5	7.2	7.6	8.0	8.5	9.1

placed in tubes with a drop of pure water and sealed. These tubes were left in an incubator set to 40° for 12 hours to hydrate and anneal. If wafers were not used immediately for an experiment they were stored under argon gas.

2.1.5 Liposomes

Fluorescence experiments were preformed on mitochondria-like liposomes. Liposomes were prepared by mixing the PC, PE, PI, DOPS, TOCL and the required cholesterol in the desired ratios following table 2.4 to give 1mg of total lipid. Chloroform was removed from the mixture under a steady stream of argon gas, and subsequently in a vacuum for three hours. Di-8-ANEPPS, a potentiometric fluorescent dye was added to the dried lipid mixture, and was purchased from InvitrogenTM. In order to avoid dye induced effects, the volume of dye added was approximately 1/200th of the volume of lipids used [21].

Samples were then hydrated with 1mL of 0.2M KCl, 1 mM MgCl₂ and 10mM HEPES at a pH of 7. Hydrated samples were freeze thawed ten times by placing

the samples in alternating baths of liquid nitrogen and luke warm water. Large unilamellar vesicles were formed by extruding the freeze thawed hydrated samples through a 100nm polycarbonate membrane (#610005, Avanti) using a liposome extruder (#610020, Avanti). Lipsomes were stored on ice and kept well for up to two days.

2.2 X-ray Apparatus and Experiment

2.2.1 Apparatus: BLADE

X-ray experiments were preformed in Maikel Rheinstädter's Laboratory for Membrane and Protein Dynamics at McMaster University in Hamilton, ON, Canada on the Biological Large Angle Diffraction Experiment (BLADE). BLADE is a Rigaku SmartLab X-ray diffractometer, with a 9kW (45 kV, 200mA) CuK α Rigaku SmartLab rotating anode. BLADE produces a parallel, monochromatic high intensity beam of x-rays with a wavelength of $\lambda = 1.54 \text{ \AA}$ and intensities up to $10^{10} \text{ counts/s} \times \text{mm}^2$. Samples are placed horizontally on an aluminium platform which remains stationary, while both the source and detector arms move vertically with angle θ with respect to the sample plane during the experiment. A schematic of the set up is shown in figure 2.2. The source arm can also move horizontally with angle ϕ with respect to the sample plane. Thus, a two dimensional intensity map of the sample's reciprocal space can be created, and both the vertical and lateral structure of the sample can be probed. The momentum transfer along the vertical axis, q_z , is in the range of $0.03 \text{ \AA}^{-1} < q_z < 1.1 \text{ \AA}^{-1}$, and the lateral momentum transfer, $q_{||}$, is in the range $0 \text{ \AA}^{-1} < q_{||} < 3.1 \text{ \AA}^{-1}$.

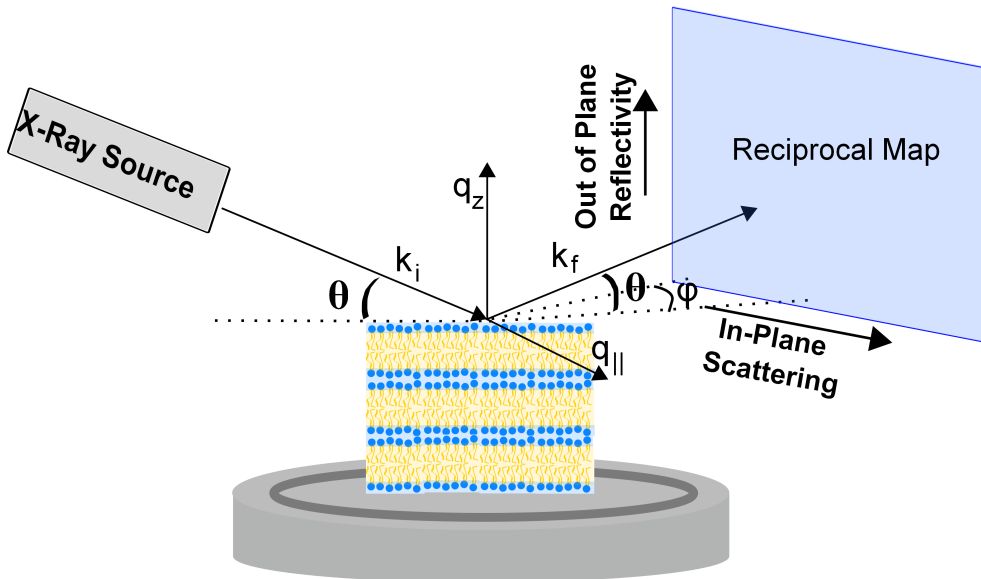


Figure 2.2: **Geometry of an x-ray scattering experiment.** In plane and out of plane diffraction experiments were performed on a multilamellar lipid sample by scanning along $q_{||}$ or q_z respectively. The detected intensity for both experiments creates a reciprocal map of the sample's structure.

2.2.2 Scattering Theory

X-rays, being a form of electromagnetic radiation, interact with the electrons of an atom. As such, during a scattering experiment, x-ray photons are scattered from the electrons of atoms within the sample and give information about the location of those electrons within the sample. Following figure 2.2, incident x-rays with wavevector k_i are scattered from the sample with wavevector k_f . The magnitude of the wave vectors depends on the wavelength, λ of the incident x-rays, $|k| = 2\pi/\lambda$. The scattering vector, also called the momentum transfer, \vec{q} , is defined as:

$$\vec{q} = \vec{k}_f - \vec{k}_i, \quad (2.1)$$

with magnitude:

$$|q| = \frac{4\pi \sin \alpha}{\lambda}. \quad (2.2)$$

The momentum transfer is therefore dependent on the geometry of the experiment via α , and the wavelength of the incident x-rays λ , where α is the angle between k_i and k_f , dependent on θ and φ from figure 2.2. It is worth noting that the direction of \mathbf{q} is completely governed by the direction of the incident beam, and the position of the detector, which allows for probing of different planes in the sample.

As a sample is composed of many atoms and thus of many electrons, the scattered x-rays interfere with one another. The intensity of scattered x-rays detected is dependent on this interference. The condition for constructive interference and therefore maximum intensity is given by Bragg's law:

$$2d \sin \theta = n\lambda, \quad (2.3)$$

where constructive interference occurs when the scattered waves remain in phase. The d in equation 2.3 is in general, the distance between planes of scatterers, or the lattice spacing in a crystal. In the case of lamellar samples, such as a stack of bilayers, d now represents the distance between two successive layers, d_z , if performed with an out-of-plane geometry. On the other hand, d becomes the average distance between chains, $d_{||}$, if performed with an in-plane geometry.

The diffracted intensity in an x-ray experiment is measured as a function of q , and maps the position of scatterers (electrons) in reciprocal space. The reciprocal variables are the form factor, $F(\vec{q})$ and the electron density, $\rho(\vec{r})$ of the sample.

2.2.3 Out of Plane, Reflectivity Experiments

Vertical structure within the sample can be probed by scanning the source and detector arms of BLADE along θ in a reflectivity scan. Reflectivity produces a series of Bragg peaks along q_z that allow for the determination of the lamellar thickness of the membrane samples. Following hydration in a container with pure water at 37°C for 12 hours, samples were placed in the centre of the aluminium platform. The aluminum platform has a well surrounding the sample location which was filled with a saturated KCl solution, producing an RH of 83%. An aluminum lid containing a kapton window, penetrable by x-rays, was placed over the platform sealing the sample environment. Sample alignment was performed automatically by BLADE; five variables, θ , z , ϕ , R_x and R_y were one by one varied to find the position of the sample. The value of each variable that gave the highest signal was set to be the zero position of the sample, such that the sample was positioned at the center of, and parallel to the x-ray beam. The samples were then allowed to equilibrate to the sample enclosure environment of 28°C and 83%RH created by the saturated KCl solution (see figure 2.1).

Short scans were taken periodically to monitor changes in Bragg peak positions. Once Bragg peak positions remained constant, samples were judged to be equilibrated. This equilibration time was found to be approximately 13 hours. Following equilibration, reflectivity and then in plane measurements were taken. A second reflectivity scan was performed after the in plane scan to insure the Bragg peak positions were still constant. Reflectivity scans involved BLADE incrementally increasing the angle θ of the source and detector arms simultaneously such that a 2θ scan geometry was accomplished.

Following the scans, samples were removed from the sample enclosure and stored

under argon gas. Samples were found to degrade due to oxygen exposure over time, and as such samples were only used once for experiments.

As the scattering of x-rays is dependent on the position of electrons within the sample, the integrated intensity obtained in reflectivity experiments can be related to the electron density of the sample via the form factor, $F(q)$ which is related to the sum of diffracted waves from every atom within the unit cell.

$$I(q_z) = \frac{|F(q_z)|^2}{q_z}, \quad (2.4)$$

where q is the Lorentz correction [16]. In reflectivity experiments the diffracted intensity is a function of q_z and is composed of a series of Bragg peaks. The average spacing between each peak, weighted by the peak order gives the lamellar spacing, d_z .

$$d_z = \frac{1}{n} \sum_n \frac{2\pi n}{q_n}. \quad (2.5)$$

The integrated area under the Bragg peaks is the intensity, I_n , in equation 2.4. The electron density profile of the sample can then be deduced from the variation of integrated intensity as a function of q_z using a 1-dimensional Fourier Transform.

$$\rho_u(z) = \frac{2}{d_z} \sum_{n=1}^N \nu_n \sqrt{I_n q_n} \cos\left(\frac{2\pi n}{d_z} z\right), \quad (2.6)$$

where $\rho_u(z)$ is the unscaled electron density profile along the vertical axis of the sample, N is the maximum number of observable Bragg peaks, $\sqrt{I_n q_n}$ is the form factor associated with each Bragg peak, ν_n is the phase of each form factor and d_z

is the lamellar spacing. v_n is not accessible directly through experiment, and its determination will be described below.

2.2.4 Reflectivity Analysis: Electron Density Scaling and Fitting, and Form Factor Phase and Membrane Thickness Determination

The form factor is in general a complex quantity, however, for centrosymmetric samples such a phospholipid bilayer, the form factors are reduced to real quantities with phases $v_n = \pm 1$. Following the sampling theorem of communication and its use in [60], the discrete values of the form factors should sample a continuous function $T(q_z)$. Phases can be determined by fitting experimentally obtained values of the form factors with the continuous function as has been done previously in [1].

$$T(q_z) = \sum_n \nu_n \sqrt{I_n q_n} \text{sinc}([d_z q_z - n]), \quad (2.7)$$

where the sum is over all discrete values of the form factors found experimentally. Once the phases are known, equation 2.6 is used to find $\rho_u(z)$.

In order to put the electron density profiles determined by Eq. (2.6) on an absolute electron density scale, the following scaling was used:

$$\rho(z) = a + b\rho_u(z). \quad (2.8)$$

The two scaling parameters were found assuming that the electron density in the centre of the lipid bilayer was equal to the density of a methyl group, $\rho_{\text{CH}_3} = 0.22 \text{ e}/\text{\AA}^3$, and that the integrated electron density over a single leaflet of the bilayer must be

equal to the expected average number of electrons per surface area given the known bilayer lipid composition and the measured area per chain, A_c :

$$\int_0^{d_z/2} \rho_u dz = \frac{\langle e_c \rangle}{A_c}. \quad (2.9)$$

The number of electrons per chain for each lipid, $e_{c,i}$, is approximated to be the total number of electrons per lipid, $e_{l,i}$ divided by the number of chains belonging to that lipid $n_{c,i}$, such that $e_{c,i} = e_{l,i}/n_{c,i}$. Where for PC, PE, PI and DOPS, $n_{c,i} = 2$, for TOCL $n_{c,TOCL} = 4$ and for cholesterol $n_{c,CHOL} = 1$. The average number of electrons per chain for a given sample, $\langle e_c \rangle$, listed in table 2.1 was then determined by a weighted sum of $e_{c,i}$ for a given sample membrane.

$$\langle e_c \rangle = \sum_i \left(\frac{M_i n_{c,i}}{\sum_i M_i n_{c,i}} e_{c,i} \right) + \frac{n_W e_W}{2}. \quad (2.10)$$

Where M_i and $n_{c,i}$ are the molar fraction and the number of chains for lipid i , respectively. Values of M_i for each sample mixture are listed in Table 2.1. The average number of water molecules associated with each phospholipid head group in a given sample membrane is n_W , and the number of electrons per water molecule is $e_W = 10$. Thus $n_W e_W / 2$ is the average number of electrons contributed by water molecules per chain. Since it was found that about seven water molecules associate on average with each POPC head group at a relative humidity of 83% [39], we considered here that $n_W e_W / 2 = 35$ electrons contributed by water molecules were associated on average with each phospholipid chain in the POPC membrane. However, it was found that the water layer associated with phospholipid head groups on one side of the membrane was $\simeq 2\text{\AA}$ thinner for the mito-like membrane as compared to the POPC membrane.

This difference corresponds to a loss of 3 water molecules per phospholipid, thus we used $n_W = 6$ for the mito-like membranes.

Combining Eqs. 2.8 and 2.9, and using the fact that the integral of the unscaled profile over half the bilayer is zero, we have:

$$a = \frac{2\langle e_c \rangle}{A_c d_z} \quad \text{and} \quad b = \frac{\rho_{CH_3} - a}{\rho_u(0)}. \quad (2.11)$$

In order to further characterize the electron density profiles, they were fit using Gaussian functions to represent the average electron density contributed by different components. This has been shown in simulations to provide a good description of a fluid membrane [4], and has often been used to interpret membrane diffraction data [125, 87, 62]. We used a single Gaussian peak to represent the head group region and its associated water molecules, and an inverted Gaussian peak to represent the chains terminal CH_3 region in the center of the membrane, as done previously in Ref. [62]. These Gaussian functions were set a top a constant baseline whose value then represents the acyl chain electron density in a dehydrated membrane, ρ_{CH_2} . Since the studied membranes were not fully hydrated and therefore did not necessarily have a significant layer of pure water between bilayers in the stack, no specific peak was attributed to a water layer, and instead, for each head group we included a Gaussian with the same amplitude and width, centered at $2d - z_h$ to represent the head group region of the neighbouring bilayer. The equation used to fit the electron density profile thus was:

$$\rho_z(z) = \rho_{CH_2} - H_c e^{-\frac{z^2}{2w_c^2}} + H_h \left(e^{-\frac{(z-z_h)^2}{2w_h^2}} + e^{-\frac{(z-(2d_z-z_h))^2}{2w_h^2}} \right). \quad (2.12)$$

In the above H_h and z_h are the amplitude and position of the Gaussian representing the head group region, and H_c is the amplitude of the Gaussian representing the terminal acyl chain region. w_h and w_c are the full width at half maximum (FWHM) of the Gaussians representing the head group and terminal acyl chain regions, respectively.

Once electron density profiles were calculated following equation 2.6, the thickness of the membrane was defined to be the headgroup to headgroup thickness, d_{hh} . This was determined by finding the distance between the position, z_h of each headgroup peak in the electron density profiles.

2.2.5 In Plane Scattering Experiments

In plane scans were performed at the same time as the reflectivity scans, so no further sample alignment was required. Following the first reflectivity scan, the source and detector arms moved back to their zero position, and the source arm traced out the angle ϕ from $\phi = 0^\circ$ to $\phi = 45^\circ$ in 0.16° increments while the detector arm remained stationary. Once the source arm reached it's maximum ϕ , it returned to it's start position at $\phi = 0^\circ$ and both the source and detector arms moved in θ . From this new θ position the ϕ scan is repeated, and following this the source and detector arms then move to a larger θ position. In this way, the scan builds up a two dimensional

map of the sample's reciprocal space.

Following the in-plane geometry of figure 2.2, the diffracted intensity is a function of $q_{||}$ and shows peaks corresponding to in-plane structures of the sample. In the case of lamellar membrane samples, there is a peak corresponding to the organization of the hydrocarbon chains, called the acyl chain correlation peak. The position of which can be related to the average distance between lipid chains and the area per lipid.

2.2.6 In Plane Analysis: Area per Phospholipid Chain and Acyl Chain Orientational Order Parameter

The acyl chain correlation peak, found around $q_{||} \approx 1.4 \text{ \AA}^{-1}$ was used to determine both the average area per chain and the chain order parameter. The in-plane peak profile as a function of $q_{||}$ was first generated by integrating the scattering data over a q_z range of $0 \text{ \AA}^{-1} < q_z < 0.3 \text{ \AA}^{-1}$. The peak position, $q_{T,||}$, was determined by fitting this profile with a Gaussian peak profile and a linear background. The average area per chain, A_c , was then calculated assuming the lipid tails form a densely packed structure with local hexagonal symmetry (planar group p6, as shown for instance by [6]), which leads to [84, 12]

$$A_c = \frac{8\pi^2}{\sqrt{3}q_{T,||}^2}. \quad (2.13)$$

The chain order parameter, $S_{\text{X-ray}}$, was determined using the out-of-plane peak profile as a function of the polar angle ϕ , as defined in Fig. 3.2, following the method outlined in Refs. [84] and [82]. Briefly, the out-of-plane peak profile was obtained by integrating the scattering data over a small $q_{||}$ range ($1.15 \text{ \AA}^{-1} < q_{||} < 1.55 \text{ \AA}^{-1}$)

(as illustrated in Fig. 3.2B). Assuming that the lipid chains can be modeled as straight rods with a distribution of tilt angles following a Maier-Saupe distribution, $f(\beta) \propto e^{m \cos^2 \beta}$, the out-of-plane chain correlation peak was fit with the following expression [84]:

$$I(\phi) = I_b + \frac{C}{8} \frac{\sqrt{m}}{e^m D(\sqrt{m})} e^{\frac{m \cos^2 \phi}{2}} I_0\left(\frac{m \cos^2 \phi}{2}\right). \quad (2.14)$$

In the above, I_0 is the modified Bessel function of the first kind, D is Dawson's integral, I_b is the background intensity, and C is a constant accounting for the amount of sample contributing to the scattering, beam intensity and exposure time. The parameter m describing the width of the chain angular distribution is directly related to the chain orientational order parameter, $S_{\text{X-ray}} = \frac{1}{2}(3\langle \cos^2 \beta \rangle - 1)$, through [84]:

$$S_{\text{X-ray}} = \frac{1}{2} \left(3 \frac{\int_0^\pi 2\pi \sin \beta \cos^2 \beta e^{m \cos^2 \beta} d\beta}{\int_0^\pi 2\pi \sin \beta e^{m \cos^2 \beta} d\beta} - 1 \right). \quad (2.15)$$

2.3 Neutron Apparatus and Experiment

2.3.1 Apparatus: N5 Triple Axis Spectrophotometer

Neutron experiments were performed on the N5 beamline at the Canadian Neutron Beam Centre (Chalk River, Ontario, Canada). N5 is a triple axis spectrometer that uses the thermal neutron source of the NRU reactor. A triple axis spectrometer, as its name implies has three axes; the monochromating crystal, the sample and the analyzer crystal. Although, N5 is a triple axis setup, the analyzer was removed as the contributions to the detected scattering intensity from wavelengths other than λ chosen from the monochromator, are so small as to be negligible. As shown in

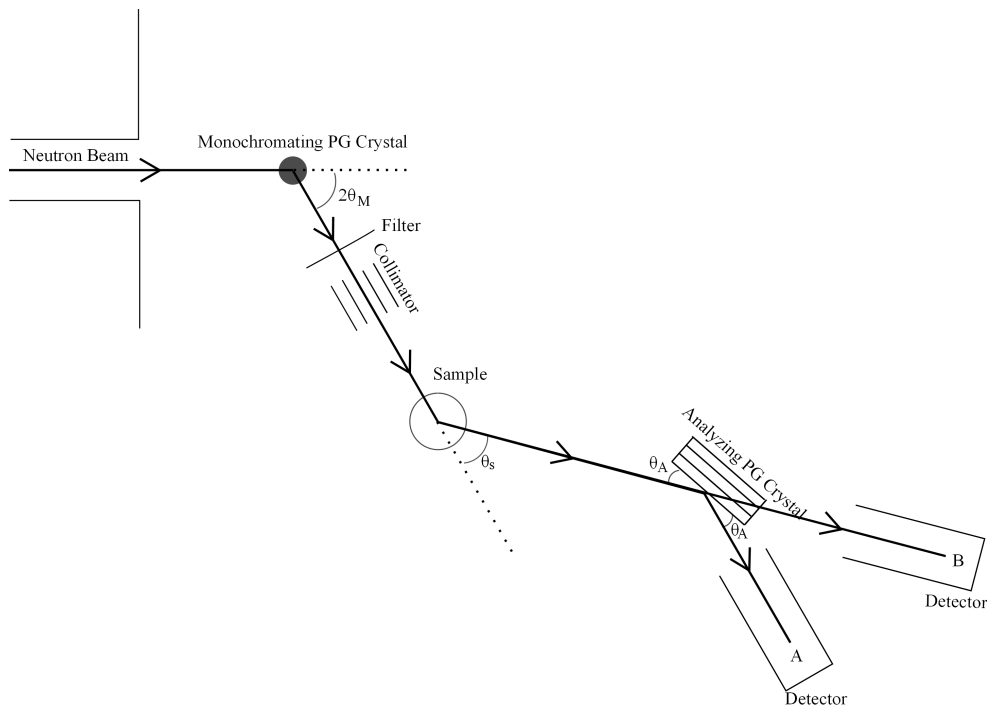


Figure 2.3: Geometry of a neutron triple axis spectrometer with and without an analyzer crystal. A) Neutrons exit from the reactor and diffract from the monochromating PG crystal. The neutron beam is collimated before interacting with the sample. Following diffraction from the sample, the neutrons are diffracted by an analyzer crystal and enter the detector. B) Following diffraction from the sample, neutrons are detected without scattering from an analyzer crystal. Setup B was used for the preset neutron reflectivity experiments.

Figure 2.3B, neutrons exit the reactor as a polychromatic beam and hit a monochromating pyrolytic graphite (PG) crystal, which, due to Bragg reflection, selects out a specific wavelength/energy of neutrons. These monochromatic neutrons then hit the sample and scatter.

The wavelength of selected neutrons for the monochromator depends on the crystal and the angle 2θ . The monochromating crystal was set up to give a wavelength of $\lambda = 2.37\text{\AA}$.

2.3.2 Scattering Theory

Neutron reflectivity was chosen, as it provides information about the vertical structure of the membrane, the location of various chemical groups of the lipids in the membrane as well as the location of added molecules if the correct contrast methods are used. Neutron reflectivity has similar geometry to x-ray reflectivity, in that the intensity of detected neutrons is a function of the vertical momentum transfer, q_z , which is related to the incident beam angle, θ , and the wavelength of the incident neutrons, λ , following equation 2.1. The goal of the experiment is to convert the detected neutron intensities over a range of q_z , via discrete fourier transforms, into meaningful vertical maps of the sample's neutron scattering length density profile. These maps contain information about the membrane's thickness, water penetration, and the location of molecules within the membrane. The raw data is in the form of repeating Bragg peaks, indicating regions of constructive interference due to the layering of the membranes. The integrated intensities of each of the Bragg peaks are background subtracted and corrected following procedures outlined in [45] and [66], for incident flux, C_{flux} , absorption from the sample, C_{abs} and the Lorentz correction, C_{lorz} .

The flux of neutrons incident to the sample varies as a function of the incident beam angle with the sample, θ , due to the Gaussian shape of the beam. This flux correction can be written as follows where σ is the Gaussian width and L is the length of the sample along the direction of the beam:

$$C_{flux} = 1/\text{erf}\left(\frac{L\sin\theta}{\sqrt{8}\sigma}\right). \quad (2.16)$$

Once the neutrons reach the sample, they are diffracted as well as absorbed. The

absorption of neutrons by the sample, C_{abs} , depends on μ , the absorption coefficient, and t is the thickness of the sample:

$$C_{abs} = \frac{2\mu t / \sin\theta}{1 - \exp(-2\mu t / \sin\theta)}. \quad (2.17)$$

μ is found by assuming each molecule within the unit cell of the sample occupies a certain volume, while t is estimated assuming the amount of lipid used to make the sample is 12 mg giving a thickness of 0.001cm. The final correction, the Lorentz correction is given by:

$$C_{Lor} = \sin(2\theta). \quad (2.18)$$

The form factor for each Bragg peak is then calculated from the corrected integrated intensities as:

$$F_n = \nu_n \sqrt{C_{flux} C_{abs} C_{Lor} I_n}, \quad (2.19)$$

where the subscript n is an integer which refers to the order of the specific Bragg peak, and ν is the phase of the form factor. Determination of ν is described in section 2.3.5. The unscaled neutron scattering length density profile, ρ_z , is calculated by taking the discrete Fourier transform of the set of form factors following:

$$\rho(z) = 2 \sum_{n=1}^{n_{max}} F_n \cos(2\pi z n / d), \quad (2.20)$$

where z is the direction normal to the plane of the sample, thus the lateral direction of the membrane, and d is the lamellar spacing of the sample. The absolute scaling

of $\rho(z)$ is explained in section 2.3.6

2.3.3 Rocking Scan

Samples were tested for orientation quality by performing a rocking scan. The rocking scan measures the intensity of detected neutrons as a function of the sample's angle with the incoming neutron beam, ψ ($\psi=\theta_s/2$ in figure 2.3). There should be a peak centered about the angle where the neutrons are diffracted in phase. It is typical of multilamellar lipid samples to have a narrow Bragg peak and a broader diffuse scattering in the rocking curves. The width of the narrow peak gives information about the quality of the sample's orientation over long ranges. The wider the peak, the greater the spread of the bilayer orientation angles. If the sample was perfectly oriented, the rocking scan would give a delta function as opposed to a widened peak. The diffuse scattering arises from local deviations from the average bilayer structure and thus represents short range order [58]. Rocking scans were performed on each sample in 100% D₂O contrast solution, as it has the highest intensity of detected neutrons as described further in the following section. Figure 2.4 shows the three geometries that highlight the features of a rocking scan.

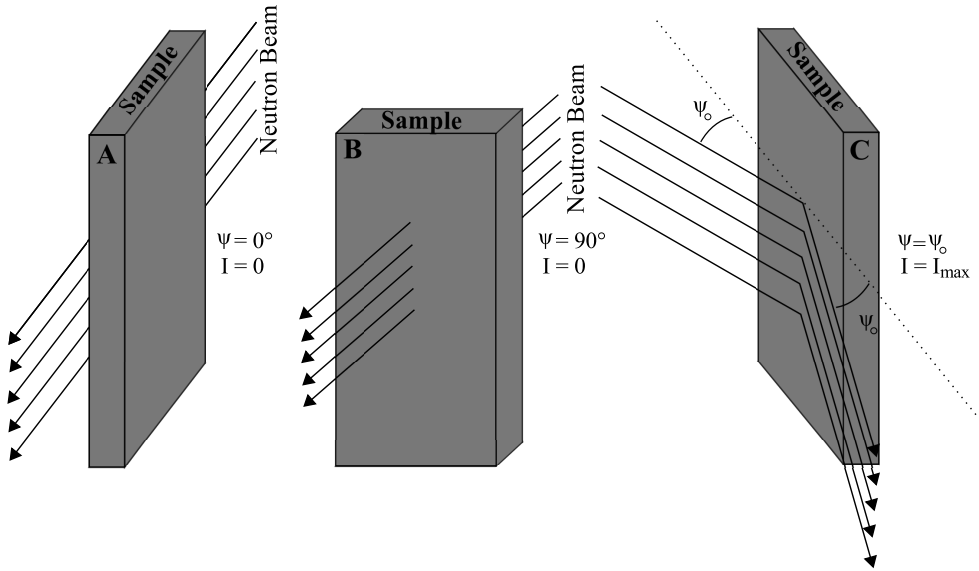


Figure 2.4: **Rocking Scan Geometries.** a) The intensity of detected neutrons is zero when the sample is oriented parallel to the neutron beam, $\psi=0^\circ$. b) The intensity of detected neutrons is again zero when the sample is oriented perpendicular to the neutron beam, $\psi=90^\circ$. c) The intensity of detected neutrons is a maximum when the sample is oriented such that the diffracted neutrons interfere constructively, $\psi=\psi_o$.

2.3.4 Reflectivity Experiment

Prior to reflectivity experiments, samples were hydrated with a saturated K_2SO_4 contrast solution composed of H_2O/D_2O in various ratios, for 8-16 hours in a $37^\circ C$ incubator. A reflectivity experiment allows one to look at the neutron scattering length density of a sample. Multilamellar membrane samples are essentially stacks of membranes. For hydrated samples, such as those in this study, a water layer exists between each membrane and the next, provided by the hydrating medium in the sample container. At 8% D_2O , the scattering length of the water layer between bilayers, composed of 8% D_2O , has an effective value of 0 therefore the detected scattering comes only from the membrane component of the sample. At higher concentrations

of D₂O, the water layer becomes has a non-zero effective scattering length and therefore contributes to the detected scattering. At 100% D₂O, the highest intensity of neutrons is detected, thus rocking scans are performed at this contrast concentration. Four D₂O concentrations were used; 8%, 40%, 70% and 100%.

There were four sample containers available, each containing one of the four contrast solutions of H₂O/D₂O, and three container lids which could each hold a sample. The lids, each holding a sample would be rotated to each of the containers such that each sample was scanned in all four contrast solutions. While one container and sample was being scanned, the two other samples were hydrated in two remaining containers inside an incubator set to 37°C. Following a scan, the sample would be placed in the last container, and one of the hydrating samples would be scanned. In this way, all samples were scanned in all four contrast solutions, and a new sample could be scanned at each change over thus making it as time efficient as possible.

During the scan, a container holding a sample was placed vertically in the center of a heated rotating sample platform. A sealed aluminum container was then placed around the sample container and a pump was used to create a vacuum. Temperature probes inside the aluminum container allowed one to monitor the temperature of the sample. The sample was kept at $37 \pm 1^\circ\text{C}$ for the duration of the reflectivity scan. Once the sample was in place it was allowed to equilibrate with the temperature after having been removed from the incubator and placed one the sample platform. During this time, which was approximately 30 minutes, the sample was aligned. Alignment involved finding the position of each of three variables that gave the highest neutron intensity detected. These three variables are the angular position of the sample with respect to the neutron beam, θ , the horizontal position of the sample, x , and finally

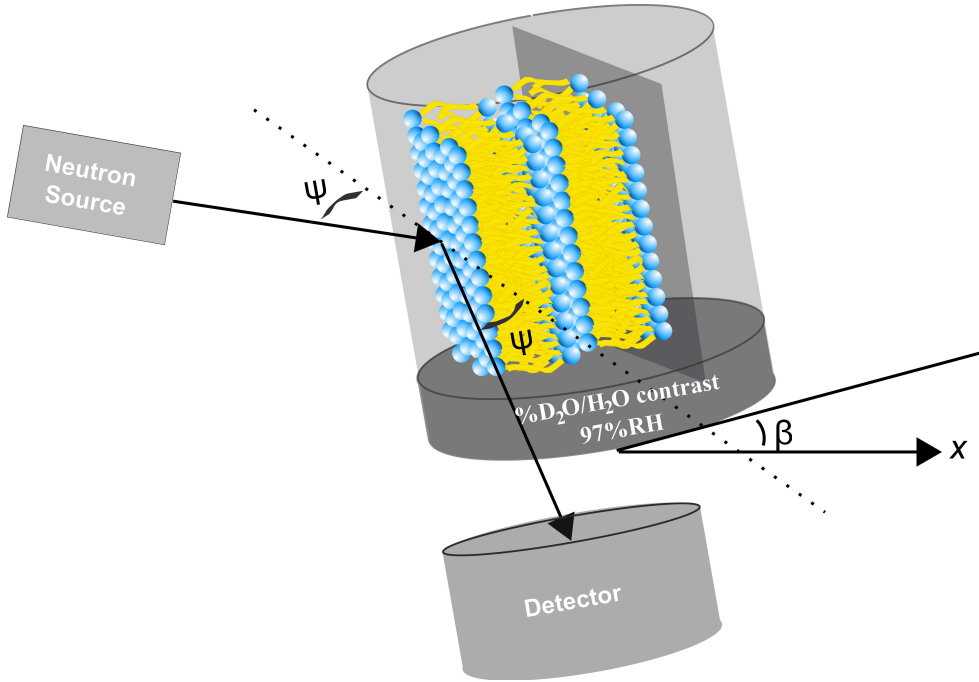


Figure 2.5: Neutron reflectivity alignment geometry. Sample containers were mounted on a stage that could control the angle between the sample plane and the neutron beam, ψ , the horizontal position of the platform, x as well as the tilt angle of the platform, β . Each of these variable was set to be zero at the value that gave the largest scattering intensity. See text for details.

the tilt of the sample platform, β , all shown schematically in figure 2.5. Alignment was started by first scanning the sample in increments of ψ , and fitting the resulting data with a Gaussian in order to find the position of ψ which gave the highest neutron intensity. The position was then set to zero and scans varying x and β were performed to find their zero positions. This was done a few times in order to be as aligned as possible. Following alignment the reflectivity scan could be started. The computer was programmed to run the scan numerous times over the period of 4-8 hours. The raw data was analyzed, and any Bragg peaks from the first few scans that had a different position than their later Bragg peaks were discarded as this indicated that the sample was not yet equilibrated to the temperature.

2.3.5 Form Factor Phase Determination

Form factor phases are obtained by using saturated salt contrast solutions, each made up of a different D₂O/H₂O ratio and a salt to hydrate the sample. Hydration of the sample introduces a water layer between each bilayer. This method for phase determination is outlined in both [66] and [69], and depends on the linear relationship between form factors and D₂O content in the water layer between bilayers. By performing a reflectivity scan on a sample in four different contrast solutions, for each Bragg order one can plot the amplitude of the form factor as a function of D₂O concentration in H₂O, this has been done for our samples in figure A.2, and for the mito-like sample in figure 2.6. As the diffracted intensity will linearly increase or decrease with the addition of D₂O depending on the phase of F(n), the slope of the line connecting F(n) as a function of D₂O content, $\rho(n)$ can be defined as:

$$\rho_n = F_n(D_2O) - F_n(H_2O), \quad (2.21)$$

$$\rho_n = \int_{-d_z/2}^{d_z/2} \Delta\rho(z) \cos\left(\frac{2\pi nz}{d}\right) dz, \quad (2.22)$$

where $\Delta\rho(z)$ is the difference in SLD profiles for samples measured in D₂O and those measured in H₂O. Lipid bilayers, when at a relative humidity between 80 and 95%, do not change their structure appreciably with changes in interbilayer water layers [59], therefore $\Delta\rho$ is the SLD profile of water molecules ($\Delta\rho = \rho_w$). By approximating ρ_w to first order as the sum of two error function positioned at the water-bilayer interface [61]:

$$\rho_w = \operatorname{erf}(-d_{hh}/2) + \operatorname{erf}(d_{hh}/2), \quad (2.23)$$

(where d_{hh} is the bilayer thickness and $d_z = d_{hh} + d_w$), equation 2.22 can be integrated to give:

$$\Delta\rho = \rho_w = (-1)^n d_z \frac{(\rho_{H_2O} - \rho_{D_2O})}{\pi n} \sin\left(\frac{\pi n d_w}{d_z}\right) \exp\left(-2\left(\frac{\pi n \sigma_w}{d_z}\right)^2\right), \quad (2.24)$$

where $d_w/2$ is half the thickness of the water layer between adjacent bilayers, $\rho_{H_2O} - \rho_{D_2O}$ is the SLD difference between D₂O and H₂O, and σ_w is the width of the water probability error function, all of which are parameters that are used to fit equation 2.24 to values of $\rho(n)$ calculated from form factor data. Such a fit for our samples is shown in figure A.1, and for the mito-like sample in figure 2.6. Once $\rho(n)$ is known, phases, $\nu(n)$, are chosen such that the F(n) fall on a line with slope $\rho(n)$ predicted by equation 2.24.

Plots of F(n) versus D₂O content for each diffraction order and each sample are shown in figure A.2 and values of F(n) can be found in table A.3.

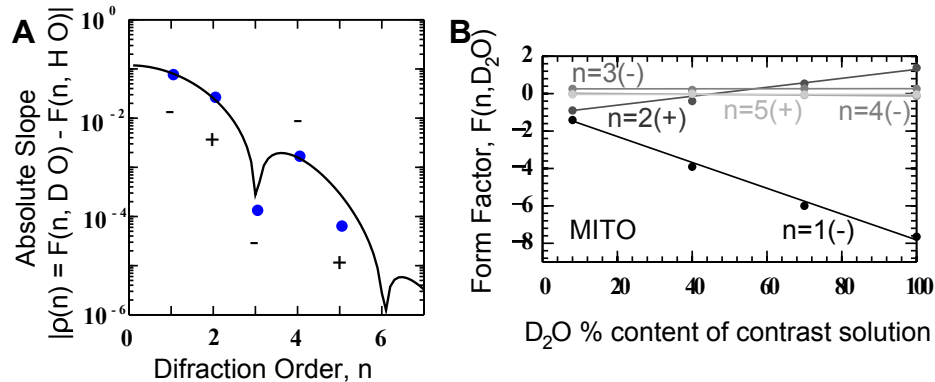


Figure 2.6: **Form factor determination** .A) Semi-log plots of the absolute slope, $\rho(n)$ predicted from equation 2.24, and experimental form factor data for the mito-like sample. The signs of the form factors are shown above or below the data, and alternate in sign until a dip in the theoretical curve after which the alternation starts again. The first sign must be negative as that produces the "U" shape in the NSLDs characteristic of a bilayer. $\rho(n) = [- + - - +]$. B) Data points represent form factors calculated from reflectivity data following equation 2.19, while lines are a fit, whose slopes are the data points from A). The slope of each line then determines the sign of each form factor, and thus the form factor phases, ν_n . Form factors of the mito-like sample for each of five diffraction orders are displayed.

2.3.6 Reflectivity Data: Scaling Neutron Scattering Length Density Profiles

Using equation 2.20, $F(n)$ were Fourier transformed to give the NSLD profiles of the membranes. Scaling was done by making assumptions similar to those used for scaling of the x-ray electron density profiles (2.2.4). The first assumption is that the center of the membrane is composed of 30% CH_3 , and 70% CH_2 groups with $\rho_c = -4.70E^{-7}$, the second is to estimate the forward scattering form factor F_0 , based on the scattering lengths of the components of the lipid sample.

$$F(0) = \frac{2(b_L - \rho_w V_L)}{A_L}, \quad (2.25)$$

where V_L , b_L and A_L are the volume, scattering length and area of the unit cell respectively. V_L and A_L are estimated constants and are listed in table 2.5. b_L is estimated from the scattering length of the mito-like lipids and from cholesterol, $b_L = x_{MITO}b_{MITO} + x_{CHOL}b_{CHOL}$. Each in turn is estimated by summing their major scattering components:

$$b_{MITO} = \sum_i n_i b_i, \quad (2.26)$$

$$b_{CHOL} = b_O + 27b_C + 46b_H, \quad (2.27)$$

where i are the scattering components PC, CH₃, CH₂ and CH, n_i are the number of scattering components in a unit cell, and x_{MITO} and x_{CHOL} are the molar fractions of mito-like lipids and cholesterol in each sample.

Scaling was then accomplished using:

$$\rho_s(z) = \rho_w + \frac{F(0)}{d} + \left(\frac{\rho_c - \rho_w - \frac{F(0)}{d}}{\rho(z=0)} \right) \rho(z), \quad (2.28)$$

where $\rho_s(z)$, $\rho(z)$ and ρ_w are the scaled, unscaled and water NSLDs respectively. ρ_w is found by weighting the NSLDs of H₂O and D₂O based on the contrast solution:

$$\rho_w = x_{D_2O}\rho_{D_2O} + x_{H_2O}\rho_{H_2O}, \quad (2.29)$$

where x_{D_2O} and x_{H_2O} are the fractions of D₂O and H₂O in each contrast solution. Parameters used to scale NSLDs are listed in table 2.5

Table 2.5: **Structural parameters used to scale $\rho(z)$ for bilayers.** A_L , V_L and b_L are the area, volume and scattering lengths respectively.

Sample	A_L (Å ²)	V_L (Å ³)	b_L (Å ⁻²)
POPC	62.3	1262.3	3.36E-4
Mito-like	68	1262.3	3.36E-4
Mito-like (10% H chol)	68.1	1332.6	3.51E-4
Mito-like (10% D chol)	67	1332.6	3.51E-4
Mito-like (20% H chol)	68	1420.5	3.69E-4
Mito-like (20% D chol)	79.2	1420.5	3.69E-4

2.4 Fluorescence Apparatus and Experiment

2.4.1 Apparatus: TECAN Spectrophotometer

Dual ratiometric fluorescence data was collected using a Tecan M1000 multiplate reader spectrophotometer located in the Biophotonics facility at McMaster University, Hamilton, ON, Canada.

2.4.2 Dual Ratiometric Method Theory

The location and orientation of molecules within a membrane can be determined by providing contrast to an experiment. For example one could label an area of the molecule with an electron rich atom and perform x-ray reflectivity as has been done, for example, in [100]. One could also label an area of the molecule with Deuterium and perform neutron reflectivity as described in section 1.2.1. The first option can be difficult depending on the molecule in question, as adding an electron rich atom could change the chemical behavior of the molecule as well as its potential interaction with the membrane. The second option, which is often employed, see for example [45], has high resolution and is trusted, however it requires a neutron source and beam time which involves proposals and waiting time. Instead one can use the dual ratiometric

fluorescence method to determine the orientation of a molecule by monitoring the dipole potential of the membrane with a potentiometric probe.

Phospholipid membranes have a transmembrane electrical potential, $\Delta\Psi$ which is defined as the difference in potential from one side of a membrane to the other. Each monolayer in the membrane has its own dipole potential ψ_d , and when the membrane is symmetric in its composition, the transmembrane potential is zero. The dipole potential of a monolayer comes from the dipoles of the lipid headgroups, the oriented water molecules in the headgroup region as well as from the carbonyl bonds of the ester linkages between the head group and hydrocarbon chains [38, 15, 98].

A molecule, such as cholesterol, with a dipole moment, will either contribute to the membrane's dipole potential or not when embedded within a membrane depending on its orientation. Cholesterol's dipole moment is oriented in the direction of it's polar hydroxyl group, thus measuring ψ_d gives information on the molecular orientation of cholesterol.

In order to do such an experiment, a probe is required to monitor the dipole potential. Di-8-ANEPPS is a potentiometric fluorophore that is sensitive to changes in the membrane potential. The excitation profile of the fluorophore changes with changes in the membrane potential. Excitation intensities at two discrete wavelengths can be measured at the same emission wavelength, and the ratio of these intensities, R , changes linearly with dipole potential [21, 43]:

$$\psi_d = mR + b \quad (2.30)$$

where m , the slope, and b , the intercept, must be found by calibrating experimental values of R with values of ψ_d found in literature.

2.4.3 Dual Ratiometric Method Experiment

A quartz 96 well plate was used for this experiment. $300\mu\text{L}$ of liposomes were pipetted into each well and contained a small amount of di-8-ANEPPS. For each experiment, liposomes without di-8-ANEPPS were also scanned to provide a measure of background fluorescence. The Tecan was programmed to excite the fluorescence of the liposomes at both 420nm and 520nm and to detect fluorescence around 670nm. The bandwidth for both was set to 5nm, the gain was manual, and the plate was read from the top. The choice of excitation and emission wavelengths was found in [22] to avoid any fluidity effects of the membrane on the dipole potential. Additionally it was found that the temperature must be above the transition temperature for the lipids to allow the fluorescent ratio to be independent of membrane fluidity [22]. As scans were taken at both room and body temperature, the latter was taken only after the liposomes were allowed to equilibrate to 37°C ; once the liposomes reached 37°C , the scans were performed every minute until the data stopped changing. The value of R was found following:

$$R = \frac{(I_{420} - I_{b,420})}{(I_{520} - I_{b,520})}, \quad (2.31)$$

where I_{420} , $I_{b,420}$, I_{520} and $I_{b,520}$ are the fluorescence intensities measured at 420nm and 520nm. The subscript b indicates the measurement of the background fluorescence from samples without di-8-ANEPPS.

2.4.4 Calibration

Calibration is required to relate the value of R to the dipole potential, ψ_d . The calibration is done by measuring R for a number of samples for which ψ_d is known to determine m and b from equation 2.30. In our case we used POPC with $\psi_d=363\text{mV}$ [44] and DAPC with $\psi_d=214\text{mV}$ [44] as well as POPC with various amounts of cholesterol. The values of ψ_d for these samples as a function of the measured value of R using our set up are plotted in figure 2.7. A linear fit of this data allows determination of the values of m and b , which leads to the relationship between R and ψ_d :

$$\psi_d = 83.3R + 108.3. \quad (2.32)$$

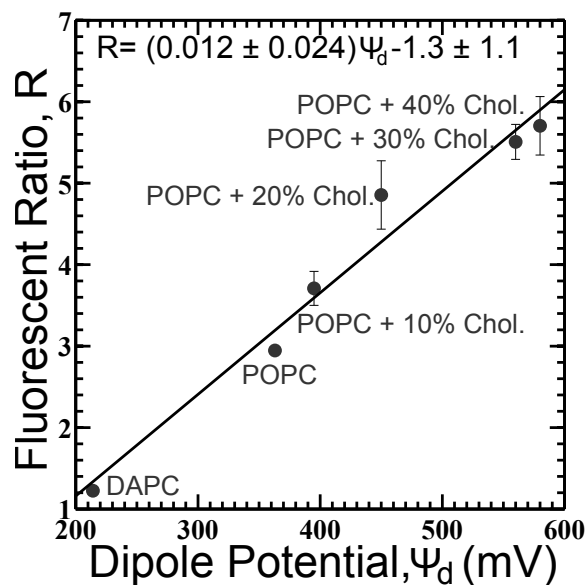


Figure 2.7: **Calibration of fluorescent R to dipole potential, ψ_d .** Data points represent values of R measured in our experiment for different samples as a function of the known values of ψ_d from the literature [44]. The line is a linear fit to the data, $R = (0.012 \pm 0.024)\psi_d - (1.3 \pm 1.1)$. Error bars represent standard deviations from three independent R measurements

Chapter 3

Results

3.1 Dual Ratiometric Fluorescence Results for Cholesterol Orientation in Mito-like Membranes

In saturated membranes, cholesterol is known to orient itself with its hydroxyl group near phospholipid carbonyl groups, and its hydrocarbon chain with the hydrocarbon chains of the phospholipids. This orientation is known as the canonical orientation, and has been observed using both neutron and NMR studies [45, 69, 77]. By contrast, when placed in a membrane composed of polyunsaturated lipids, cholesterol takes on a non-canonical orientation, lying flat in between bilayer leaflets, at the center of the membrane [46]. The canonical orientation would see cholesterol contributing to the dipole potential of the membrane, while the non-canonical orientation would see no contribution, as cholesterol's dipole would be directed, on average, at a normal to the membrane dipole potential. By monitoring the change in membrane dipole potential as a function of cholesterol content, one can determine which orientation cholesterol

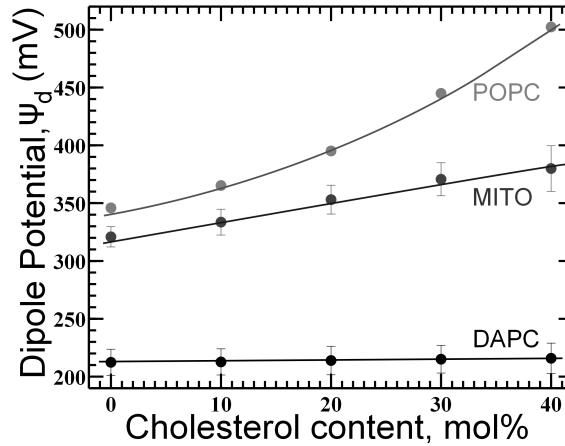


Figure 3.1: **Dipole potential as a function of cholesterol content.** Data points represent ψ_d values calculated using equation 2.32 for three independent trials (mean \pm standard deviation). Curves are guides to follow the trend and not fits.

adopts. In order to determine the orientation of cholesterol in a mito-like membrane, we performed fluorescent experiments utilizing the dual ratiometric approach on POPC membranes (acting as a positive control), DAPC membranes (acting as a negative control) and on the mito-like membrane. The results of three independent trials are shown in figure 3.1.

DAPC is a polyunsaturated lipid in which cholesterol is known to adopt a non-canonical orientation [46]. When cholesterol is incorporated into the DAPC membrane it sits horizontally with its dipole moment oriented perpendicular to the dipole moment of the lipids, thus not contributing to the overall dipole potential of the membrane. Figure 3.1 shows that ψ_d for DAPC is unchanged as a function of cholesterol content which is to be expected, and resembles curves produced previously [44]. In contrast, ψ_d for POPC, a monounsaturated lipid, is seen in figure 3.1 to increase as a function of cholesterol content. This is also to be expected as cholesterol is known to adopt a canonical orientation in POPC membranes, thus contributing to ψ_d . The

trend for ψ_d as a function of cholesterol is similar to what was found in [44], with what appears to be a non-linear relationship. In contrast, the ψ_d for the mito-like membrane increases with cholesterol with what looks to be a linear relationship. If cholesterol were sitting in a non-canonical orientation, the mito-like curve would be expected to match the DAPC curve, which it does not. Therefore figure 3.1 suggests that cholesterol has some sort of distribution of orientations in a mito-like membrane. Additional techniques are required to precisely determine cholesterol's orientation.

3.2 X-Ray Diffraction Results

In order to probe the molecular structure of mito-like membranes, we prepared stacks of highly oriented membranes, which we examined using 2-dimensional x-ray diffraction. The precise lipid compositions of all the membranes examined in this study are given in Tables 2.1 and 2.2. The membranes were studied at $T = 28^\circ\text{C}$ and $83.6 \pm 0.3\%$ relative humidity to emphasize their structural features. In this partially dehydrated state the increased number of higher order Bragg peaks allows reconstructing high resolution electron density profiles for the membranes. The membrane stacks were placed inside the diffractometer as shown in Fig. 3.2A, and diffraction data covering a large area of reciprocal space was collected.

For a quantitative analysis of the diffracted intensity, the 2-dimensional intensity maps recorded during an experiment were cut along three different axes, as illustrated in Fig. 3.2B. The three types of one-dimensional scattering data give access to different structural parameters, as described in detail in sections 2.2.3 and 2.2.5. The in-plane scattering data along $q_{||}$ (wide-angle x-ray scattering) contains information about the packing of the lipid acyl chains, where the average surface area occupied by an acyl

chain, A_c , can be determined from the position of the broad chain-correlation peak observed at $q_{\parallel,T} \approx 1.4 \text{ \AA}^{-1}$ [117, 12]. Note that two additional peaks are seen in the in-plane scattering data, that are not related to the stacked membrane structure: The Kapton window of the hydration chamber leads to scattering at $q_{\parallel} \approx 0.3 \text{ \AA}^{-1}$, while the silicon substrate leads to scattering at $q_{\parallel} \approx 2.75 \text{ \AA}^{-1}$ and $q_z \approx 2.8 \text{ \AA}^{-1}$. The out-of-plane scattering along q_z (reflectivity data) showed a series of 8 to 9 Bragg peaks, which were used to reconstruct the average transverse electron density profile of the membranes as described in section 2.2.2. [125, 87, 37, 91, 12, 116]. Finally, the profile of the chain-correlation peak plotted as a function of the polar angle ϕ , i.e. along the arc defined by the constant scattering wave vector amplitude $q = q_{T,\parallel}$ in the (q_{\parallel}, q_z) plane, allows estimating an orientational order parameter for the lipids carbon chains where the more disordered the lipid acyl chains, the broader the chain-correlation peak [84].

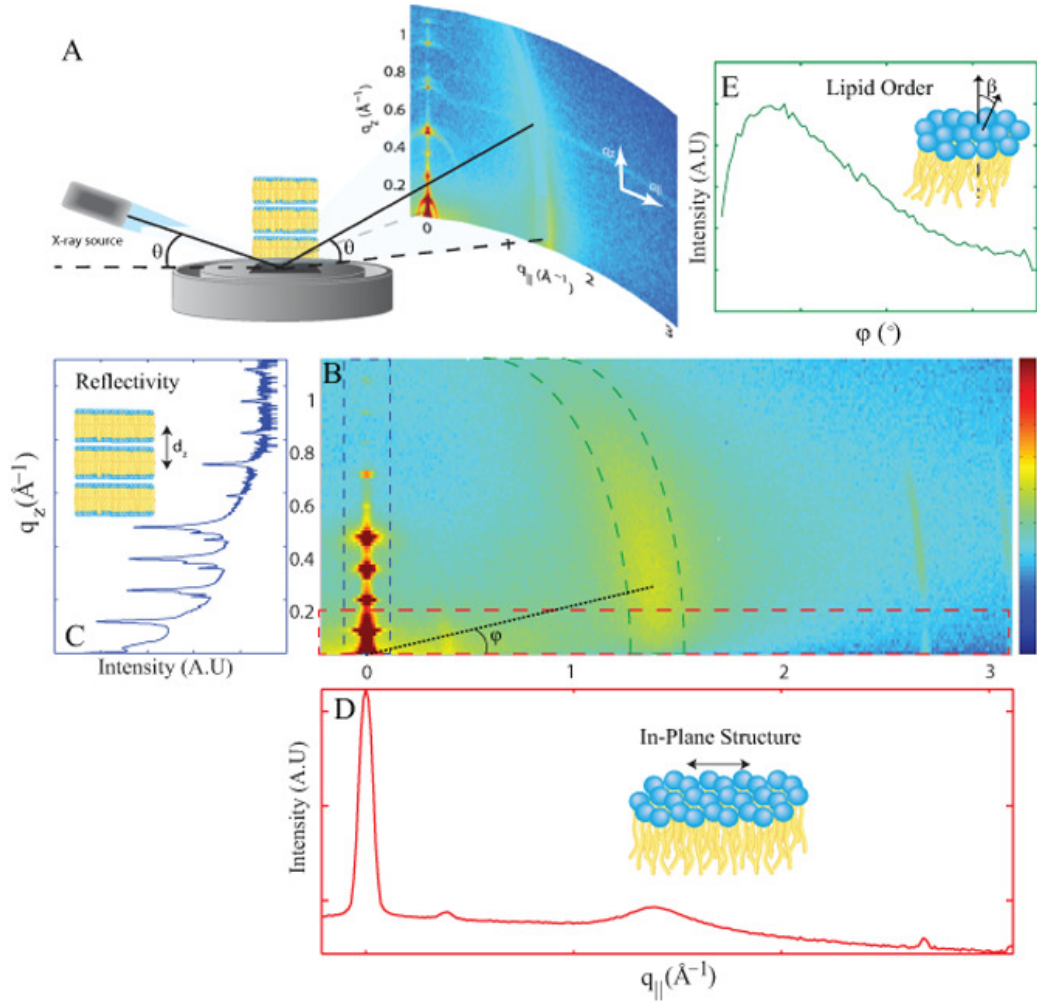


Figure 3.2: Extraction of one-dimensional scattering data from the two-dimensional X-ray diffraction map. A) Experimental X-ray diffraction set-up, showing how two-dimensional intensity maps were recorded for stacks of highly oriented lipid membranes. B) Two-dimensional intensity map obtained for POPC membranes. The one-dimensional scattering data shown in panels C-D were obtained by integrating the data in the 2D-map either over a small $q_{||}$ -range to obtain reflectivity curves as a function of q_z (C), over a small q_z -range ($0 \text{\AA}^{-1} \leq q_z \leq 0.3 \text{\AA}^{-1}$) to obtain in-plane scattering curves as a function of $q_{||}$ (D), or over a small q -range to obtain scattering curves as a function of ϕ (E). The regions of the 2D-map used to generate each kind of 1-D scattering curve are indicated by the corresponding coloured boxes.

3.2.1 Structure of Multi-Component Mitochondria-Like Membranes

We first compared the structure of the five-component mito-like membrane to that of a one-component POPC membrane. POPC was chosen as a control since PC is the most abundant phospholipid head group in the mito-like membrane, representing 48 mol % of the phospholipids in the mixture. Additionally, 16:0/18:1 (1-palmitoyl-2-oleoyl) is the most abundant chain composition in the naturally extracted PC used to form the mito-like membrane. Furthermore, POPC has often been used as a model system to study lipid membrane properties [62, 36, 50, 56, 39, 94, 124].

For the membranes studied here, the wide-angle scattering data always showed a single well developed chain-correlation peak at $q_{T,\parallel} \sim 1.4 \text{ \AA}^{-1}$, with a distinctive vertical rod-like shape typical of diffraction for 2-dimensional systems, as shown for POPC in Fig. 3.2D). The broad peak is indicative of a L_α fluid liquid crystalline phase (also referred to as liquid disordered phase, L_d) [84]. This is expected for the POPC membranes, even at this relatively low relative humidity, since the gel phase to fluid phase transition for POPC is $T = -3.7^\circ\text{C}$ [101, 36]. In addition, since the T_m for POPC, PE and DOPS, three lipids in the mito-like mix, are below the temperature of the experiment [10], and since the mito-like membrane also shows a broad chain correlation peak, we can conclude that the mito-like membrane is also in the fluid phase. This is to be expected even below physiologic temperature as the mito-like membrane is composed of unsaturated lipids that, in general, have higher degrees of fluidity as compared to saturated lipids of the same length.

For the POPC membrane studied here, we find that using equation 2.13 $A_c = 23.4 \text{\AA}^2$ at $83.6 \pm 0.3\%$ hydration (see Table 3.1 for a list of the structural parameters

Table 3.1: **Structural properties of the samples used in this study.** The average area per chain, A_c , was determined from the position of the chain correlation peak visible in the in-plane scattering data. The lamellar thickness, d_z , was determined from the position of the Bragg reflectivity peaks. The membrane thickness, d_{hh} , was equated to the headgroup peak-to-peak distance observed in the calculated electron density profiles. The head group thickness, w_h , head group electron density, H_h , CH₃ region thickness, w_c , and CH₃ region depth, H_c , were determined by fitting the electron density profiles as explained in the text and as illustrated in Fig. 3.4. The X-ray chain order parameter, $S_{\text{X-ray}}$, was determined from the vertical extension of the acyl chain peak, as explained in the text. Data was measured at $83.3 \pm 0.3\%$ relative humidity.

Sample	$A_c(\text{\AA}^2)$	$d_z(\text{\AA})$	$d_{hh}(\text{\AA})$	$w_h(\text{\AA})$	$H_h(\text{e}/\text{\AA}^3)$	$w_c(\text{\AA})$	$H_c(\text{e}/\text{\AA}^3)$	$S_{\text{X-ray}}$
POPC	23.40 ± 0.04	53.2 ± 0.8	39.1 ± 0.5	9.7	0.56	7.7	-0.09	0.36
Mitochondria-like	23.31 ± 0.06	50.26 ± 0.19	39.9 ± 0.5	8.5	0.59	6.7	-0.10	0.26
Mito-like (10% chol.)	24.1 ± 0.2	50.71 ± 0.17	40.3 ± 0.5	9.0	0.56	7.6	-0.11	0.39
Mito-like (20% chol.)	24.6 ± 0.1	51.4 ± 0.3	42.6 ± 0.5	9.9	0.52	10.2	-0.12	0.54
Mito-like (30% chol.)	24.8 ± 0.2	53.9 ± 0.7	43.1 ± 0.5	10.8	0.48	10.6	-0.10	0.48

measured for both membranes). This is as expected, falling between the value measured for a fully hydrated POPC membrane at $T = 30^\circ\text{C}$, $A_c = 34 \text{ \AA}^2$ [62], and that obtained for optimum packing of all-trans chains, $A_c \simeq 20 \text{ \AA}^2$ [99]. The measured area per chain for the mito-like membrane was determined to be $A_c = 23.3 \text{ \AA}^2$.

In a fluid phase lipids are not expected to have a favoured tilt angle with respect to the membrane normal, and therefore the chain-correlation peak profile should be centered at $\phi = 0$. However, as the intensity scattered parallel to the plane of the membrane ($\phi \lesssim 10^\circ$ values) is obstructed by the membrane itself, the peak maximum was not observed (see Fig. 3.2E) [83]. Therefore only the intensity obtained for $\phi \geq 13^\circ$ was considered when examining the profile of the chain-correlation peak. Assuming a Maier-Saupe orientational distribution function for the chains leads to an analytical expression for the peak scattering intensity as a function of polar angle, $I(\phi)$, which is dependent on the width of the chain orientation distribution Eq. (2.14) [83]. The width of this distribution can in turn be related to the chain orientational

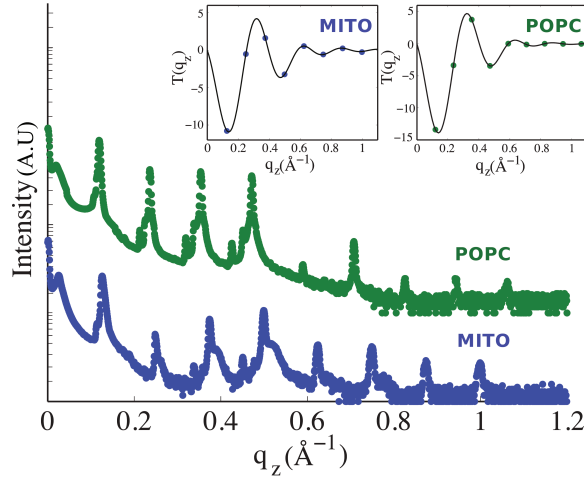


Figure 3.3: Reflectivity curves for mitochondria-like and POPC membranes. The X-ray reflectivity curves for the mitochondria-like membrane and for the POPC membrane (shifted upwards for clarity) show eight and nine well developed Bragg peaks, respectively. The insets show fits of the peaks amplitude with the continuous $T(q_z)$ function, plotted for the best combination of phases, ν_n . These are needed for the Fourier reconstruction.

order parameter, $S_{\text{X-ray}}$, as described in more detail in section 2.2.6. For the monounsaturated POPC membrane, we found that $S_{\text{X-ray}} = 0.36$. This value is close to that measured by the same method for fully hydrated membranes of the mono-unsaturated SOPC (1-stearoyl-2-oleoyl PC, or PC(18:0/18:1)) [93]. It falls between those measured for fully hydrated membranes of the saturated lipid DPPC (1,2-dipalmitoyl PC, or PC(16:0/16:0)) and of the di-monounsaturated lipid DOPC (1,2-dioleoyl PC, or PC(18:1/18:1)) [84], as predicted by coarse-grain simulations [123]. Strikingly, the order parameter measured for the mito-like membrane, which contains a significant fraction of di-monounsaturated and polyunsaturated chains (see Fig. 1.3), is significantly smaller: $S_{\text{X-ray}} = 0.26$.

The reflectivity curves obtained for the POPC and the mito-like membranes are compared in Fig. 3.3. Nine pronounced Bragg peaks were observed for the former,

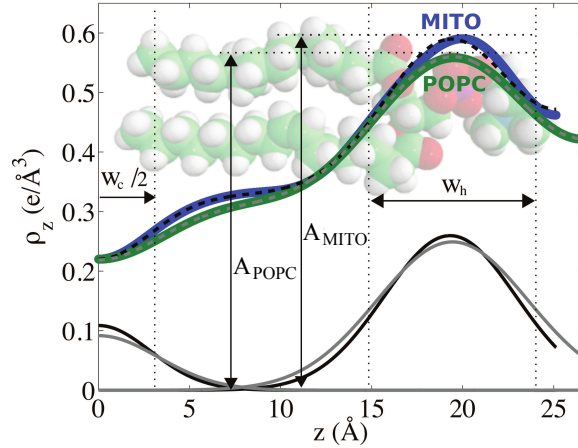


Figure 3.4: Calculated electron densities for the mitochondria-like and POPC membranes. The electron densities for the mitochondria-like and POPC membranes were determined from the data shown in Figure 3.3 and modelled with Gaussian peak profiles to represent different lipid molecular components. The head group region is fit with a single Gaussian peak, and the chain terminal region by a single Gaussian depression positioned at the centre of the membrane, both sitting atop a constant background. The individual components of the fit are plotted with a zero background in black and grey for the mitochondria-like and POPC membranes respectively. The dashed black and grey lines are the result of the total fit for the mitochondria-like and POPC membranes respectively. The FWHMs of the head group region, w_h , and chain terminal region, w_c , are indicated on the figure and their values are listed in table 3.2.

and eight for the latter, indicative in both cases of a well ordered lamellar structure. The lamellar spacing, determined from the position of the Bragg peaks, was found to be $d_z = 53.2 \text{ \AA}$ for the POPC membrane stack, comparable to the value reported for a similar relative humidity (86%) at room temperature, $d_z = 52.9 \text{ \AA}$ [40], but significantly below the value reported for POPC membranes at full hydration, $d_z = 64 \text{ \AA}$ [65]. The lamellar spacing of the mito-like membrane was slightly lower, $d_z = 50.3 \text{ \AA}$.

The average electron density profile, ρ_z , was calculated by Fourier transformation

of the integrated peak intensities, as outlined in Section 2.2.2. The profile was normalized following equations 2.11 and 2.11. The electron density profiles obtained for the POPC and the mito-like membranes are shown in Fig. 3.4. Both are consistent with the electron density profiles of lipid bilayers in the liquid-disordered state. The maxima found in the electron density profiles on either side of the membrane correspond to the electron rich phosphorous group found in the head group region. The membrane thickness, d_{hh} , defined here as the distance between electron density maxima can be extracted from this profile as explained in section 2.2.4. For the POPC membrane, we found that $d_{hh} = 39.1 \text{ \AA}$. This value is slightly larger than the thickness of a fully hydrated POPC membrane of $d_{hh} = 37 \text{ \AA}$ [62]. This is to be expected as more hydrated membranes allow for more disordered lipid chains which take up more lateral distance and thus result in a thinner membrane. The bilayer thickness of the mito-like membrane of $d_{hh} = 39.9 \text{ \AA}$, is slightly larger than that of the POPC membrane, probably due to the presence of lipids with chains longer than that of POPC (see Fig. 1.3).

The electron density profiles of both the POPC and the mito-like membranes were fit with Eq. (2.12), as shown in Figure 3.4, and the results of these fits are presented in Table 3.1. In a previous study, where several types of diffraction measurements were used to achieve high resolution, the head group region of one-component lipid bilayers was found to be best approximated by two Gaussians, one for the phosphatidylcholine region and one for the carbonyl and glycerol region [62]. However, in the case of the POPC membrane studied here, the use of two head group Gaussian peaks was found to lead to over fitting. In the case of the mito-like membrane, using two Gaussians for the head group region did give a better fit, probably because of the presence of

lipids with various head groups. For consistency, the fits shown in Fig. 3.4 and the results shown in Table 3.1 were those obtained using a single Gaussian peak.

3.2.2 Cholesterol Effects on Mitochondria-Like Membranes

The structure of mito-like membranes with increasing amounts of cholesterol was next studied to examine the effect of cholesterol on complex membranes.

The addition of cholesterol to fully hydrated lipid membrane usually leads to a significant decrease of the area per phospholipid molecule, and at the same time to a increase in membrane thickness. This effect, known as cholesterol's condensing effect, is due to the suppression of fluctuations and the ordering of the phospholipid hydrocarbon chains [25, 26].

The average area per chain A_c , was determined as described in section 2.2.6 from the position of the chain correlation peak observed in the in-plane diffraction data in Fig. 3.5. The shift of the position of the chain correlation peak to smaller $q_{||}$ -values with increasing cholesterol content reflects an increase of the average chain-chain distance and an increase of the corresponding average area per lipid chain, as shown in the inset of Fig. 3.5. At the same time, the broadening of the peak with cholesterol addition points to an increase in the average distribution of chain-chain distances, which can be expected since the surface area of cholesterol's "chain" (i.e. of the cholesterol molecule itself) is larger than that of a phospholipid chain. This makes the peak representative of a distribution of cholesterol chain-cholesterol chain, cholesterol chain-phospholipid chain and phospholipid chain-phospholipid chain distances. To correct for cholesterol increasing the average area of the unit cell, and to specifically examine the influence of cholesterol on the organization of the phospholipid chains,

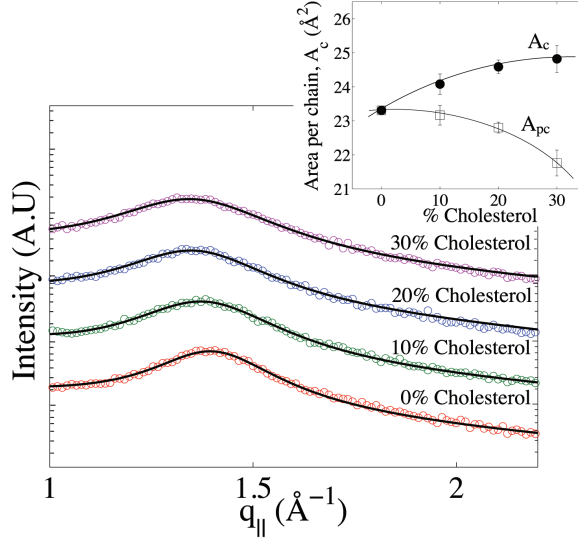


Figure 3.5: Area condensation effect of cholesterol in mitochondria-like membranes. Semi-log plot of chain correlation peaks for mitochondria-like membranes containing between 0 and 30 mol % cholesterol (see Table 2.1 for exact lipid composition). Each curve was fit with a Gaussian profile on a sloping background (black lines). Curves were shifted vertically for clarity. The inset shows the average area per total chain (i.e. including cholesterol chains), A_c , directly inferred from the position of the peak (closed symbols), compared to the average area per phospholipid chain, A_{pc} , as corrected for cholesterol volume using Eq .3.1 (open symbols). Solid lines are guides for the eyes.

the average area per chain, A_c , can be written as the average area per phospholipid chain, A_{pc} , and the area per cholesterol chain, A_{chol} :

$$A_c(x) = (1 - x)A_{pc}(x) + xA_{chol}, \quad (3.1)$$

where x is the cholesterol mol %, and where it is assumed that $A_{chol} = 39 \text{ \AA}^2$ is a constant [52]. Eq. (3.1) can then be used to calculate $A_{pc}(x)$. As can be seen in the inset in Figure 3.5, whereas A_c increases with cholesterol content, A_{pc} markedly decreases. Indicating that cholesterol's condensing effect is present in five-component mito-like membranes.

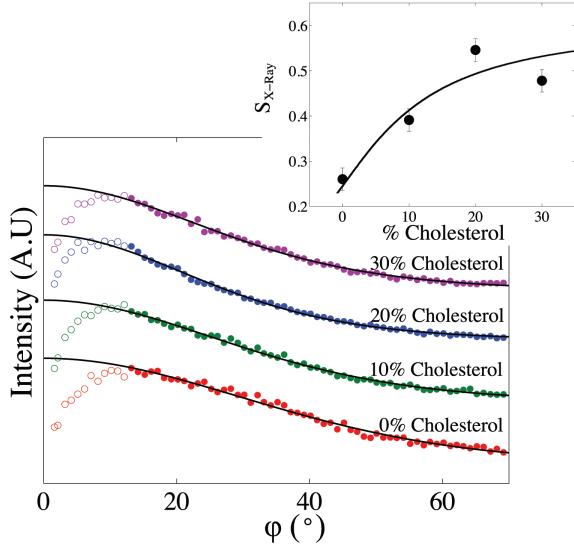


Figure 3.6: Cholesterol increases mitochondria-like membrane orientational order. Integrated intensities along the chain correlation peak are plotted as a function of the polar angle ϕ . Curves have been shifted upwards for clarity. Continuous lines represent fit of the filled symbol data with Eq. (2.14), while the open symbols were not included in the fit. The inset shows the X-ray chain orientational order parameter, $S_{X\text{-ray}}$, calculated from that fit.

Equation ?? was used in Ref. [31]. They assumed cholesterol's area was dependent on x , and found that cholesterol has negative partial specific area at low x . However, they measured the area per molecule by dividing the surface area of a simulation by the number of lipids in a bilayer leaflet, whereas we measured the area per chain from the acyl chain correlation peak. Thus, as we measured different quantities we chose to analyze our data differently, and assume that cholesterol's area was constant for our system.

The influence of cholesterol on lipid tail order was further assessed by extracting the order parameter, $S_{X\text{-ray}}$ from the wide-angle peak profiles shown in Fig. 3.6. As expected, $S_{X\text{-ray}}$ increases with cholesterol content (see inset in Fig. 3.6). This behaviour is comparable to that observed for single-component membranes, with a

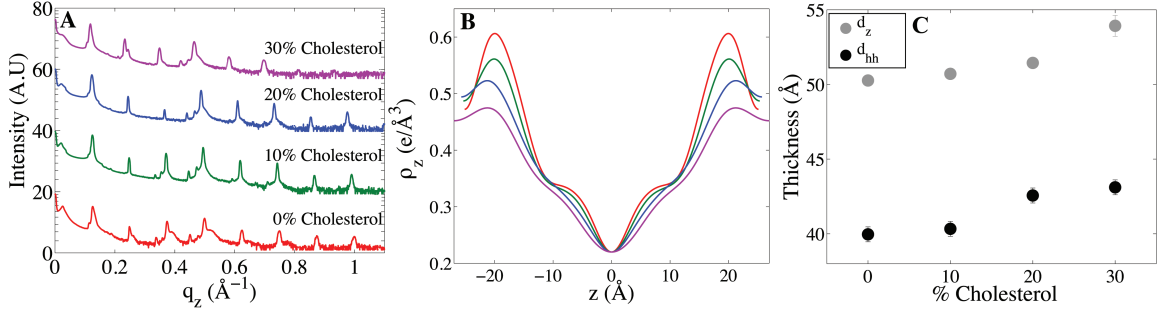


Figure 3.7: Cholesterol increases lamellar spacing and membrane thickness in mitochondria-like membranes A) Reflectivity curves for mitochondria-like membranes with 0, 10, 20 and 30 mol% cholesterol. The curves are shifted for clarity. Intensity is plotted on a logarithmic scale. B) Scaled electron density profiles of mitochondria-like membranes with the same cholesterol content as in A). C) Lamellar spacing, d_z , and peak-to-peak membrane thickness, d_{hh} , as a function of cholesterol content.

sharp increase of $S_{\text{X-ray}}$ for cholesterol contents between 0% and 20%, then a plateauing of the chain order around 30% cholesterol, at a value of $S_{\text{X-ray}}$ about double that obtained at 0% cholesterol [84, 93].

The reflectivity data for mito-like membranes containing cholesterol is shown in Figure 3.7A. All systems were found to form lamellar structures with pronounced and equally spaced Bragg reflections. Addition of cholesterol seems to have an effect on the topology of the membrane stacks, as the number of diffraction orders passes from eight to six when the amount of cholesterol reaches 30 mol %. The corresponding electron density profiles are shown in Figure 3.7B. These profiles were fitted with the Gaussian model described in Section 2.2.4. With the exception of the profile obtained in the absence of cholesterol, they were well fit by a single Gaussian peak to describe the head group region. The results of these fits are shown in Table 3.1. The electron density in the head group region decreased with increasing cholesterol content as

more electron rich lipid molecules are replaced by smaller cholesterol molecules. At the same time the head group peak shifts further from the center of the membrane, indicative of an increase in the bilayer thickness, d_{hh} , which coincides with the increase in lamellar spacing, d_z , as shown in Fig. 3.7C. This indicates that the thickening is occurring in the hydrophobic acyl chain region.

3.3 Neutron Reflectivity Results

We performed neutron reflectivity on POPC membranes and on mito-like membranes with 0, 10 and 20 % cholesterol. The goal of this experiment was twofold; the structure of a multi-component mito-like membrane was compared to that of a single component POPC membrane, and the location, orientation and effects of cholesterol were investigated in a mito-like membrane. In order to investigate the position of cholesterol in the mito-like membrane, we used deuterated and protonated cholesterol. Names for mito-like membrane samples containing deuterated cholesterol are distinguished from those with protonated cholesterol by using a ‘D’ following the cholesterol content as opposed to an ‘H’. So, a 10% protonated cholesterol sample is referred to as 10H, whereas a 10% deuterated cholesterol sample is referred to as 10D.

3.3.1 Determination of Sample Orientation Quality

As described in section 2.3.3, rocking curves are used to check the orientation quality of multilamellar samples. Figure 3.8 shows rocking curves for all six sample investigated. Minima in the curves are representative of neutron absorption and should occur when the substrate is parallel to either the incident or diffracted neutron beams.

The width of the narrow peak is indicative of the bilayers' orientation with respect to one another. The wider the peak, the larger the distribution of bilayer orientations. All samples had a narrow peak and thus were deemed to be well oriented.

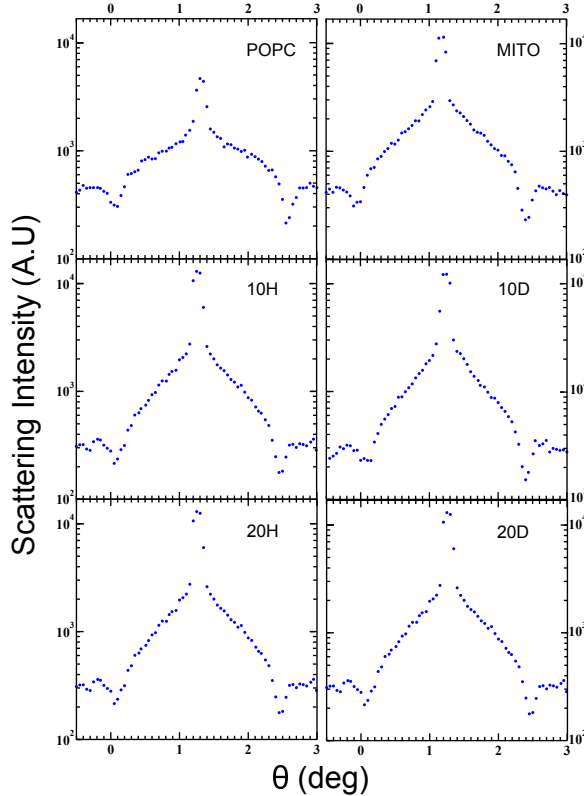


Figure 3.8: Neutron rocking curves. Semi-log plots of neutron rocking curves for the first diffraction peak for each sample taken at 100% D₂O. Minima in the curves occur where there is neutron absorption while rotating the sample in θ . Maximum absorption occurs when the substrate is parallel to either the incident or diffracted beams. The orientation of the bilayers in the sample can be determined from the width of the peak. The narrower the peak, the more oriented the bilayers. See section 2.3.3 for details. The six samples are POPC, mito-like (MITO), mito-like with 10% protonated cholesterol (10H), mito-like with 10% deuterated cholesterol (10D), mito-like with 20% protonated cholesterol (20H) and mito-like with 20% deuterated cholesterol membranes. Cholesterol samples are in mito-like membranes.

3.3.2 Neutron Reflectivity and Scattering Length Density Profiles

Neutron reflectivity as detailed in section 2.3.4 generated reflectivity curves for each of the six samples at four D₂O volume fractions. These curves are shown in figure 3.9, with the scattering intensity on the vertical axis and the probing angle, 2θ along the horizontal axis. Curves measured at 8, 40, 70 and 100% D₂O are all plotted and shifted vertically for clarity in that order. Each Bragg peak in each contrast solution was measured 4-5 times once the samples reached equilibrium and the curves in figure 3.9 are an average of those 4-5 measurements. They are also corrected for C_{flux} C_{abs} and C_{Lor} as discussed in section 2.3.2.

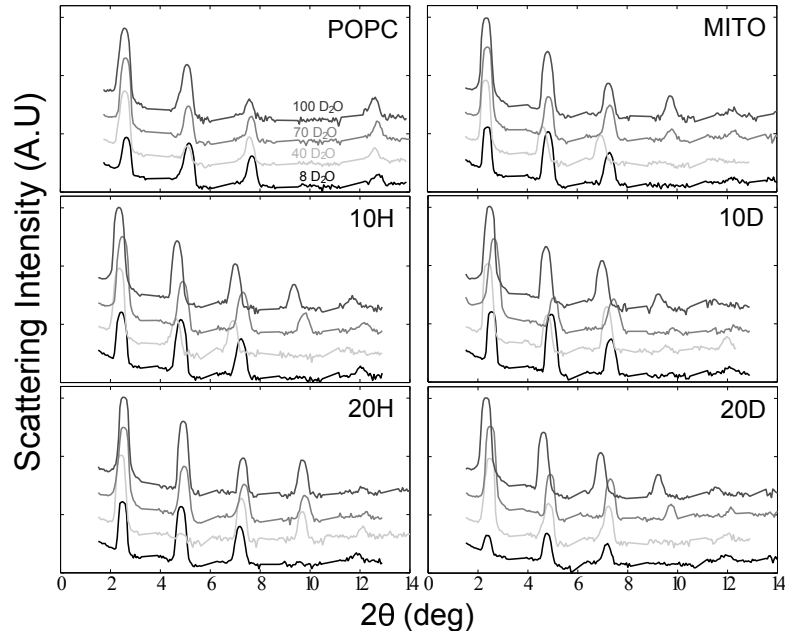


Figure 3.9: **Neutron reflectivity profiles.** Semi-log plots of neutron reflectivity curves for each sample in 8% D₂O, 40% D₂O, 70% D₂O and 100% D₂O in H₂O. Profiles are shifted vertically for clarity, in ascending order with the 8% D₂O profile at the bottom and the 100% D₂O profile at the top. Five diffraction orders were used for all profiles in all samples.

Five Bragg peaks were used for subsequent analysis for all six samples. Bragg peaks for different D₂O solution can have different magnitudes but should sit on top of one another as scattering from the bilayers is not affected by changes in the interbilayer water layer [59]. However in all of the samples, one or two of the four reflectivity curves had a shift in Bragg peak positions with respect to the others. As each of the samples was made from the same lipid solution, it is unlikely to be due to a difference in lipid content. Towards the end of the experiments, despite precautions such as hydrating samples under argon, a thin layer of yellow deposits was observed on the bottom edge of some of the substrates. Yellow deposits are indicative of oxidative damage to the unsaturated lipids. However, we do not believe the shift in Bragg positions is a result of oxidation, as oxidation would be time dependent and the shifted curves were not the ones performed last but rather the ones performed in the middle of the overall experiment. Finally, although incomplete equilibration of the samples (to 37°C) is a possible explanation, only curves that had stopped shifting were used for analysis, so we don't believe this to be the cause of the shifted Bragg positions. As oxidation, difference in lipid content, and incomplete temperature equilibration can be discarded as possible reasons for the shifted curves, we believe that incomplete hydration of the samples must have been the problem. The shift in the Bragg peak positions should not affect the scattering length density profiles as the lamellar spacing, d_z , is calculated from the weighted average of Bragg peak positions over all contrasts. Therefore the shifted curve would hold less weight in the average as compared to the other curves.

Form factors, F(n), were calculated using equation 2.19, where the integrated intensities, I(n), were found by integrating the area under each of the Bragg peaks in

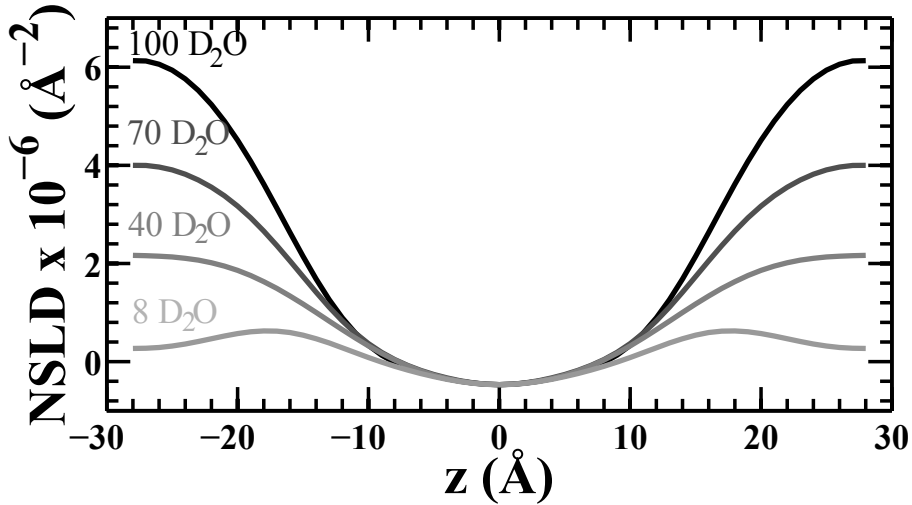


Figure 3.10: **NSLD profiles for a mito-like membrane at all contrasts.** Profiles were obtained for each of the four D₂O contrast solutions using equation 2.20 and scaled using equation 2.28.

figure 3.9. Phases, $\nu(n)$ were found following the method outlined in section 2.3.5. Values of F(n) are listed in table A.3. Form factors for each membrane were Fourier transformed using equation 2.20 to give scattering length density, SLD, profiles of the membranes. Figure 3.10 shows SLD profiles of the mito-like membrane at all four D₂O contrasts.

3.3.3 Structure of Single Component POPC and Multi-Component Mitochondria-like Membranes

In order to investigate the differences and similarities between a mito-like membrane and a POPC membrane, NSLD profiles at 8% D₂O were compared and are plotted in figure 3.11. 8% D₂O was chosen since at this D₂O concentration, scattering from the solvent is effectively zero and therefore the scattering comes only from the membrane, as explained in section 2.3.4 [30].

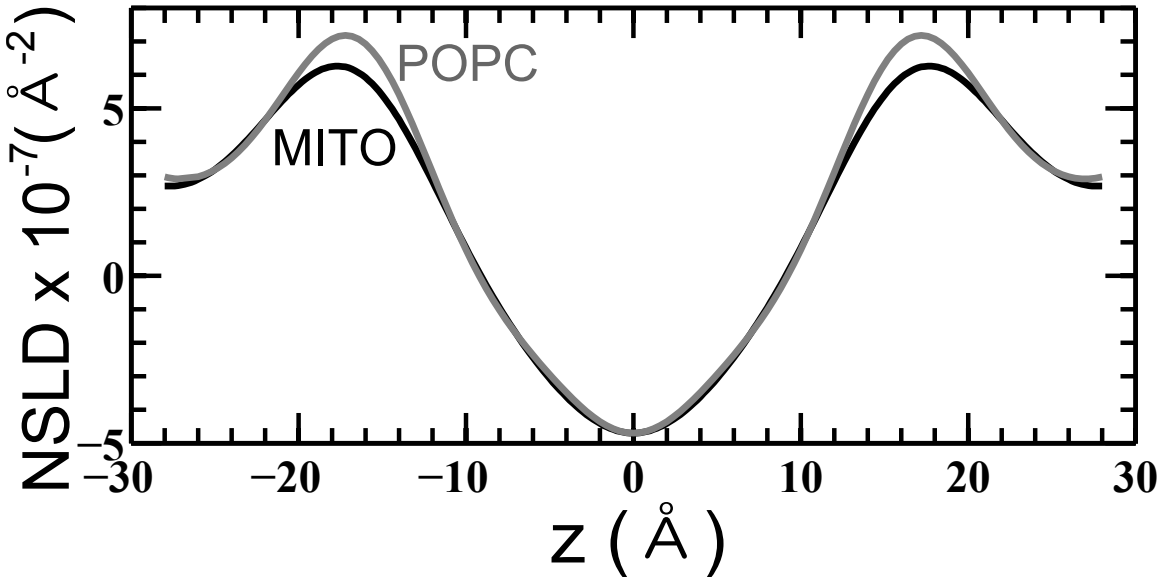


Figure 3.11: **NSLD profiles for mito-like (MITO) and POPC membranes.** Profiles are of membranes hydrated with 8% D₂O. Notable differences include thickness, carbonyl peak width and acyl chain shape.

At the same hydration level and 8% D₂O, the two membranes share the common structure of two peaks centered around the carbonyl groups in the headgroup of the lipids, and a dip at the center of the membrane, $z=0$. Slight differences are apparent in the thickness of the membranes and in the structure of the acyl chain region. The latter difference can be seen by the slight “kink” visible between the center of the POPC bilayer and the carbonyl groups. This kink is associated with the location of carbon double bonds in unsaturated phospholipids such as POPC [126]. The mito-like membrane on the other hand does not display this kink, and instead has a ‘U’ like shape from the carbonyl peak to the bilayer center. Although the mito-like membrane is composed of unsaturated lipids, we believe that the combination of lipids with different tail lengths and degrees of unsaturation leads to a broadening of the distribution for the “kink” location until it is a smooth ‘U’ shape. This ‘U’

Table 3.2: Structural parameters of POPC and mito-like membranes. d_z is the unit cell thickness and comes directly from the distance between Bragg peaks using equation 2.5. d_b and d_w are the bilayer and water thicknesses, d_b comes from the peak to peak distance of membranes in figures 3.11 and 3.15 and $d_w = d_z - d_b$.

Sample	d_z (Å)	d_b (Å)	d_w (Å)
POPC	54.03	34.4	19.63
Mito-like	55.42	35.6	19.82

shape is indicative of an increase in membrane fluidity and flexibility [45], likely a result of the distribution of tail lengths and degrees of unsaturation in the mito-like membrane. Physical quantities measured from the SLD profiles are listed in table 3.2, and represented schematically in figure 3.12.

The POPC lamellar thickness, d_z , is comparable to that found for POPC membranes at 86% RH [39], and 10 Å shorter than that measured for fully hydrated POPC [62]. On the other hand, the membrane thickness, d_b , defined as the peak to peak distance in the NSLDs, for POPC was only slightly smaller than that of fully hydrated POPC membranes, 36.8 Å [62]. Thus the 10 Å difference in d_z must come primarily from water molecules and therefore the hydration.

Both d_z and d_b differ slightly between the mito-like and POPC membranes. They are both larger for the mito-like membrane by 1.4 Å and 1.2 Å respectively. As the mito-like membrane is composed of lipids with various headgroups, some of which are larger than PC (see figure 1.3 for lipid chemical structures), and as the peak of the NSLD comes primarily from the carbonyl group which connects the headgroups to the acyl chains, the differences of 1.4 Å and 1.2 Å most likely comes from the difference in headgroups other than PC and in acyl chain lengths between the mito-like membrane and the POPC.

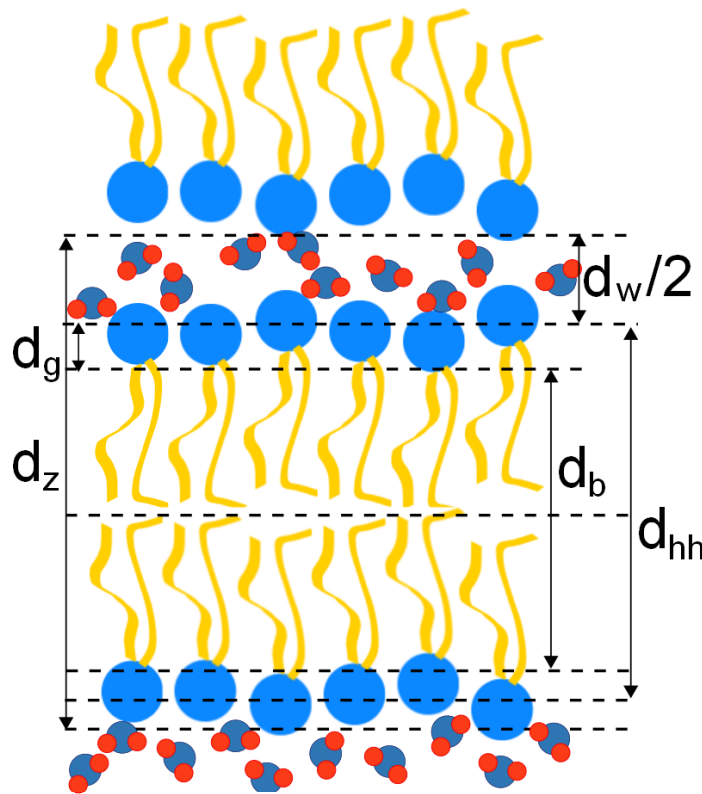


Figure 3.12: **Membrane bilayer thicknesses.** Lamellar thickness, d_z , membrane thickness found by neutron scattering, d_b , membrane thickness found by x-ray scattering, d_{hh} , the glycerol region thickness, d_g and half the water layer thickness, d_w , are represented schematically.

The structure of these two membranes thus only differs slightly in acyl region flexibility and overall length, which is to be expected as POPC is the main component of the mito-like membrane and the differences can be attributed to the differences in mito-like lipids headgroups, tail lengths, and degrees of unsaturation. The change in the mito-like structure as a function of cholesterol will be discussed in the following section.

Table 3.3: **Structural parameters of bilayers.** d_z is the unit cell thickness and comes directly from the distance between Bragg peaks using equation 2.5. d_b and d_w are the bilayer and water thicknesses, d_b comes from the peak to peak distance of membranes in figures 3.11 and 3.15 and $d_w = d_z - d_b$.

Sample	d_z (Å)	d_b (Å)	d_w (Å)
POPC	54.03	34.4	19.63
Mito-like	55.42	35.6	19.82
Mito-like (10% H chol)	56.70	36.8	19.9
Mito-like (10% D chol)	57.04	35.6	21.44
Mito-like (20% H chol)	57.98	37.2	20.78
Mito-like (20% D chol)	56.93	35.2	21.73

3.3.4 Cholesterol Effects on Mitochondria-Like Membranes: Membrane Thickness

In order to investigate the thickening effect of cholesterol on a mito-like membrane, the d_z and d_b of mito-like membranes containing cholesterol were compared. Values for both of these thickness are listed in table 3.3. Cholesterol increases the d_z of the membranes by 2.6 Å from 0 to 20% cholesterol content. Figure 3.13 shows NSLD profiles of half the membrane of mito-like membranes with 0-20% cholesterol content. d_b increases as a function of cholesterol by 1.6 Å which is consistent with what was observed in molecular dynamic simulations for one component DPPC membranes from 0-11% cholesterol, showing an increase in d_b of 1.2 Å [112] and from neutron experiments with DMPC one component membranes from 0-30% cholesterol that found an increase in d_b of 3.9 Å [28]. Moreover the value of d_b measured for mito-like membranes with 10% cholesterol agrees well with the value for POPC membranes with 10% cholesterol found using neutron diffraction, 36.5 Å [45].

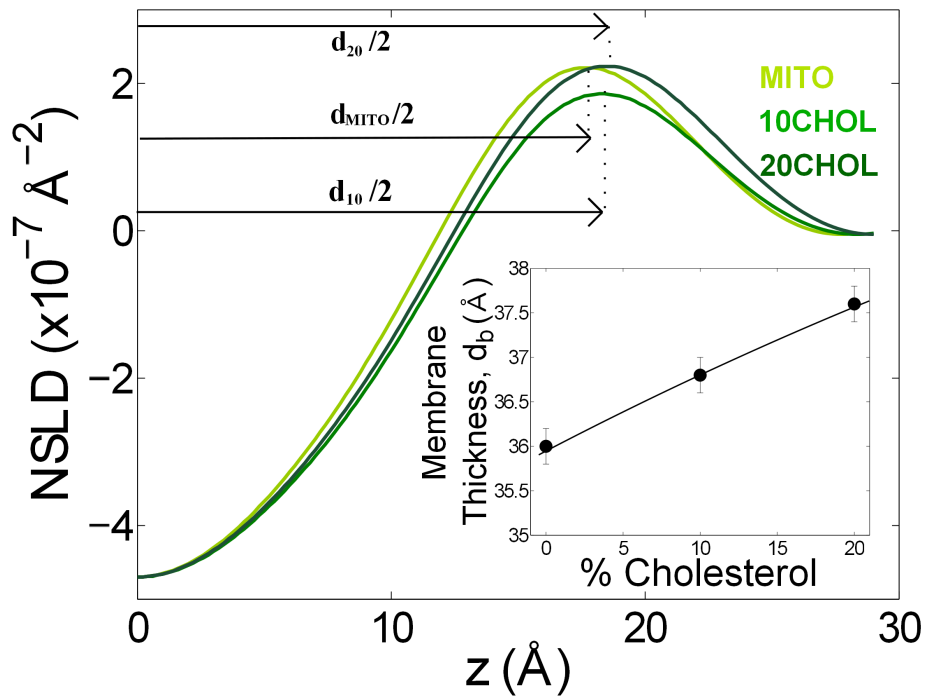


Figure 3.13: **NSLD profiles for mito-like (MITO), 10 and 20% cholesterol containing membranes.** Inset shows the change in membrane thickness defined as the distance between the two carbonyl peaks, as a function of cholesterol content. Note that cholesterol has a thickening effect on the multicomponent mito-like membranes.

Another measure of the membrane thickness is the depth of water penetration. Water penetration is defined as the position, z_w of a logistic function fit to the water probability profile from the center of the membrane. The water profile can be determined since, as has been mentioned before, the scattering from bilayers is independent of the D_2O content in the water layer and the only difference in scattering amongst the four contrast solutions originates from the change in the water layer. Thus the water profile can be obtained from the average of the differences between NSLDs of the samples at the four contrast solutions.

Figure 3.14 shows the water penetration for mito-like membranes with 0-20%

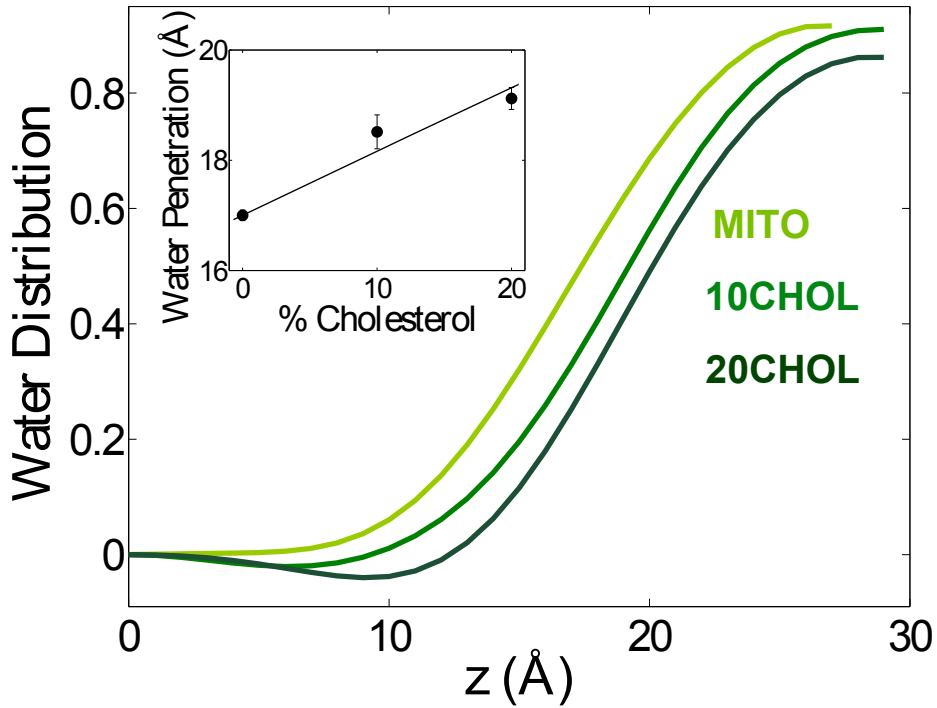


Figure 3.14: **Water probability profiles for mito-like 10 and 20% cholesterol containing membranes.** Curves are obtained from the average of the differences between NSLDs of the samples at the four contrast solutions. The inset shows the change in water penetration, defined from the center of the membrane, as a function of cholesterol content.

cholesterol content. The values of z_w are listed in table 3.4. The decrease in water penetration (with respect to the outside of the membrane) is of the same magnitude as the increase in membrane thickness, thus it is believed to be a result of the same effect.

From this we conclude that cholesterol increases the overall membrane thickness by straightening membrane hydrocarbon chains thus increasing the thickness of the membrane hydrophobic region and the membrane order. As volume must be conserved, the thickening effect must be accompanied by an area condensation effect, characteristic of cholesterol in one and two component model membranes[112, 28].

3.3.5 Cholesterol Effects on Mitochondria-Like Membranes: Location and Orientation of Cholesterol

Cholesterol's orientation and location in the mito-like membrane were determined by finding the deuterium label profile, $\rho_c(z)$. The NSLD of bilayers containing protonated cholesterol are assumed to remain unchanged upon the incorporation of labeled deuterated cholesterol. Thus the difference in NSLDs between samples with protonated and deuterated cholesterol is equal to $\rho_c(z)$.

$$\rho_c(z) = \rho^D(z) - \rho^H(z) \quad (3.2)$$

where $\rho^D(z)$ and $\rho^H(z)$ are the NSLD profiles of the samples containing deuterated and protonated cholesterol respectively, and are plotted in figure 3.15.

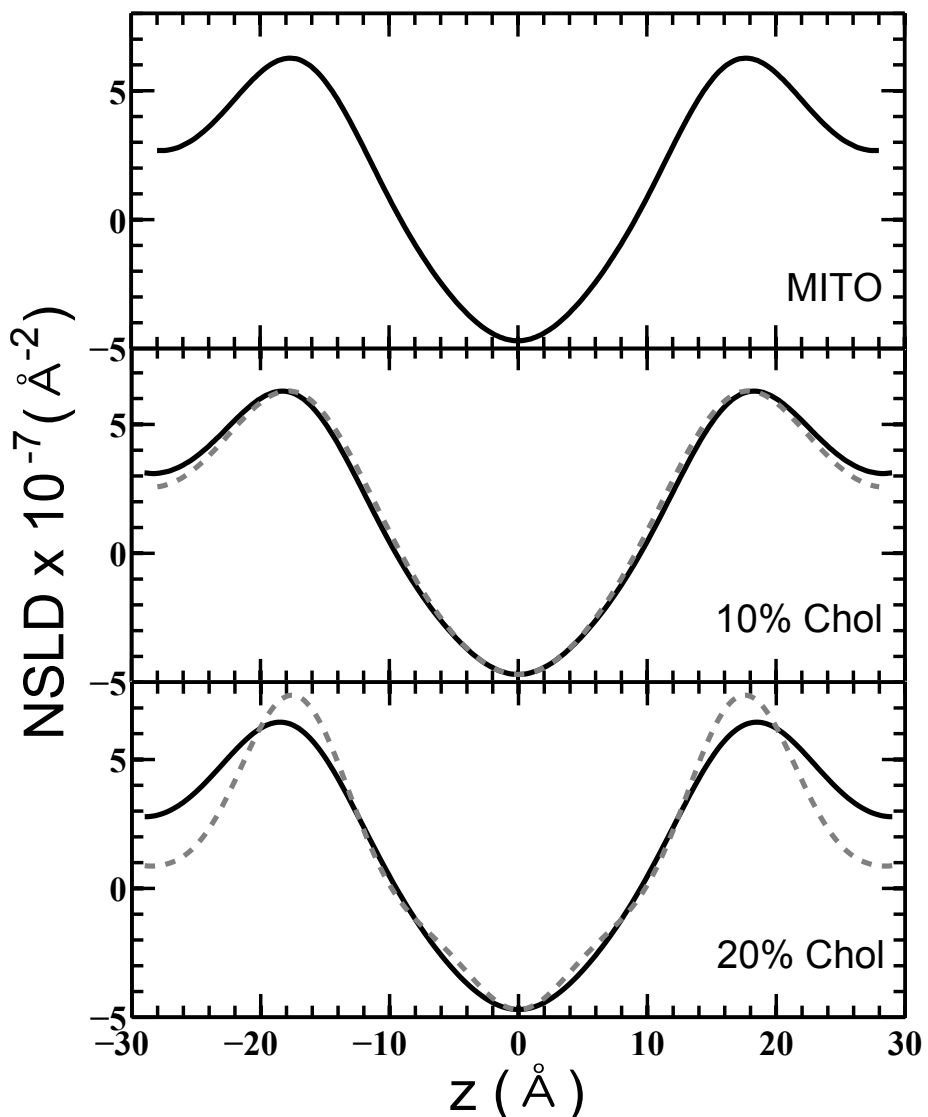


Figure 3.15: NSLD profiles for mito-like (MITO), 10 and 20% cholesterol containing membranes. Profiles are obtained using equation 2.20 and scaled using equation 2.28. Membranes containing protonated cholesterol are shown as black curves, while those labeled with deuterated cholesterol are shown as dashed gray curves. Note that as cholesterol content increases, a “kink” in the acyl chain region begins to appear, more pronounced in the deuterated membrane, signaling greater lipid order.

Label profiles for mito-like membranes with 0-20% cholesterol are plotted in figure 3.16. The position of the label profile maximum, z_c is defined at the location of the label. The difference profiles show the location of the center of mass of the deuterium label on the ring structure of cholesterol. The location of the label for both 10 and 20 mol% cholesterol are listed in table 3.4. The location at $\simeq 17 \text{ \AA}$ of the center of mass of the deuterium label in the 20 mol% cholesterol sample agrees with the location of $\simeq 16 \text{ \AA}$ found previously for 10 mol% cholesterol samples of POPC, DOPC and 18:0-20:4 PC [45] and a 30 mol% cholesterol sample of DMPC [69]. As the position of the lipid's carbonyl group for the 20 mol% cholesterol sample is approximately $z_b=19 \text{ \AA}$ (2 \AA outside the location of the deuterium label) and as the hydroxyl group of cholesterol is 1.9 \AA outside the center of mass of the label, this puts the polar hydroxyl group of cholesterol in good position to hydrogen bond with the lipid's ester oxygens as has been shown previously for single component PC membranes [45, 69].

For the 10 mol% cholesterol sample on the other hand, $z_c=14 \text{ \AA}$ and $z_b=18 \text{ \AA}$. The difference between the center of mass of the deuterium label and the position of the lipid's carbonyl group is 4 \AA , thus the difference between the position of the

Table 3.4: Location of the cholesterol label and water penetration depth. Uncertainty in the position measurements comes from Gordeliy and Chernov's (1997) theoretical prediction that one can achieve accuracy of 1 \AA for molecular label positions in neutron diffraction experiments with 4 diffraction orders. z_b are for the samples containing protonated cholesterol.

Sample	z_c (\AA)	z_w (\AA)	z_b (\AA)
POPC	—	17 ± 1	17 ± 1
Mito-like	—	17 ± 1	18 ± 1
Mito-like (10% chol)	14 ± 1	19 ± 1	18 ± 1
Mito-like (20% chol)	17 ± 1	20 ± 1	19 ± 1

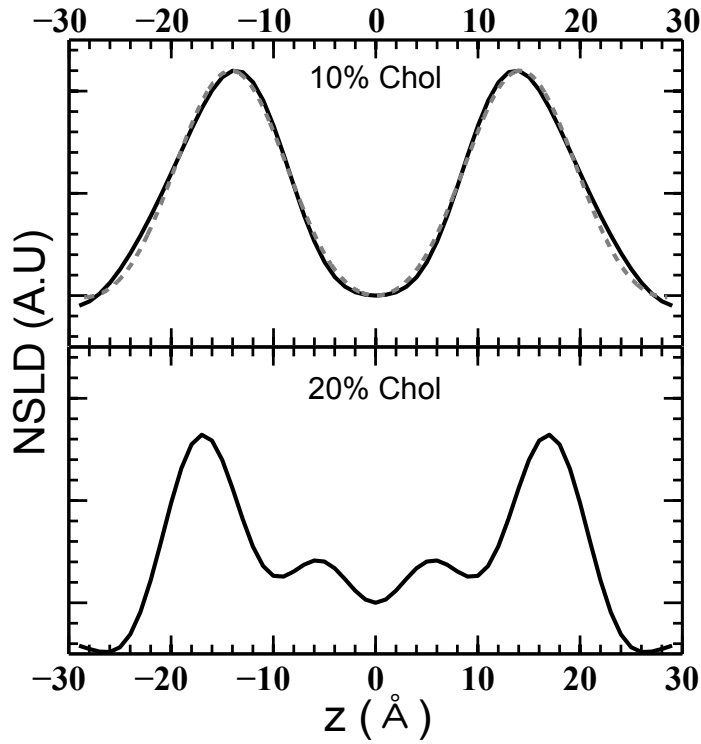


Figure 3.16: NSLD profiles of the deuterium label for 10 and 20% cholesterol containing membranes. The black curves represent label profiles obtained using equation 3.2. The gray dashed curve represents a Gaussian fit performed in reciprocal space for the 10% sample. The position of the label moves outwards from the center of the membrane with an increase in cholesterol content. Note that the width of the 10% cholesterol containing membrane is wider than for the 20% case. As the width of the label represents the time-average motion [45], the 10% sample has greater fluidity.

lipid's carbonyl group and cholesterol's hydroxyl group is 2 Å. However, the carbonyl, water and cholesterol label profiles still overlap (see figure 3.17) indicating that there is potential for hydrogen bonding [113]. Finally, the width of the label profile is indicative of the time-average motion of the label, which is larger for the 10 mol% cholesterol sample than for the 20 mol% cholesterol sample.

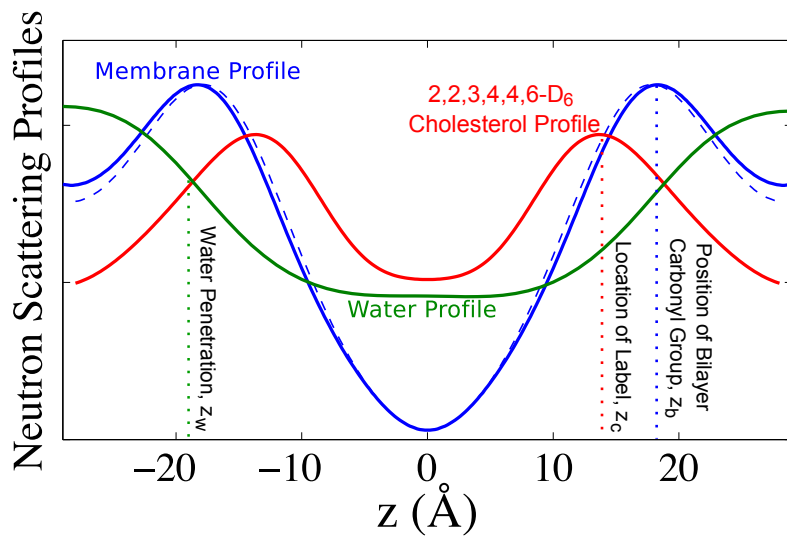


Figure 3.17: **Structure of a 10% cholesterol containing membrane.** The blue solid curve represents the NSLD in arbitrary units of the 10% protonated cholesterol sample, while the blue dashed curve is for the 10% deuterated cholesterol sample. The green curve represents the water probability distribution, and the red curve is the profile of the center of mass of the cholesterol label. Note that the label is approximately 4.8 \AA inwards from the carbonyl peak (the maxima of the blue curves), and the water penetration profile is centered at the carbonyl peak. Nevertheless, the label distribution overlaps with the headgroup distribution, thus making it possible for cholesterol to hydrogen bond with the ester oxygens, see text for details.

Chapter 4

Discussion

4.0.6 How Different is the Multicomponent Mitochondria-Like Membrane From a Single Component POPC Membrane?

Although our x-ray and neutron experiments were carried out in different conditions (83.6% RH, T=28°C for the x-ray experiments and 96% RH, T= 37°C for the neutron experiment), in both cases the membrane was in the liquid crystalline L_α phase. Despite the membrane fluidity in both cases it was possible to observe structural features (eight Bragg peaks for the x-ray reflectivity, and five Bragg peaks for the neutron reflectivity).

The structure of the mito-like membrane differed in a number of ways from that of the POPC membrane in both the x-ray and neutron experiments (structural parameters can be compared in Table 4.1). The mito-like membrane was slightly ($\simeq 1\text{\AA}$) thicker than the POPC membrane (found for both d_{hh} and d_b), not surprisingly since it contained some lipids with longer chains (see Fig. 1.3) [63]. It should be noted

Table 4.1: Some structural parameters of the membranes in this study found by neutron and x-ray scattering. This table summarizes some of the structural parameters found using x-ray and neutron scattering for POPC, mito-like and mito-like with cholesterol membranes.

Sample	83 % RH (x-ray)				97% RH (neutron)			
	A_{pc} (Å ²)	d_{hh} (Å)	d_z (Å)	S_{X-ray}	d_z (Å)	d_b (Å)	z_c (Å)	z_b (Å)
POPC	23.40	39.1	53.2	0.36	54.03	34.4	—	17
Mito-like	23.31	39.9	50.3	0.26	55.42	35.6	—	17
Mito-like (10% H chol)	23.2	40.3	50.7	0.39	56.70	36.8	—	—
Mito-like (10% D chol)	—	—	—	—	57.04	35.6	13.6	19
Mito-like (20% H chol)	22.8	42.6	51.4	0.54	57.98	37.2	—	—
Mito-like (20% D chol)	—	—	—	—	56.93	35.2	16.5	18.6

however that d_{hh} and d_b do not measure the same thing, the former measures the phosphate to phosphate group distance, while the later measures the carbonyl to carbonyl group distance of the phospholipids. At the same time, the lamellar spacing found using x-ray diffraction was significantly ($\simeq 3$ Å) thinner for the mito-like membrane. This means that the water layer found between mito-like membranes was $\simeq 4$ Å thinner than that found between POPC membranes. This corresponds to a loss of $\simeq 0.5$ water molecules per lipid chain (assuming a water molecule has a specific volume of 30 Å³), or $\simeq 1$ water molecule per phospholipid (except CL which occupies a larger surface area). Since at 83.6% relative humidity it was shown that each POPC molecule had $\simeq 7$ water molecules associated with it [39], we conclude that phospholipids in the mitochondria-like membrane, have, at the same relative humidity, only $\simeq 6$ water molecules associated with each of them, or in other words, that there are $\simeq 3$ water molecules on average for each lipid chain in the mito-like membrane. The lamellar spacing, by contrast, for the mito-like membrane found in the neutron experiment was $\simeq 1.3$ Å larger than the POPC lamellar spacing.

As the membranes were at a higher hydration in the neutron experiment it was

expected that d_z would increase. This was found to be true as d_z increased between the x-ray and neutron experiments for both membranes. As the increase was significantly greater for the mito-like membrane (5.8 Å as compared to 0.8 Å for the POPC membrane) we believe the mito-like membrane was able to achieve a slightly thicker water layer.

The fact that only a thin water layer is present in the case of the mito-like membrane at lower hydration could be due to favorable interactions between the negatively charged lipids in the complex membrane and positive ions in solution. While, at higher hydration (96%RH), with a greater number of ions in solution, this interaction becomes weaker and the water layer between adjacent bilayers is able to be thicker. A thicker water layer was only found at higher hydration for the mito-like membrane, not for the neutral POPC.

Making assumptions about the number of water molecules present per chain allowed normalization of the electron density profile of both the POPC and the mito-like membranes without having to make the assumption that the electron density between two membranes was equal to the electron density of water, $\rho = 0.33 \text{ \AA}^3$. Although this last assumption is common, it is likely not appropriate to the study of membranes at a low level of hydration, such as ours. Indeed, the electron density between the membrane is higher than that of water (see figure 3.4), due to the close proximity of neighbouring electron-rich lipid head groups. A sign that the method adopted here is valid, can be seen in the similarity between the electron density of both tail regions. This is as one would expect, since the tail regions of other membranes, DMPC and DLPC have been shown to have a constant electron density [62].

The most notable difference between the POPC and mito-like membranes was

the higher degree of chain disorder in the mito-like membrane found using x-ray diffraction. Chain order was assessed in our study using wide-angle x-ray scattering to measure the chain order parameter $S_{\text{X-ray}}$. It has been shown that $S_{\text{X-ray}}$ differs from the usual chain order parameter measured by NMR only by a multiplication factor [84]. It has also been pointed out that for membranes containing unsaturated chains, as was the case for the membranes we studied, $S_{\text{X-ray}}$ gives a more consistent evaluation of the chain order [93]. The chain order parameter of the mito-like membrane was more than 25% lower than that of the simple POPC membrane, and instead equal to that measured for DOPC membranes, formed with a lipid containing two mono-unsaturated chains, at close to full hydration [93].

Since the fraction of polyunsaturated chains present in the mito-like membrane ($\simeq 4\%$) is not high enough to explain such a low order parameter [84, 93], it is likely that this is instead a feature of multicomponent membranes containing lipids with different tail compositions. In other words, a membrane made of lipids with a number of different chains may have a lower order parameter than membranes composed uniquely of any of its components.

This happens while, interestingly, the area per chain for the mitochondria-like membrane is very low, almost the same as for the POPC membrane, and, close to that obtained for optimum packing of acyl chains, $A_c \simeq 20 \text{ \AA}^2$ [99]. Thus the membrane is disordered but the packing, at least close to the headgroup region, is close to ideal. Additionally, the structural features of the mito-like membrane (i.e. the width of the CH_3 and headgroup regions) seemed to be, if anything, slightly sharper than that of the POPC membrane. In addition, whereas the POPC headgroup region in the electron density profile was perfectly fit by a single Gaussian peak, as expected for

simple membranes in the fluid state [4], that of the mito-like membrane was not. Thus chain orientation disorder does not translate in a significant smearing out of the electron density profile across the membrane, and did not prevent the resolution of fine features, in this case probably due to the heterogeneity in headgroup composition.

4.0.7 Effect of Cholesterol on The Complex Mitochondria-Like Membrane

High cholesterol concentration in the plasma membrane of mammalian cells is known to decrease membrane fluidity and increase membrane rigidity and thickness, thereby helping to provide a stronger cellular enclosure. In one-component membranes, the effect of cholesterol has been quantitatively studied by many different methods (experimental and simulations, see e.g. Ref [86] for a review), in particular for POPC membranes [50]. Cholesterol has been shown to thicken the membrane and simultaneously (since the volume of the hydrophobic region of the membrane is conserved [92]) to reduce the surface area allotted to each phospholipid (a process known as the condensing effect [79]). This occurs as the result of a decrease in chain disorder, thought to be due to cholesterol's interaction with the acyl tails resulting in a straightening out of the lipid chains [26]. The condensing effect is stronger for membranes containing saturated lipids, as cholesterol has been found to change the thickness of membranes to a greater extent for saturated membranes as compared to monounsaturated membranes [93, 51]. Cholesterol is also known for enabling the formation of a special phase, the liquid ordered phase, which possess both a high fluidity and a high order parameter [53]. Finally, cholesterol is known to sometimes segregate and form highly ordered domains (the equivalent of lipid rafts in cells) [86, 7].

Overall, we find that the mito-like membrane behaves much like a single-component membrane upon addition of cholesterol. The orientational order parameter of the hydrocarbon chains, quickly doubles upon increase of cholesterol content (Fig. 3.6), reaching what seems to be a maximum around $S_{X\text{-ray}} \approx 0.5$. This plateauing was also observed for single-component membranes, although the maximum value observed for the complex membrane ($S_{X\text{-ray}} \approx 0.5$) is lower than what was observed at high cholesterol content even for di-monounsaturated lipids (e.g. DOPC) and higher hydration levels [93]. This again suggests that five component membranes cannot achieve as high a degree of order as any single-component membranes that could be formed with the individual components of the five component membrane. In other words, the capacity of cholesterol to order the five component membrane is limited.

In addition to the position of cholesterol's label in a mito-like membrane, the width of its distribution also gives information about the overall structure of the membrane. The width of the label distribution describes the time average motion of the label, and was found to decrease as a function of cholesterol content. This indicates that the membrane becomes more rigid with the addition of cholesterol, supporting the idea that cholesterol increases the mito-like membranes' order which is supported by the increase found in $S_{X\text{-ray}}$ with the addition of cholesterol.

Accordingly with the increase in chain ordering and therefore chain straightening upon addition of cholesterol, the thickness of the membrane increased by 8 % and 5 % in the x-ray and neutron experiments respectively. Furthermore the surface area per phospholipid chain found using x-ray diffraction accordingly decreased by 6 % after addition of 30% cholesterol. This condensing effect seems to be slightly weaker than that observed for one component membranes (see e.g. Refs [51, 26], where the area

Table 4.2: **Average surface area per phospholipid chain.** Average area per phospholipid chain, A_{pc} , as calculated directly from the position of the chain correlation peak (Eq. (2.13)) or as inferred from the value of the membrane thickness (Eq. (4.1)).

Sample	$A_{pc} \text{ \AA}^2$	$A_{pc*} \text{ \AA}^2$
POPC	23.4	18.4
Mitochondria-like	23.3	17.8
Mito-like (10% chol.)	23.2	17.6
Mito-like (20% chol.)	22.8	16.4
Mito-like (30% chol.)	21.8	16.1

condensation is shown to be around 10 – 20 % for 30 % cholesterol, although their experiments and simulations were performed at a high relative humidity). However, the membrane thickness, d_b , found from neutron diffraction is in agreement with increases seen for fully hydrated diC22:1PC, a di-monounsaturated lipid [66]. So although x-ray data suggests area condensation to be weaker for the five component membrane as compared to single component membranes, the neutron data suggests that at least the thickening effect is in agreement with what would be expected from single component membranes. However, these experiments were performed at different hydrations, so there is a possibility that at a higher hydration, the complex membrane can achieve greater condensation as a result of cholesterol.

The values of A_{pc} we obtained directly from the position of the correlation peak are consistently larger than those that can be inferred from the membrane thickness by assuming the chain region is incompressible, as done for example in Ref. [51]:

$$A_{pc} = \frac{V_c}{d_{hh} - 2d_g}, \quad (4.1)$$

where $V_c = 495 \text{ \AA}^3$ is the average volume of a phospholipid hydrocarbon chain [88],

and $d_g \simeq 5 \text{ \AA}$ is the length of the glycerol region. Both sets of values are shown in table 4.2 for comparison. We acknowledged that the determination of the area per phospholipid in fluid membranes is not a completely understood area. The discrepancy in the values listed in table 4.2 could be due to assumption made to come up with the value of V_c used.

Cholesterol has a clear effect on the acyl chains of the phospholipids present in the membrane, but it also affects the lipid headgroup region. As the membrane thickness increases, so does the lamellar spacing to the exact same extent (see Fig. 3.7), which implies the thickness and therefore presumably the structure of the water layer around the phospholipid head groups does not significantly change. On the other hand, we observe that the electron density in the headgroup region is strongly decreased upon cholesterol addition (Fig. 3.7, by 20 %). This can be attributed to the fact that the average area per chain, A_c , increases (Fig. 3.5, by 6 %) and the headgroup region becomes wider along z (see Table 3.1, by 20 %). We believe the increase in A_c is due to the fact that the cross-section of the cholesterol chain is larger than that of a phospholipid chain. Thus the average measured A_c with potential contributions from distances between cholesterol and cholesterol, cholesterol and phospholipid chain, and phospholipid chain and phospholipid chain, becomes larger than it would be with contributions from only phospholipid chain to phospholipid chain distances. In addition, cholesterol's polar region is small (just a hydroxyl group) which could contribute to the decrease in headgroup electron density. The overall decrease in headgroup electron density has implications for the distribution of ions in the vicinity of the membrane surface, and the type of electric potential profile encountered by molecules approaching the membrane, such as proteins.

Overall we found that cholesterol affected our mito-like membrane in a similar fashion to one and two component membranes, by increasing the membrane thickness and decreasing the area per phospholipid chain. Additionally, the ordering brought about by cholesterol was found by x-rays to be less complete than ordering in homogeneous one component membranes.

4.1 Orientation of Cholesterol in a Mitochondria-like Membrane

Cholesterol has been observed to adopt a non-canonical orientation in polyunsaturated membranes [46], sitting horizontally between bilayer leaflets. It has been proposed that this is due to cholesterol being unable to interact with the high relative disorder in polyunsaturated chains. As the lipids composing the mito-like membrane are all unsaturated with DOPS being di-monounsaturated and cardiolipin being polyunsaturated, it was possible that cholesterol could resist the interaction with the polyunsaturated chains and adopt a non-canonical orientation. A non-canonical orientation could have implications for protein insertion as it could prevent proteins from becoming transmembrane. We used both neutron reflectivity and fluorescent experiments to investigate the position and orientation of cholesterol in the mito-like membrane.

Our fluorescent data suggests some kind of intermediate orientation, or distribution of orientations for cholesterol. If cholesterol adopted a non-canonical orientation the dipole potential of the mito-like membrane (2.7b) should have been unchanged upon addition of cholesterol, just as observed for DAPC membranes, which it was

not. On the other hand, if cholesterol adopted a canonical orientation in the mito-like membrane, ψ_d would be expected to increase with a similar trend to that of the POPC membrane, since it is the largest component in the mito-like mix. This is not what is seen either in figure 2.7. This leaves the impression that cholesterol adopts neither a canonical nor a non-canonical orientation, and instead some sort of distribution between the two.

By marked contrast the neutron data clearly shows that the position of the cholesterol label is close to the hydrophilic headgroups of the phospholipids indicative of a canonical orientation. The location of the center of mass of cholesterol's deuterium label in the mito-like membrane moved outward from the center of the membrane as more cholesterol was added (see table 3.4). The change in its position of $\simeq 3\text{\AA}$, is much larger than the change in the carbonyl groups' position of $\simeq 0.2\text{\AA}$. The position of the label at 20% cholesterol is such that cholesterol's hydroxyl group can hydrogen bond with the carbonyl ester oxygens, whereas the position of the label at 10% cholesterol is such that the cholesterol hydroxyl group is much further away from the carbonyl ester oxygens, making hydrogen bonding to stabilize the interaction less likely. Assuming that van der Waal interactions between cholesterol's hydrocarbon side chain and the acyl tails of phospholipids are the greatest contributors to the interaction between cholesterol and phospholipids [120], it is possible that at lower cholesterol concentrations, 10%, van der Waals forces are enough to stabilize the interaction between cholesterol and the saturated lipids in the mito-mix. However, at higher cholesterol concentrations, 20%, cholesterol becomes forced to interact with the unsaturated acyl chains, which is less favorable for cholesterol, thus forcing cholesterol further away from the bilayer center towards the head groups. Additionally, as

discussed in section 3.3.5, the distribution of the cholesterol label at 10% cholesterol overlaps with the membrane and water profiles, indicating that hydrogen bonding is still possible with the ester oxygens in the carbonyl groups.

Kucerka et al. 2010 [64] showed that doping polyunsaturated DAPC with 50% of monounsaturated POPC, and only 5% of saturated DMPC would cause cholesterol to flip from a non-canonical to a canonical orientation. Therefore it seems that it requires a large concentration of polyunsaturated lipids for cholesterol to adopt a non-canonical orientation, which is not true of the mito-like membrane, and explains why we detected an increase in mito-like membrane dipole potential with the addition of cholesterol (figure 2.7b). Membranes in which cholesterol adopted a non-canonical orientation are also quite thin, with the carbonyl group at 15 Å [46] a result of increased membrane fluidity, and it was hypothesized that since cholesterol's ring structure sits at about 16 Å, it cannot fit vertically in the membrane and therefore must adopt a horizontal orientation [45]. The thickness of the mito-like membrane is still relatively large compared to the position of cholesterol's ring, and thus there is no impetus for cholesterol to orient horizontally.

From the neutron data, we would then expect the ψ_d trend for the mito-like membrane to follow that of the POPC, which is not the case. The discrepancy must then be explained by something other than cholesterol's orientation. Egg PC, which is predominantly POPC is removed from the mito-like mix when cholesterol is added. POPC is also removed when cholesterol is added to the one component membrane. Thus the dipole potential generated from the PC headgroups should be the same for both membranes, and should not be the reason for the discrepancy between the

POPC and mito-like ψ_d curves. We believe that the difference in POPC and mito-like ψ_d trends with cholesterol arises from a difference in the degree of orientation cholesterol is able to impart to the two membranes. Since cholesterol orders mono-unsaturated membranes more readily than di-monounsaturated membranes [93] and our S_{X-ray} data shows a less efficient ordering of the mito-like membrane as compared to single component membranes with the addition of cholesterol, it is likely that there would be a greater condensation effect for one-component membranes, as compared to multi-component unsaturated membranes. Thus we can expect a larger ψ_d for our one-component POPC membrane as compared to our five component mito-like membrane due to the increased lateral lipid density in the POPC membrane. This is possible, as the mito-like membrane is composed of five unsaturated lipids of different lengths with which cholesterol may have trouble ordering as compared to the single component POPC membrane. Moreover the condensing and thickening effects of cholesterol as discussed in section 4.0.7 appear to be weaker for the multicomponent mito-like membrane as compared to single lipid membranes composed of any of the individual mito-like lipid components.

Thus from both experiments we find that cholesterol adopts a canonical orientation in the mito-like membrane with its hydroxyl group in proximity for hydrogen bonding with the phospholipid ester oxygens.

4.2 Implications for Mitochondria with Elevated Cholesterol Content

In healthy cells, cholesterol is mainly found in the plasma membrane, while mitochondrial membranes contain only a minimal amount of cholesterol. This, however, has been shown to change in different disease states including cancer [24, 35, 95]. Importantly, increased concentrations of cholesterol in the mitochondria membrane has been shown to increase chemotherapy resistance [85], leading to the idea that targeting cholesterol production should be explored as a cancer treatment option [127]. A leading hypothesis is that mitochondrial cholesterol affects cancer treatment outcome by blocking outer membrane permeabilization during apoptosis. This is supported by several biophysical studies that have shown that, *in vitro*, cholesterol can block the pore formation activity of the pro-apoptotic protein Bax in mitochondria-like membranes [71, 20, 108]. Interestingly, all these studies concur that the step that is specifically blocked by the presence of cholesterol in the membrane is the insertion of the protein in the lipid bilayer. This effect is non-specific, as it can be replicated with the enantiomer of cholesterol [20]. Our study suggests several possible explanations for the inhibition of Bax membrane insertion, and therefore of its subsequent oligomerization and pore formation. A first possibility is that the main cause for Bax insertion inhibition is the condensing effect of cholesterol, accompanied by the decrease in electron density in the headgroup region (Fig. 3.7). The condensing effect would result in the elimination of defects in the membrane (probably mainly in the headgroup region, since the hydrophobic region is mostly incompressible), which may be required for Bax insertion into the membrane, and the decrease in electron density

could change how Bax “sees” the membrane as it approaches. A second possibility is that the main effect is the decrease in membrane flexibility and increase in order as demonstrated by S_{X-ray} that accompanies the addition of cholesterol (both membrane bending and compressibility have been shown to be affected by the ordering brought about by cholesterol [34]). A decrease in bending flexibility might prevent lipidic pore formation, a decrease in lateral compressibility might decrease lateral density fluctuations which may be indispensable for Bax pore formation, and an increase in order would make insertion of the protein through the hydrocarbon core of the membrane more difficult. A third possibility is that by increasing membrane thickness, cholesterol makes it difficult for Bax to adopt a transmembrane configuration. Follow up studies will be required in order to see which of these effects is most relevant to the interaction with the protein.

Chapter 5

Concluding Statements and Future Work

The goal of this work was to investigate the structure of a five component mito-like membrane with the addition of cholesterol, as an attempt to understand how cholesterol inhibits Bax insertion in mitochondria outer membranes. We used x-ray and neutron scattering to quantify biophysical quantities such as membrane thickness, area per phospholipid and order parameter, as well as using neutron scattering and fluorescence methods to find the location and orientation of cholesterol in a mito-like membrane.

The mitochondria-like membrane was found to have a lower order parameter and to be thicker while surprisingly having a similar area per chain as a POPC membrane. The mito-like membrane had a thinner lamellar distance than the POPC at lower hydration, while having a larger lamellar distance at higher hydration. The differences were quite small, except for the difference in order parameters. We found that the value of S_{X-ray} of the five component mito-like membrane was 28% less than that of a

single component POPC membrane suggesting that a mixed membrane is significantly disordered compared to a single component membrane. This was supported by the ordering effect of cholesterol on the mito-like membrane, which was found to be less pronounced than in one component membranes. In addition to its ordering effect, it was also confirmed that cholesterol had a condensing effect and increased the thickness of the mito-like membrane, in two hydration and temperature states.

Cholesterol was found to sit with a canonical orientation in the mito-like membrane, as it does in membranes composed of saturated, mono and di-monounsaturated lipids. The location of the hydroxyl group was found to move outwards from the center of the membrane as a function of the cholesterol content, suggesting that van der Waals interactions between cholesterol's hydrocarbon chain and the phospholipids' acyl chains are the main interactions at low cholesterol content, and hydrogen bonds between cholesterol's hydroxyl group and the phospholipid's carbonyl oxygens becomes important at higher cholesterol content.

The effects of cholesterol on the mitochondria-like membrane despite being less pronounced than those on one component membranes are still sufficient to inhibit Bax insertion. Three possibilities for the cause of the inhibition (which are not necessarily mutually exclusive) are that (1) cholesterol's condensing effect reduces the occurrence of membrane defects which are necessary for Bax insertion as well as reduces the electron density of the headgroup region potentially changing the charge density of the membrane surface, (2) that cholesterol increases the lateral order of the membrane, particularly in the membrane hydrophobic core, thus making Bax insertion and pore formation more difficult if not impossible and (3) cholesterol thickens the mitochondria membrane to such an extent as to inhibit Bax from adopting a trans-membrane

conformation. Identifying which of these effects are relevant to the protein would be useful for the understanding of cholesterol's role in cancer therapy resistance. Based on the work presented, the ordering of phospholipids due to cholesterol is a larger effect than the increase in thickness, as such I would suggest that the ordering brought about by cholesterol is the most likely reason for Bax insertion inhibition.

In order to establish with certainty whether the increase in thickness or the increase in orientational order brought about by cholesterol is inhibiting Bax, one could perform fluorescent release assay to judge Bax's effectiveness at permeabilizing the mitochondria outer membrane, on membranes with varying thickness or those with varying order. WAXS on these membranes would give a quantitative measure of the order parameter and thickness and thus help identify which effect of cholesterol is relevant to the protein Bax.

Appendix A

Neutron Form Factor

Determination

Slopes for the relationship between form factors and D₂O content for all six samples are plotted in figure A.1 with a fit from equation 2.24. The fitted slopes are then used to find the phases, ν_n of the form factors, F(n) for each Bragg order. Form factors as a function of D₂O content for all six samples are plotted figure A.2.

The form factors for all six samples are listed in table A.3.

Table A.3: Experimental form factors. Form factor magnitudes are found by taking the integrated intensity of each Bragg peak as described in section 2.3.2, while the phases are found using the contrast method as described in section 2.3.5 and shown in figure A.1 and figure A.2. Forward scattering form factor, F_0 is estimated based on the composition of samples using equation 2.25.

Sample	%D ₂ O	Diffraction peak order					
		0	1	2	3	4	5
POPC	100	-2.49E-4	-4.91	0.804	0.108	0	-0.0891
	70	-1.64E-4	-3.67	0.354	0.151	0	-0.0819
	40	-7.93E-5	-2.45	-0.145	0.171	0	-0.0644
	8	1.1E-5	-0.883	-0.550	0.219	0	-0.0574
Mito-like	100	-227E-4	-7.65	1.39	0.257	-0.125	-0.0449
	70	-1.5E-4	-6.00	0.54	0.270	-0.072	-0.045
	40	-7.24E-5	-3.91	-0.396	0.200	0	0
	8	1.01E-5	-1.41	-0.899	0.257	0	-0.040
Mito-like (10% H chol.)	100	-2.39E-4	-7.96	1.45	0.376	-0.137	0.054
	70	-1.58E-4	-6.23	0.71	0.322	-0.112	0.045
	40	-7.64E-5	-4.45	-0.369	0.251	0	0.023
	8	1.05E-5	-1.77	-1.01	0.311	0	-0.051
Mito-like (10% D chol.)	100	-2.43E-4	-8.20	1.13	0.439	-0.085	0
	70	-1.61E-4	-5.30	0.334	0.234	-0.033	0
	40	-7.77E-5	-5.32	-0.416	0.431	-0.046	-0.071
	8	1.07E-5	-1.82	-1.27	0.307	0.030	-0.043
Mito-like (20% H chol.)	100	-2.56E-4	-8.40	2.27	0.326	-0.268	-0.0413
	70	-1.68E-4	-6.20	0.903	0.292	-0.169	-0.035
	40	-8.17E-5	-5.14	-0.080	0.420	-0.208	-0.068
	8	1.11E-5	-1.86	-1.18	0.345	0	-0.056
Mito-like (20% D chol.)	100	-2.2E-4	-8.22	1.42	0.418	-0.136	-0.054
	70	-1.45E-4	-6.68	0.630	0.366	-0.096	-0.052
	40	-7.02E-5	-4.59	-0.50	0.302	0	-0.049
	8	9.49E-6	-0.374	-0.358	0.153	0	-0.060

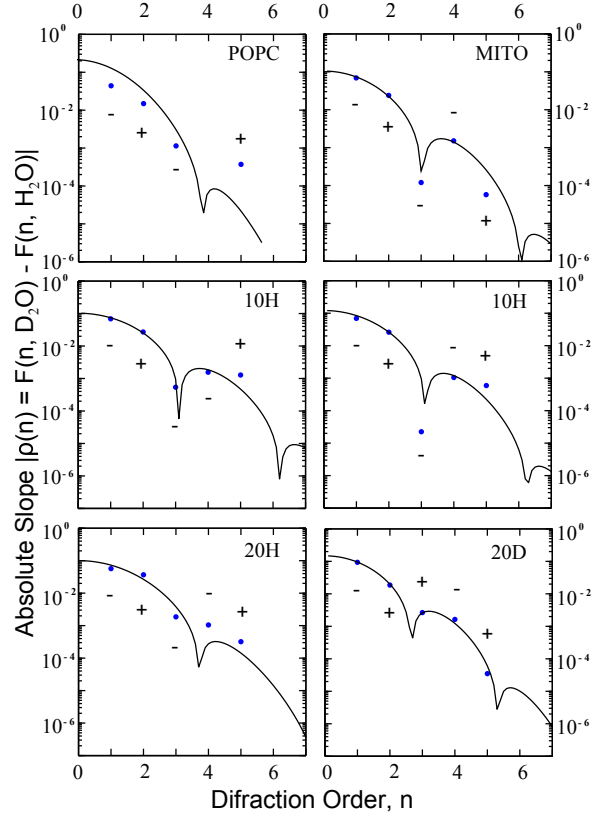


Figure A.1: **Form factor determination**. Semi-log plots of the absolute slope, $\rho(n)$, predicted from equation 2.24, and experimental form factor data for all six samples. The signs of the form factors are shown above or below the data, and alternate until a dip in the theoretical curve, after which the alternation starts again. The first sign must be negative as that produces the "U" shape in the NSLDs characteristic of a bilayer. $\rho(n) = [- + - - +]$ for all samples except mito-like (20% D cholesterol) which has $\rho(n) = [- + + - +]$.

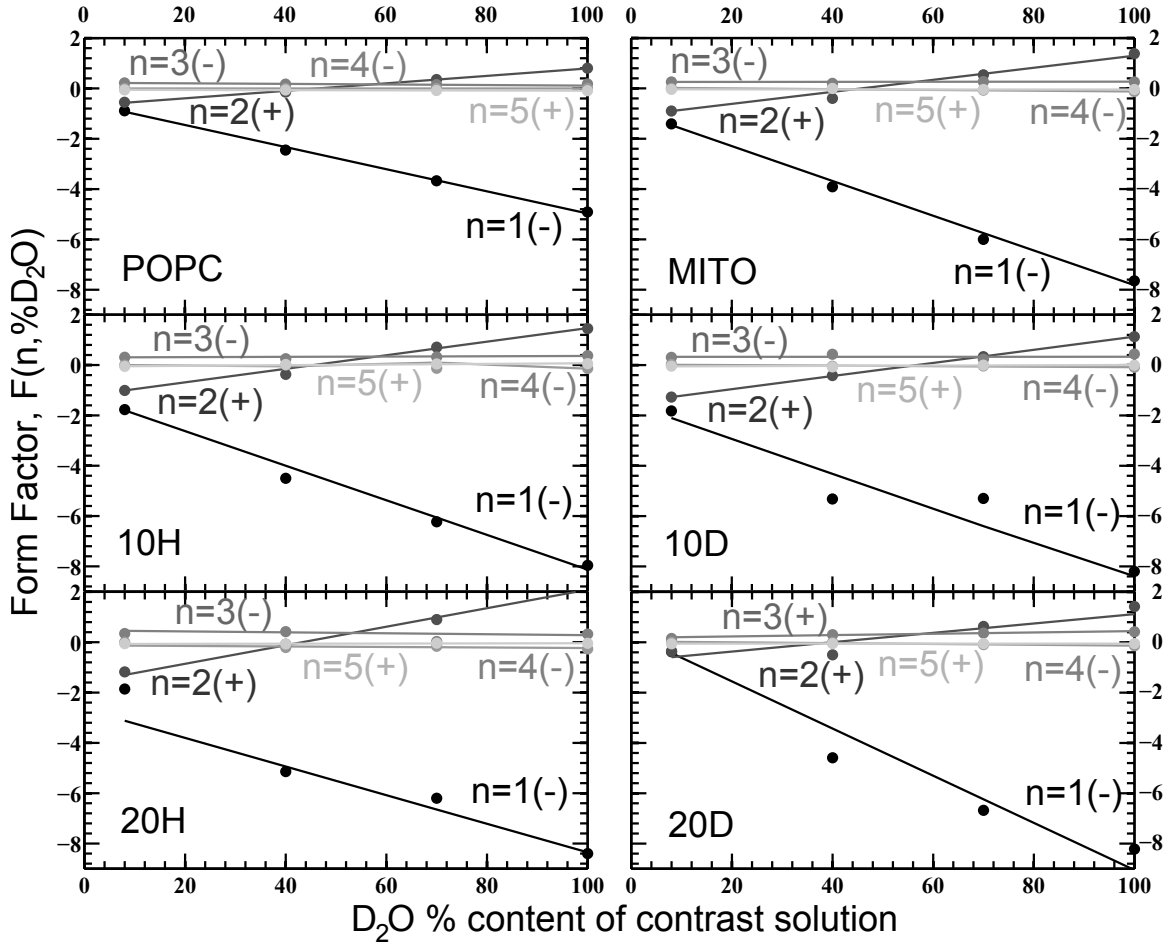


Figure A.2: Form factors for each diffraction order, n , as a linear function of D_2O content in the contrast solution. Data points represent form factors calculated from reflectivity data following equation 2.19, while lines are a fit, whose slopes are determined from the fit in figure A.1. The slope of each line then determines the sign of each form factor, and thus the phases. Form factors from each of the six samples for each of five diffraction orders are displayed.

Appendix B

Neutron Scattering Length Density Profiles

Scattering length density profiles were obtained by Fourier transforming the form factors from table A.3 using equation 2.20. SLDs are shown for all six samples in figure B.3.

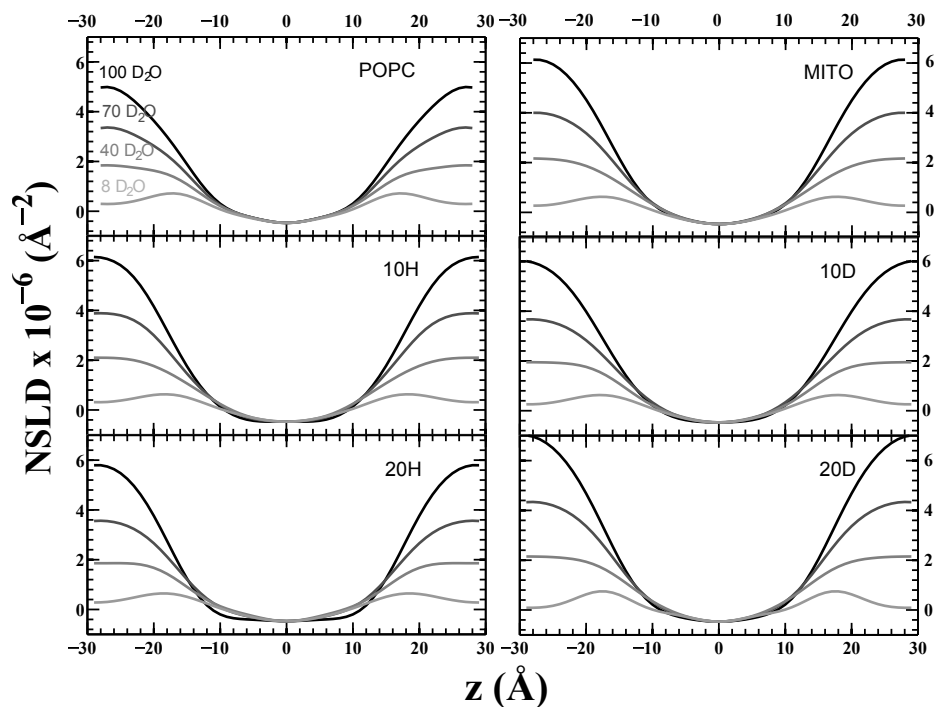


Figure B.3: **NSLD profiles for all samples at all D_2O contrasts.** Profiles are obtained for each of the four D_2O contrast solutions using equation 2.20 and scaled using equation 2.28.

Bibliography

- [1] Adachi, T. (2000). A new method for determining the phase in the X-ray diffraction structure analysis of phosphatidylcholine/alcohol. *Chemistry and physics of lipids*, **107**(1), 93–7.
- [2] Alsop, R. J., Barrett, M. A., Zheng, S., Dies, H., and Rheinstädter, M. C. (2014). Acetylsalicylic acid (asa) increases the solubility of cholesterol when incorporated in lipid membranes. *Soft Matter*, **10**, 4275–4286.
- [3] Andersen, O. S. and Koeppe, R. E. (2007). Bilayer thickness and membrane protein function: an energetic perspective. *Annual review of biophysics and biomolecular structure*, **36**, 107–30.
- [4] Armen, R. S., Uitto, O. D., and Feller, S. E. (1998). Phospholipid component volumes: determination and application to bilayer structure calculations. *Biophysical journal*, **75**(2), 734–744.
- [5] Armstrong, C. L., Barrett, M. A., Hiess, A., Salditt, T., Katsaras, J., Shi, A.-C., and Rheinstädter, M. C. (2012). Effect of cholesterol on the lateral nanoscale dynamics of fluid membranes. *Eur. Biophys. J.*, **41**(10), 901–913.
- [6] Armstrong, C. L., Marquardt, D., Dies, H., Kučerka, N., Yamani, Z., Harroun,

- T. A., Katsaras, J., Shi, A.-C., and Rheinstädter, M. C. (2013a). The observation of highly ordered domains in membranes with cholesterol. *PLOS ONE*, **8**, e66162.
- [7] Armstrong, C. L., Marquardt, D., Dies, H., Kučerka, N., Yamani, Z., Harroun, T. a., Katsaras, J., Shi, A.-C., and Rheinstädter, M. C. (2013b). The Observation of Highly Ordered Domains in Membranes with Cholesterol. *PloS one*, **8**(6), e66162.
- [8] Armstrong, C. L., Häußler, W., Seydel, T., Katsaras, J., and Rheinstädter, M. C. (2014). Nanosecond lipid dynamics in membranes containing cholesterol. *Soft matter*, **10**(15), 2600–2611.
- [9] Ashkenazi, A. (2008). Directing cancer cells to self-destruct with pro-apoptotic receptor agonists. *Nature reviews. Drug discovery*, **7**(12), 1001–12.
- [10] Avanti Polar Lipids Inc., A. (2014). Phase transition temperatures for glycerophospholipids. avantilipids.com/index.php?option=com_content&id=1700&Itemid=419. Accessed: 2014-08-03.
- [11] Baggetto, L. G., Clottes, E., Vial, C., Cells, A.-d. T., and Glottes, E. (1992). Low Mitochondrial Proton Leak Due to High Membrane Cholesterol Content and Cytosolic Creatine Kinase as Two Features of the Deviant Bioenergetics of Ehrlich and AS30-D Tumor Cells Low Mitochondrial Proton Leak Due to High Membrane Cholesterol Content and. *Cancer Research*, **52**, 4935–4941.
- [12] Barrett, M. A., Zheng, S., Roshankar, G., Alsop, R. J., Belanger, R. K., Huynh, C., Kučerka, N., and Rheinstädter, M. C. (2012). Interaction of aspirin (acetylsalicylic acid) with lipid membranes. *PLoS ONE*, **7**(4), e34357.

- [13] Basañez, G., Sharpe, J. C., Galanis, J., Brandt, T. B., Hardwick, J. M., and Zimmerberg, J. (2002). Bax-type apoptotic proteins porate pure lipid bilayers through a mechanism sensitive to intrinsic monolayer curvature. *The Journal of biological chemistry*, **277**(51), 49360–5.
- [14] Breen, G. A. and Draper, R. K. (2008). *Medical Cell Biology*. Elsevier.
- [15] Brockman, H. (1994). Dipole potential of lipid membranes. *Chemistry and physics of lipids*, **73**(1-2), 57–79.
- [16] Buerger, M. (1940). The correction of x-ray diffraction intensities for lorentz and polarization factors. *Proceedings of the National Academy of Sciences of the United States of America*, **26**, 637–642.
- [17] Cai, M., Zhao, W., Shang, X., Jiang, J., Ji, H., Tang, Z., and Wang, H. (2012). Direct evidence of lipid rafts by in situ atomic force microscopy. *Small (Weinheim an der Bergstrasse, Germany)*, **8**(8), 1243–50.
- [18] Cattaneo, E., Zuccato, C., and Tartari, M. (2005). Normal huntingtin function: an alternative approach to Huntington’s disease. *Nature reviews. Neuroscience*, **6**(12), 919–30.
- [19] Chernomordik, L. V. and Kozlov, M. M. (2008). Mechanics of membrane fusion. *Nature structural & molecular biology*, **15**(7), 675–83.
- [20] Christenson, E., Merlin, S., Saito, M., and Schlesinger, P. (2008). Cholesterol effects on BAX pore activation. *Journal of molecular biology*, **381**(5), 1168–83.
- [21] Clarke, R. J. and Kane, D. J. (1997a). Optical detection of membrane dipole

- potential: avoidance of fluidity and dye-induced effects. *Biochimica et biophysica acta*, **1323**(2), 223–39.
- [22] Clarke, R. J. and Kane, D. J. (1997b). Optical detection of membrane dipole potential: avoidance of fluidity and dye-induced effects. *Biochimica et biophysica acta*, **1323**(2), 223–39.
- [23] Colbeau, A., Nachbaur, J., and Vignais, P. (1971). Enzymic characterization and lipid composition of rat liver subcellular membranes. *Biochimica et biophysica acta*, **249**, 462–492.
- [24] Crain, R. C., Clark, R. W., Harvey, B. E., Mitochondria, M. H., and Grain, R. C. (1983). Role of Lipid Transfer Proteins in the Abnormal Lipid Content of Morris Hepatoma Mitochondria and Microsomes. *Cancer Research*, **42**, 3197–3202.
- [25] de Meyer, F. and Smit, B. (2009). Effect of cholesterol on the structure of a phospholipid bilayer. *Proc. Natl. Acad. Sci. U.S.A.*, **106**, 3654–3658.
- [26] de Meyer, F. J.-M., Benjamini, A., Rodgers, J. M., Misteli, Y., and Smit, B. (2010). Molecular simulation of the dmpc-cholesterol phase diagram. *The Journal of Physical Chemistry B*, **114**(32), 10451–10461.
- [27] Dies, H., Toppozini, L., and Rheinstädter, M. C. (2014). The Interaction between Amyloid- β Peptides and Anionic Lipid Membranes Containing Cholesterol and Melatonin. *PLoS one*, **9**(6), e99124.
- [28] Douliez, J.-p., Le, A., Dufourc, E. J., Recherche, C. D., and Pascal, P. (1996). Conformational Order of DMPC sn-1 versus sn-2 Chains and Membrane Thickness

- : An Approach to Molecular Protrusion by Solid State ^2H -NMR and Neutron Diffraction. *Journal of Physica Chemistry*, **3654**(96), 18450–18457.
- [29] Dragatsis, I., Levine, M. S., and Zeitlin, S. (2000). Inactivation of Hdh in the brain and testis results in progressive neurodegeneration and sterility in mice. *Nature genetics*, **26**(3), 300–6.
- [30] Drolle, E., Kučerka, N., Hoopes, M. I., Choi, Y., Katsaras, J., Karttunen, M., and Leonenko, Z. (2013). Effect of melatonin and cholesterol on the structure of DOPC and DPPC membranes. *Biochimica et biophysica acta*, **1828**(9), 2247–54.
- [31] Edholm, O. and Nagle, J. F. (2005). Areas of molecules in membranes consisting of mixtures. *Biophysical Journal*, **89**(3), 1827 – 1832.
- [32] Epand, R. F., Martinou, J.-C., Fornallaz-Mulhauser, M., Hughes, D. W., and Epand, R. M. (2002). The apoptotic protein tBid promotes leakage by altering membrane curvature. *The Journal of biological chemistry*, **277**(36), 32632–9.
- [33] Epand, R. F., Martinou, J.-C., Montessuit, S., and Epand, R. M. (2004). Fatty acids enhance membrane permeabilization by pro-apoptotic Bax. *The Biochemical journal*, **377**(Pt 2), 509–16.
- [34] Evans, E. and Rawicz, W. (1990). Entropy-driven tension and bending elasticity in condensed-fluid membranes. *Physical Review Letters*, **64**(17), 2094.
- [35] Feo, F., Canuto, R. a., Bertone, G., Garcea, R., and Pani, P. (1973). Cholesterol and phospholipid composition of mitochondria and microsomes isolated from morris hepatoma 5123 and rat liver. *FEBS letters*, **33**(2), 229–32.

- [36] Fidorra, M., Duelund, L., Leidy, C., Simonsen, A. C., and Bagatolli, L. (2006). Absence of fluid-ordered/fluid-disordered phase coexistence in ceramide/popc mixtures containing cholesterol. *Biophysical journal*, **90**(12), 4437–4451.
- [37] Fragneto, G. and Rheinstädter, M. (2007). Structural and dynamical studies from bio-mimetic systems: an overview. *Comptes Rendus Physique*, **8**, 865–883.
- [38] Gawrisch, K., Ruston, D., Zimmerberg, J., Parsegian, V. a., Rand, R. P., and Fuller, N. (1992). Membrane dipole potentials, hydration forces, and the ordering of water at membrane surfaces. *Biophysical journal*, **61**(5), 1213–23.
- [39] Gawrisch, K., Gaede, H. C., Mihailescu, M., and White, S. H. (2007a). Hydration of POPC bilayers studied by ^1H -PFG-MAS-NOESY and neutron diffraction. *European biophysics journal : EBJ*, **36**(4-5), 281–91.
- [40] Gawrisch, K., Gaede, H. C., Mihailescu, M., and White, S. H. (2007b). Hydration of POPC bilayers studied by ^1H -PFG-MAS-NOESY and neutron diffraction. *European biophysics journal : EBJ*, **36**(4-5), 281–91.
- [41] Gebert, N., Joshi, A. S., Kutik, S., Becker, T., McKenzie, M., Guan, X. L., Mooga, V. P., Stroud, D. a., Kulkarni, G., Wenk, M. R., Rehling, P., Meisinger, C., Ryan, M. T., Wiedemann, N., Greenberg, M. L., and Pfanner, N. (2009). Mitochondrial cardiolipin involved in outer-membrane protein biogenesis: implications for Barth syndrome. *Current biology : CB*, **19**(24), 2133–9.
- [42] Ghobrial, I. M., Witzig, T. E., and Adjei, A. A. (2005). Targeting Apoptosis Pathways in Cancer Therapy. *A Cancer Journal for Clinicians*, **55**, 178–194.

- [43] Gross, E., Bedlack, R. S., and Loew, L. M. (1994). Dual-wavelength ratiometric fluorescence measurement of the membrane dipole potential. *Biophysical journal*, **67**(1), 208–16.
- [44] Haldar, S., Kanaparthi, R. K., Samanta, A., and Chattopadhyay, A. (2012). Differential effect of cholesterol and its biosynthetic precursors on membrane dipole potential. *Biophysical journal*, **102**(7), 1561–9.
- [45] Harroun, T. a., Katsaras, J., and Wassall, S. R. (2006). Cholesterol hydroxyl group is found to reside in the center of a polyunsaturated lipid membrane. *Biochemistry*, **45**(4), 1227–33.
- [46] Harroun, T. a., Katsaras, J., and Wassall, S. R. (2008). Cholesterol is found to reside in the center of a polyunsaturated lipid membrane. *Biochemistry*, **47**(27), 7090–6.
- [47] Hartmann, A., Hunot, S., Michel, P. P., Muriel, M.-p., Vyas, S., Faucheu, B. A., Mouatt-prigent, A., Turmel, H., Srinivasan, A., Ruberg, M., Evan, G. I., Agid, Y., and Hirsch, E. C. (2000). Caspase-3 : A vulnerability factor and final effector in apoptotic death of dopaminergic neurons in Parkinson s disease. *Proceedings of the National Academy of Sciences of the United States of America*, **97**(6), 2875–2880.
- [48] Hartmann, A., Troadec, J.-d., Kikly, K., Faucheu, B. A., Mouatt-prigent, A., Ruberg, M., Agid, Y., and Hirsch, E. C. (2001a). Caspase-8 Is an Effector in Apoptotic Death of Dopaminergic Neurons in Parkinson s Disease , But Pathway Inhibition Results in Neuronal Necrosis. *The Journal of neuroscience : the official journal of the Society for Neuroscience*, **21**(7), 2247–2255.

- [49] Hartmann, A., Michel, P. P., Troadec, J.-d., Mouatt-prigent, A., Faucheuix, B. A., Ruberg, M., Agid, Y., and Hirsch, E. C. (2001b). Is Bax a mitochondrial mediator in apoptotic death of dopaminergic neurons in Parkinson ' s disease ? *Journal of Neurochemistry*, **76**, 1785–1793.
- [50] Henriksen, J., Rowat, A. C., Brief, E., Hsueh, Y., Thewalt, J., Zuckermann, M., and Ipsen, J. H. (2006). Universal behavior of membranes with sterols. *Biophysical journal*, **90**(5), 1639–1649.
- [51] Hung, W.-C., Lee, M.-T., Chen, F.-Y., and Huang, H. W. (2007). The condensing effect of cholesterol in lipid bilayers. *Biophysical journal*, **92**(11), 3960–7.
- [52] Hyslop, P. A., Morel, B., and Sauerheber, R. D. (1990). Organization and interaction of cholesterol and phosphatidylcholine in model bilayer membranes. *Biochemistry*, **29**(4), 1025–1038.
- [53] Ipsen, J. H., Karlstrom, G., Mouritsen, O., Wennerstrom, H., and Zuckermann, M. (1987). Phase equilibria in the phosphatidylcholine-cholesterol system. *Biochimica et Biophysica Acta*, **905**, 162–172.
- [54] Jacrot, B. (1976). The study of biological strutures by neutron scattering from solution. *Rep. Prog. Phys.*, (39), 911–953.
- [55] Janmey, P. a. and Kinnunen, P. K. J. (2006). Biophysical properties of lipids and dynamic membranes. *Trends in cell biology*, **16**(10), 538–46.
- [56] Jójárt, B. and Martinek, T. A. (2007). Performance of the general amber force field in modeling aqueous popc membrane bilayers. *Journal of computational chemistry*, **28**(12), 2051–2058.

- [57] Kang, M. H. and Reynolds, C. P. (2009). Bcl-2 inhibitors: targeting mitochondrial apoptotic pathways in cancer therapy. *Clinical cancer research : an official journal of the American Association for Cancer Research*, **15**(4), 1126–32.
- [58] Katsaras, J. (1998). Adsorbed to a rigid substrate, dimyristoylphosphatidyl-choline multibilayers attain full hydration in all mesophases. *Biophysical Journal*, **75**, 2157–2162.
- [59] Katsaras, J., Jeffrey, K. R., Yang, D. S., and Epand, R. M. (1993). Direct evidence for the partial dehydration of phosphatidylethanolamine bilayers on approaching the hexagonal phase. *Biochemistry*, **32**(40), 10700–7.
- [60] King, G. I. and Worthington, C. (1971). Analytic Continuation as a Method of Phase Determination. *Physics Letters*, **35**(4), 259–260.
- [61] Klauda, J. B., Kucerka, N., Brooks, B. R., Pastor, R. W., and Nagle, J. F. (2006). Simulation-based methods for interpreting x-ray data from lipid bilayers. *Biophysical journal*, **90**(8), 2796–807.
- [62] Kucerka, N., Liu, Y., Chu, N., Petrache, H. I., Tristram-Nagle, S., and Nagle, J. F. (2005). Structure of fully hydrated fluid phase DMPC and DLPC lipid bilayers using X-ray scattering from oriented multilamellar arrays and from unilamellar vesicles. *Biophysical journal*, **88**(4), 2626–37.
- [63] Kučerka, N., Pencer, J., Nieh, M.-P., and Katsaras, J. (2007). Influence of cholesterol on the bilayer properties of monounsaturated phosphatidylcholine unilamellar vesicles. *The European Physical Journal E*, **23**(3), 247–254.

- [64] Kucerka, N., Marquardt, D., Harroun, T. a., Nieh, M.-P., Wassall, S. R., de Jong, D. H., Schäfer, L. V., Marrink, S. J., and Katsaras, J. (2010). Cholesterol in bilayers with PUFA chains: doping with DMPC or POPC results in sterol reorientation and membrane-domain formation. *Biochemistry*, **49**(35), 7485–93.
- [65] Kučerka, N., Liu, Y., Chu, N., Petrache, H. I., Tristram-Nagle, S., and Nagle, J. F. (2005). Structure of fully hydrated fluid phase DMPC and DLPC lipid bilayers using x-ray scattering from oriented multilamellar arrays and from unilamellar vesicles. *Biophys. J.*, **88**, 2626–2637.
- [66] Kučerka, N., Nieh, M.-p., Pencer, J., Sachs, J. N., and Katsaras, J. (2009). What determines the thickness of a biological membrane. *General Physiology and Biophysics*, **28**, 117–125.
- [67] Kuwana, T., Mackey, M. R., Perkins, G., Ellisman, M. H., Latterich, M., Schneiter, R., Green, D. R., and Newmeyer, D. D. (2002). Bid, Bax, and lipids cooperate to form supramolecular openings in the outer mitochondrial membrane. *Cell*, **111**(3), 331–42.
- [68] Leber, B., Lin, J., and Andrews, D. W. (2007). Embedded together: the life and death consequences of interaction of the Bcl-2 family with membranes. *Apoptosis : an international journal on programmed cell death*, **12**(5), 897–911.
- [69] Leonard, A., Escrive, C., Laguerre, M., Pebay-peyroula, E., Neri, W., Pott, T., Katsaras, J., and Dufourc, E. J. (2001). Location of Cholesterol in DMPC Membranes . A Comparative Study by Neutron Diffraction and Molecular Mechanics Simulation . *Langmuir*, **17**(6), 2019–2030.

- [70] Lucken-Ardjomande, S., Montessuit, S., and Martinou, J.-C. (2008a). Bax activation and stress-induced apoptosis delayed by the accumulation of cholesterol in mitochondrial membranes. *Cell death and differentiation*, **15**(3), 484–93.
- [71] Lucken-Ardjomande, S., Montessuit, S., and Martinou, J.-C. (2008b). Bax activation and stress-induced apoptosis delayed by the accumulation of cholesterol in mitochondrial membranes. *Cell Death & Differentiation*, **15**(3), 484–493.
- [72] Lucken-Ardjomande, S., Montessuit, S., and Martinou, J.-C. (2008c). Contributions to Bax insertion and oligomerization of lipids of the mitochondrial outer membrane. *Cell death and differentiation*, **15**(5), 929–37.
- [73] Lund-Katz, S., Laboda, H. M., McLean, L. R., and Phillips, M. C. (1988). Influence of Molecular Packing and Phospholipid Type on Rates of Cholesterol Exchange. *Biochemistry*, **27**(1961), 3416–3423.
- [74] Majno, G. and Joris, I. (1995). Apoptosis, Oncosis, and Necrosis: An Overview of Cell Death. *American Journal of Pathology*, **146**(1), 3–15.
- [75] Mannock, D. a., McIntosh, T. J., Jiang, X., Covey, D. F., and McElhaney, R. N. (2003). Effects of natural and enantiomeric cholesterol on the thermotropic phase behavior and structure of egg sphingomyelin bilayer membranes. *Biophysical journal*, **84**(2 Pt 1), 1038–46.
- [76] Marquardt, D., Williams, J. A., Kucerka, N., Atkinsons, J., Wassall, S. R., Katsaras, J., and Harroun, T. A. (2013). Tocopherol activity correlates with its location in a membrane: a new perspective on the antioxidant vitamin E. *Journal of the American Chemical Society*, **135**(20), 7523–7533.

- [77] Marsan, M. P., Muller, I., Ramos, C., Rodriguez, F., Dufourc, E. J., Czaplicki, J., and Milon, a. (1999). Cholesterol orientation and dynamics in dimyristoylphosphatidylcholine bilayers: a solid state deuterium NMR analysis. *Biophysical journal*, **76**(1 Pt 1), 351–9.
- [78] Mayer, B. and Oberbauer, R. (2003). Mitochondrial regulation of apoptosis. *News in physiological sciences : an international journal of physiology produced jointly by the International Union of Physiological Sciences and the American Physiological Society*, **18**, 89–94.
- [79] McConnell, H. M. and Radhakrishnan, A. (2003). Condensed complexes of cholesterol and phospholipids. *Biochimica et Biophysica Acta*, **1610**, 159–173.
- [80] McIntosh, T. J. (1999). *Membrane Permeability - 100 Years since Ernest Overton*, volume 48 of *Current Topics in Membranes*. Elsevier.
- [81] Meier, P., Finch, A., and Evan, G. (2000). Apoptosis in development. *Nature*, **407**(6805), 796–801.
- [82] Mills, T. T., Tristram-Nagle, S., Heberle, F. A., Morales, N. F., Zhao, J., Wu, J., Toombes, G. E., Nagle, J. F., and Feigenson, G. W. (2008a). Liquid-liquid domains in bilayers detected by wide angle x-ray scattering. *Biophysical journal*, **95**(2), 682–690.
- [83] Mills, T. T., Toombes, G. E. S., Tristram-Nagle, S., Smilgies, D.-M., Feigenson, G. W., and Nagle, J. F. (2008b). Order parameters and areas in fluid-phase oriented lipid membranes using wide angle X-ray scattering. *Biophysical journal*, **95**(2), 669–81.

- [84] Mills, T. T., Toombes, G. E. S., Tristram-Nagle, S., Smilgies, D.-M., Feigenson, G. W., and Nagle, J. F. (2008c). Order parameters and areas in fluid-phase oriented lipid membranes using wide angle x-ray scattering. *Biophysical Journal*, **95**, 669–681.
- [85] Montero, J., Morales, A., Llacuna, L., Lluis, J. M., Terrones, O., Basañez, G., Antonsson, B., Prieto, J., García-Ruiz, C., Colell, A., and Fernández-Checa, J. C. (2008). Mitochondrial cholesterol contributes to chemotherapy resistance in hepatocellular carcinoma. *Cancer research*, **68**(13), 5246–56.
- [86] Mouritsen, O. G. and Zuckermann, M. J. (2004). What's so special about cholesterol? *Lipids*, **39**(11), 1101–13.
- [87] Nagle, J., Zhang, R., Tristram-Nagle, S., Sun, W., Petrache, H., and Suter, R. (1996). X-ray structure determination of fully hydrated $\lambda\alpha$ phase dipalmitoylphosphatidylcholine bilayers. *Biophys. J.*, **70**, 1419–1431.
- [88] Nagle, J. F. and Tristram-Nagle, S. (2000). Structure of lipid bilayers. *Biochimica et Biophysica Acta (BBA) - Reviews on Biomembranes*, **1469**(3), 159–195.
- [89] Ohvo-Rekilä, H., Ramstedt, B., Leppimäki, P., and Slotte, J. P. (2002). Cholesterol interactions with phospholipids in membranes. *Progress in lipid research*, **41**(1), 66–97.
- [90] Omega Engineering Inc., O. (2014). Equilibrium relative humidity: Saturated salt solutions. www.omega.com/temperaturesz/pdf/z103.pdf. Access: 2014-08-03.

- [91] Pabst, G., Kučerka, N., Nieh, M.-P., Rheinstädter, M., and Katsaras, J. (2010). Applications of neutron and x-ray scattering to the study of biologically relevant model membranes. *Chemistry and Physics of Lipids*, **163**(6), 460 – 479.
- [92] Pan, D., Wang, W., Liu, W., Yang, L., and Huang, H. W. (2006). Chain packing in the inverted hexagonal phase of phospholipids: a study by x-ray anomalous diffraction on bromine-labeled chains. *Journal of the American Chemical Society*, **128**(11), 3800–3807.
- [93] Pan, J., Mills, T., Tristram-Nagle, S., and Nagle, J. (2008). Cholesterol Perturbs Lipid Bilayers Nonuniversally. *Physical Review Letters*, **100**(19), 198103.
- [94] Pandit, S. A., Chiu, S.-W., Jakobsson, E., Grama, A., and Scott, H. (2007). Cholesterol surrogates: a comparison of cholesterol and 16: 0 ceramide in popc bilayers. *Biophysical journal*, **92**(3), 920–927.
- [95] Parlo, R. A. and Coleman, S. (1984). Enhanced Rate of Citrate Export from Cholesterol-rich Hepatoma Mitochondria. *The Journal of Biological Chemistry*, **259**(16), 9997–10000.
- [96] Perier, C., Tieu, K., Guégan, C., Caspersen, C., Jackson-Lewis, V., Carelli, V., Martinuzzi, A., Hirano, M., Przedborski, S., and Vila, M. (2005). Complex I deficiency primes Bax-dependent neuronal apoptosis through mitochondrial oxidative damage. *Proceedings of the National Academy of Sciences of the United States of America*, **102**(52), 19126–31.
- [97] Perier, C., Bové, J., Wu, D.-C., Dehay, B., Choi, D.-K., Jackson-Lewis, V., Rathke-Hartlieb, S., Bouillet, P., Strasser, A., Schulz, J. B., Przedborski, S.,

- and Vila, M. (2007). Two molecular pathways initiate mitochondria-dependent dopaminergic neurodegeneration in experimental Parkinson's disease. *Proceedings of the National Academy of Sciences of the United States of America*, **104**(19), 8161–6.
- [98] Peterson, U., Mannock, D. a., Lewis, R. N. a. H., Pohl, P., McElhaney, R. N., and Pohl, E. E. (2002). Origin of membrane dipole potential: contribution of the phospholipid fatty acid chains. *Chemistry and physics of lipids*, **117**(1-2), 19–27.
- [99] Petrache, H., Dodd, S., and Brown, M. (2000). Area per lipid and acyl length distributions in fluid phosphatidylcholines determined by (2)H NMR spectroscopy. *Biophys. J.*, **79**, 3172–3192.
- [100] Qian, S., Wang, W., Yang, L., and Huang, H. W. (2008). Structure of transmembrane pore induced by Bax-derived peptide: evidence for lipidic pores. *Proceedings of the National Academy of Sciences of the United States of America*, **105**(45), 17379–83.
- [101] Ridgway, N., McLeod, R., Vance, J., and Vance, D. E. (2008). *Biochemistry of lipids, lipoproteins and membranes*. Elsevier.
- [102] Rigamonti, D., Bauer, J. H., De-Fraja, C., Conti, L., Sipione, S., Sciorati, C., Clementi, E., Hackam, a., Hayden, M. R., Li, Y., Cooper, J. K., Ross, C. a., Govoni, S., Vincenz, C., and Cattaneo, E. (2000). Wild-type huntingtin protects from apoptosis upstream of caspase-3. *The Journal of neuroscience : the official journal of the Society for Neuroscience*, **20**(10), 3705–13.
- [103] Rigamonti, D., Sipione, S., Goffredo, D., Zuccato, C., Fossale, E., and Cattaneo,

- E. (2001). Huntingtin's neuroprotective activity occurs via inhibition of procaspase-9 processing. *The Journal of biological chemistry*, **276**(18), 14545–8.
- [104] Roe, R.-J. (2000). *Methods of X-ray and Neutron Scattering*.
- [105] Satsoura, D., Kučerka, N., Shivakumar, S., Pencer, J., Griffiths, C., Leber, B., Andrews, D. W., Katsaras, J., and Fradin, C. (2012). Interaction of the full-length Bax protein with biomimetic mitochondrial liposomes: a small-angle neutron scattering and fluorescence study. *Biochimica et biophysica acta*, **1818**(3), 384–401.
- [106] Shamas-Din, A., Brahmbhatt, H., Leber, B., and Andrews, D. W. (2011). BH3-only proteins: Orchestrators of apoptosis. *Biochimica et biophysica acta*, **1813**(4), 508–20.
- [107] Shamas-Din, A., Binder, S., Chi, X., Leber, B., Andrews, D. W., and Fradin, C. (2014a). Distinct lipid effects on tBid and Bim activation of membrane permeabilization by pro-apoptotic Bax. *submitted*, pages 1–25.
- [108] Shamas-Din, A., Bindner, S., Chi, X., Leber, B., Andrews, D. W., and Fradin, C. (2014b). Effect of lipid composition on membrane permeabilization by bax when activated by tbid or bim. *Submitted*.
- [109] Shiratori, Y., Okwu, A. K., and Tabas, I. (1994). Free Cholesterol Loading of Macrophages Stimulates Phosphatidylcholine Biosynthesis and Up-regulation of CTP:Phosphocholine Cytidylyltransferase. *The Journal of biological chemistry*, **269**(15), 11337–11348.
- [110] Singer, S. J. and Nicolson, G. L. (1972). The fluid mosaic model of the structure of cell membranes. *Science (New York, N.Y.)*, **175**(4023), 720–31.

- [111] Smaby, J. M., Brockman, H. L., and Brown, R. E. (1994). Cholesterol's Interfacial Interactions with Sphingomyelins and Phosphatidylcholines : Hydrocarbon Chain Structure Determines the Magnitude of Condensation +. *Biochemistry*, **33**, 9135–9142.
- [112] Smolyrev, a. M. and Berkowitz, M. L. (1999). Structure of dipalmitoylphosphatidylcholine/cholesterol bilayer at low and high cholesterol concentrations: molecular dynamics simulation. *Biophysical journal*, **77**(4), 2075–89.
- [113] Soubias, O., Jolibois, F., Réat, V., and Milon, A. (2004). Understanding sterol-membrane interactions, part ii: Complete ¹h and ¹³C assignments by solid state nmr spectroscopy and determinaton of the hydrogen-bonding partners of cholesterol in a lipid bilayer. *Chemistry A European Journal*, **10**, 6005–6014.
- [114] Stockton, G. W. and Smith, I. C. (1976). A Deuterium Nuclear Magnetic Resonance Study of the Condensing Effect of Cholesterol on Egg Phosphatidylcholine Bilayer Membranes. I. Perdeuterated Fatty Acid Probes. *Chemistry and Physics of Lipids*, **17**, 251–263.
- [115] Tatton, N. a. (2000). Increased caspase 3 and Bax immunoreactivity accompany nuclear GAPDH translocation and neuronal apoptosis in Parkinson's disease. *Experimental neurology*, **166**(1), 29–43.
- [116] Toppozini, L., Armstrong, C. L., Barrett, M. A., Zheng, S., Luo, L., Nanda, H., Garcia Sakai, V., and Rheinstädter, M. (2012). Partitioning of ethanol into lipid membranes and its effect on fluidity and permeability as seen by x-ray and neutron scattering. *Soft Matter*, **8**, 11839–11849.

- [117] Tristram-Nagle, S., Liu, Y., Legleiter, J., and Nagle, J. F. (2002). Structure of gel phase DMPC determined by X-ray diffraction. *Biophys. J.*, **83**(6), 3324–3335.
- [118] Tristram-Nagle, S. A. (2007). Preparation of oriented, fully hydrated lipid samples for structure determination using x-ray scattering. *Methods in Membrane Lipids*, **400**, 63–75.
- [119] van Meer, G., Voelker, D. R., and Feigenson, G. W. (2008). Membrane lipids: where they are and how they behave. *Nature reviews. Molecular cell biology*, **9**(2), 112–24.
- [120] Vanderkooi, G. (1994). Computation of mixed phosphatidylcholine-cholesterol bilayer structures by energy minimization. *Biophysical journal*, **66**(5), 1457–68.
- [121] Vila, M., Jackson-lewis, V., Vukosavic, S., Djaldetti, R., Liberatore, G., Offen, D., Korsmeyer, S. J., and Przedborski, S. (2001). Bax ablation prevents dopaminergic neurodegeneration in the 1-methyl- mouse model of Parkinson s disease. *Proceedings of the National Academy of Sciences of the United States of America*, **98**(5), 2837–2842.
- [122] Viswanath, V., Wu, Y., Boonplueang, R., Chen, S., Stevenson, F. F., Yantiri, F., Yang, L., Beal, M. F., and Andersen, J. K. (2001). Caspase-9 Activation Results in Downstream Caspase-8 Activation and Bid Cleavage in 1-Methyl-4-Phenyl-1, 2 , 3 , 6-Tetrahydropyridine- Induced Parkinson s Disease. *The Journal of neuroscience : the official journal of the Society for Neuroscience*, **21**(24), 9519–9528.

- [123] Wang, Z.-J. and Deserno, M. (2010a). Systematic implicit solvent coarse-graining of bilayer membranes: lipid and phase transferability of the force field. *New journal of physics*, **12**(9), 095004.
- [124] Wang, Z.-J. and Deserno, M. (2010b). A systematically coarse-grained solvent-free model for quantitative phospholipid bilayer simulations. *The Journal of Physical Chemistry B*, **114**(34), 11207–11220.
- [125] Wiener, M. C. and White, S. H. (1992). Structure of a fluid dioleoylphosphatidylcholine bilayer determined by joint refinement of x-ray and neutron diffraction data. II. Distribution and packing of terminal methyl groups. *Biophysical journal*, **61**(2), 428–33.
- [126] Wiener, M. C., King, G. I., and White, S. H. (1991). Structure of a fluid dioleoylphosphatidylcholine bilayer determined by joint refinement of x-ray and neutron diffraction data. I. Scaling of neutron data and the distributions of double bonds and water. *Biophysical journal*, **60**(3), 568–76.
- [127] Wong, R. S. Y. (2011). Apoptosis in cancer: from pathogenesis to treatment. *Journal of experimental & clinical cancer research : CR*, **30**(1), 87.
- [128] Wong, W., Dimitroulakos, J., Minden, M., and Penn, L. (2002). REVIEW HMG-CoA reductase inhibitors and the malignant cell: the statin family of drugs as triggers of tumor-specific apoptosis. *Leukemia*, **16**(September 2001), 508–519.
- [129] Yethon, J. a., Epand, R. F., Leber, B., Epand, R. M., and Andrews, D. W. (2003). Interaction with a membrane surface triggers a reversible conformational

- change in Bax normally associated with induction of apoptosis. *The Journal of biological chemistry*, **278**(49), 48935–41.
- [130] Youle, R. J. and Strasser, A. (2008). The bcl-2 protein family: opposing activities that mediate cell death. *Nature Reviews Molecular Cell Biology*, **9**, 47–59.
- [131] Zinser, E. and Daum, G. (1995). Isolation and biochemical characterization of organelles from the yeast, *Saccharomyces cerevisiae*. *Yeast (Chichester, England)*, **11**(6), 493–536.